POLITECNICO DI MILANO

Facoltà di Ingegneria

Corso di Laurea in
Ingegneria Meccanica

POLITECNICO
MILANO 1863

Cathodic Arc Deposition PVD Coating: Process and Production Parameters Analysis Affecting Coating Layer Thickness.

Relatore: Ch.mo Prof. Quirico SEMERARO

Correlatore: Ing. Ranieri GIULIANI

Tesi di Laurea di:

Fabio SARGENTINI Matr. 836400

Anno Accademico 2017 – 2018

Ringraziamenti

Un ringraziamento speciale va al Ch.mo Prof Quirico Semeraro, per avermi guidato in questo lavoro di tesi con la massima pazienza e disponibilità.
Ringrazio tutti i membri di Oerlikon Balzers Coating Italy S.p.A. per il supporto ricevuto dall'azienda, in particolare il mio correlatore Ing Ranieri Giuliani, insieme alla Dott.ssa Claudia Bottosso e alla Dott.ssa Sara Cappelletti. Ringrazio anche l'Ing. Luca Barra, per la procura dei campioni in carburo cementato.
Ringrazio Andrea, per lo straordinario lavoro di preparazione superficiale dei campioni.
Un altro ringraziamento speciale va al Sig. Alberto Rivolta di Böhler, per la fornitura dei campioni in acciaio K110 ed S600.
Ringrazio cordialmente Utensil Tempra S.r.l. per il trattamento termico dei campioni
Infine, ringrazio la mia famiglia, Allegra e tutti i miei amici per avermi sempre sostenuto in questi anni di studio.

General Index

Figures List

Table List

Introduction

In Physical Vapor Deposition (PVD), a coating material is transferred from a source (frequently called a target) through the vapor phase to form a coating on a substrate. The PVD technology includes techniques such as evaporation, ion plating, sputtering, and laser ablation. It is used to deposit thin films of approximately 10 nm or less as well as thick films of 10 μm or more and even freestanding components. With one or more of these processes, virtually any solid material, with the exception of certain polymers, may be deposited onto any other solid surface.

Nowadays, PVD Coating technologies are gaining more and more importance in manufacturing industry, due to the high variety of applications: a layer thinner than a hair is able to significantly improve wear resistance of tools, reduce friction in precision components and protect from corrosion turbine blades.
The scope of the master thesis is to analyse, control and suggest improvements of a real PVD coating process, focusing on one of the most important output parameter: coating layer thickness.
Coating thickness is a parameter which must be kept under control in a coating process, both for geometrical reasons (e.g. tolerances), and because it has a high influence on performances of the coated tool, component etc.

The process analysed is the deposition of BALINIT® ALCRONA PRO, an AlCrN-based arc deposition coating, engineered and produced by Oerlikon Balzers, one of the global leader of PVD coating services and equipment.

The master thesis starts from a general overview about the PVD coating market and the main deposition techniques, which is followed by an analytical description of operations steps in a coating service plant of Oerlikon Balzers.
The next chapters introduce the core part of the thesis, with the presentation of “the thickness problem”, from the state of the art till the qualitative analysis performed to identify the key factors that affect coating thickness.
This section anticipates the measurement system analysis (MSA), which is essential for the validation of the following factor screening and main experiments.
The experimental part ends with an industrial optimization session, dealing with the problem from a double-perspective point of view.
Last chapters are then dedicated to results and conclusions of the research: from a development of a model, to recommendations addressed to the coating companies, and finally hints for a further development in the research.

Chapter 1

PVD Market, Applications and Competitors

1.1 Global PVD market

The global physical vapor deposition (PVD) market was valued 22.4 billion USD in 2016, and it is expected to grow up at a compound annual growth rate (CAGR) of 5.5%, till the global revenues will reach 29.2 billion USD value in 2021. [BCC Research LLC]
These aggregate revenue data consider coating services, materials and equipment supply. PVD equipment is the largest part of the market, as a matter of fact, its relevance was evaluated as the 60.2% of the overall market in 2013. [Grand View Research Inc.]
Asia Pacific and North America dominates the global PVD market, collectively constituting more than 60% share in 2015. Large number of PVD service providers are emerging in Asia Pacific due to the significant increase in demand for PVD and attractive profit margins. Various PVD equipment and service providers operate in developed regions such as North America and Europe, where this technology was born.

1.2 Applications and trends

Possible applications of PVD technology are in continuous expansion.
Nowadays, they include microelectronics, data storage, solar products, manufacturing tools, precision components, medical equipment, and many others.
Microelectronics was estimated as the largest application of the technology across the globe, accounting for 37.8% of the market share in the year 2015.
Cutting tools coating is one of the first application developed, indeed the first industrial developments in this field started from the ’70 of the last century. The focus of the coating development was on wear protection against abrasion and adhesion.
In 1969, the first CVD (Chemical Vapour Deposition) tool coating was introduced on the market: a TiC based coating suitable for carbide tools. Its fast success lead to a dynamic development progress of CVD processes as well as the coating materials TiCN, TiN and Al2O3.
In 1980, TiN (Titanium Nitride) became the first PVD coating to be applied in the industry. 9 years later, TiAIN followed. The advantage of PVD in lower deposition temperatures with respect CVD, made the coating of tool steels possible. Even though investigations on innumerable coating materials were run throughout the 1970s and 1980s, TiC, TiCN, TiN, TiAIN, Al2O3 still remain the tool coatings applied most frequently today. Other materials applied are CrN, AICrN, TiB2, ZrN and carbon coatings such as diamond or DLC. [Bob16]
In tools segment, applications are not limited to cutting tools.
Nowdays, even big dimension metal forming tools, moulds for plastic processing and die casting are treated. Moulds are treated to prevent wear and improve tool life, and also to prevent adhesion of the moulded material on the tool surface.
Other applications are designed for friction reduction.
Increasing environmental awareness and energy costs are major driving forces behind the development of energy efficient machines. Simultaneously, increased energy efficiency often leads to higher power densities and therefore higher wear rates and reduced life times. Enhanced wear protection and reduced friction are the goals of

research and development in many fields of industry. Regarding tribological systems, wear and friction are strongly affected by the lubricant and especially by the additive composition. Over the years a broad variety of particular additive families has been developed to serve the demands of modern mechanical systems. According to their primary purpose, lubricant additives can be divided into anti wear (AW), extreme pressure (EP) and friction modifier (FM) additives. Although, the choice of lubricant and additive can significantly contribute to wear and friction reduction, the loads often exceed the load carrying capacities of the base materials. Therefore, coatings for the application on tribological highly stressed components were developed. In the automotive sector diamond-like carbon (DLC) coatings, deposited by PVD or Plasma Enhanced Chemical Vapor Deposition (PECVD), are widely used on components of the power train such as bearing shells, piston pins and injectors. Interactions between tribological coatings and lubricants become more and more subject of research activities. Besides DLC coatings, nitride hard coatings applied by PVD show a high potential for wear reduction in industrial applications and in addiction to that they exhibit a high thermal stability. [Bob17]

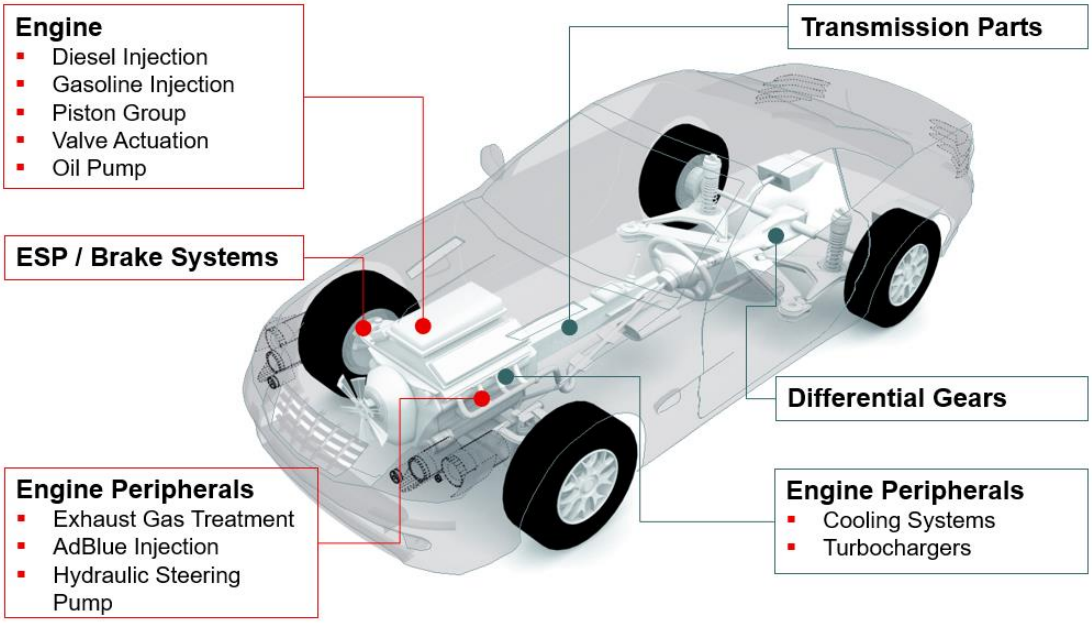

Figure 1.1: PVD applications in automotive industry. [courtesy of Oerlikon Balzers]

PVD coatings are environmentally friendly compared to other coating technologies such as electroplating.: Policies for restricting hex chrome electroplating due to production of toxic wastes in economies such as Europe and the U.S. are anticipated to boost the growth of the market in this direction.
Due to the rising demand for high-efficient solar panels, even solar application segment of the PVD market is anticipated to expand significantly, with a forecasted CAGR of 10.2% from 2016-2024. [Grand View Research] Utilization of the technology in solar products is estimated as one of the fastest growing segment. This sector is expected to grow prominently in the Asia Pacific and Europe owing to increase in the R&D investments by both wafer and photovoltaic cell manufacturers to maintain low cost due to declining selling prices.
Another key application which is going to drive the market in the next years is medical equipment. This market is expected to grow at a CAGR of 10.9% from 2016 to 2024.

Since it was introduced to the medical device industry in the late 1980s, physical vapor deposition (PVD) has become widely used to deposit wear-resistant thin-film coatings on a variety of medical devices, including orthopaedic implants, pacemakers, surgical instruments, orthodontic appliances and dental instruments. The value of PVD technology rests in its ability to modify the surface properties of a device without changing the underlying material properties and biomechanical functionality.
Increasing expenditure by various governments to provide basic healthcare facilities to its population is anticipated to augment the demand for devices & equipment, subsequently driving the physical vapor deposition industry.
PVD technology is employed also to deposit Thermal Barrier Coatings (TBC) on turbine blades. TBC have been widely studied over the past 20 years because they increase the durability and efficiency of gas turbine engines by allowing an increase in turbine inlet temperature and by reducing the amount of cooling air required by the hot-section components. It has been reported that applications of such coatings throughout the combustion chamber and early stages of the turbine would save an operator around 1-2% of fuel cost, translating into savings of over $10 million per annum for some companies. [Xu98]

1.3 PVD companies, a focus on Oerlikon Balzers

1.3.1 History

The company was born as “Gerätebauanstalt Balzers” in Balzers (Liechtenstein) in 1946, founded by Professor Max Auwärter with the support of Prince Franz Josef II and Swiss industrialist Emil Georg Bührle.
The objective was to make the then largely unknown and little-researched vacuum thin-film technology useable on an industrial scale. Since no systems and equipment for the production of thin-film coatings were available at the time, the company developed and produced them in-house. The first popular applications were sun protection and anti-reflection coatings for ophthalmic lenses, anti-reflection coatings for camera lenses, optical filters and reflectors and thin films for electronic applications.

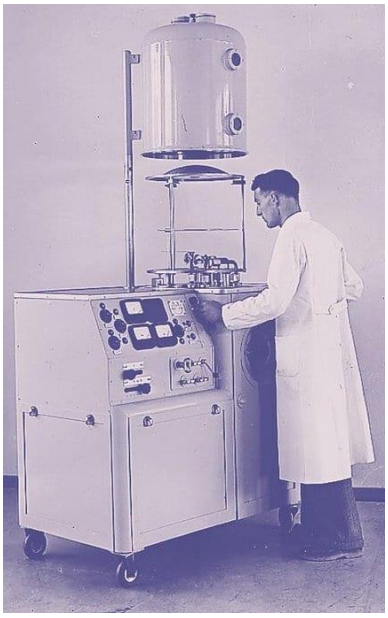

Figure 1.2: Balzers vacuum evaporator BA 500, 1954 [Courtesy of Oerlikon Balzers]

In 1974, Balzers decided to develop scratch-proof gold-coloured PVD coatings for the watch industry, two years after the company founder Prof. Max Auwärter retired and Oerlikon-Bührle Holding AG (Now OC Oerlikon Corporation AG) became the company′s sole owner.
Then, the company concentrates its business on PVD coating for tools market.
In 1977 the first trials of TiN-coated forming tools are successful: experiments evidence a tool service life increased by a factor of 4. The next year, the official go-ahead was given for the development and marketing of PVD hard coatings for tools with BALINIT® A (TiN based coating). In 1980 twist drills coated by Balzers were shown for the first time, at an exhibition in Germany.

Figure 1.3: Tools and components coated with TiN-based BALINIT® A coating. [Courtesy of Oerlikon Balzers]

In 1983 the company started its worldwide expansion: First coating centre outside Liechtenstein was opened in Italy, followed the next year by openings in Germany, Spain and the USA.
The first application of coatings to precision components was launched in 1985.
In the 90s, the company continued its expansion worldwide, opening new coating centres, developing new coatings materials and widening the application of the technology.
In 2000, BALINIT-coated components were used on the new Volkswagen Lupo 3L TDI, the world's first mass-production 3-litre car (manufacturer declared a consumption of 3 litres of fuel each 100 km), and in the same year BALINIT® DLC diamond-like carbon coating was introduced.
In the last decade, alongside the introduction of new coating machines and materials, has boosted the development of new coating technologies. In 2011 was patented and industrialized S3p® technology, based on High-power impulse magnetron sputtering (HiPIMS), which combines the advantage of arc evaporation and sputtering.

1.3.2 Company profile

Oerlikon Balzers is part of the Surface Solutions Segment of OC Oerlikon Corporation AG, a swiss-based technology group structured in three segments: manufacturing of protective coatings for precision tools and components (Surface Solutions Segment), equipment for textile production (Manmade Fibers Segment) and propulsion technology (Drive Systems Segment).

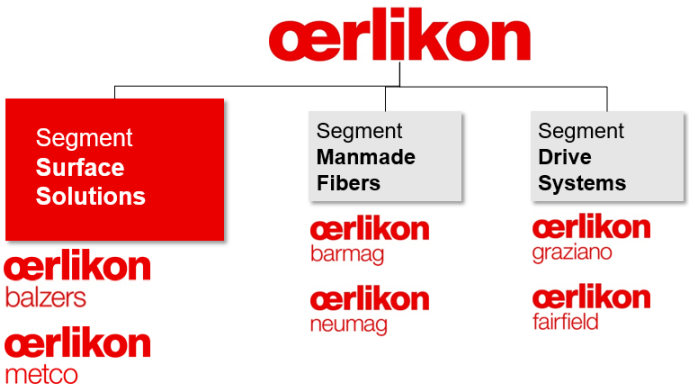

Figure 1.4: OC Oerlikon Segments

In Surface Solution Segment more than 6100 people are employed, with a global presence in 37 countries and a 1.2bn CHF of sales revenue.
Balzers Industrial Solutions is the business unit of Surface Solution Segment which develops and produces coating equipment and services for tools and precision components. More than 100 coating service centres are active worldwide, with a global and diffused presence in continuous expansion.
It has been estimated that about 33% of all tools worldwide are coated by Oerlikon Balzers.
Customers range over many industrial sectors, from tools manufacturing, to automotive industry, metalworking, aerospace, oil & gas, plastic processing, mechanical engineering, plant construction and many others.
In Italy, Oerlikon Balzers has two coating plants, one in Brugherio (MI), where there is also the regional HQ, and the other one in Limena (PD). There is an additional in-house coating department located inside Samputensili plant in Bentivoglio (BO).
Oerlikon Balzers Coating Italy S.p.A. is a joint-stock company with a sales volume of 13.921 million € in 2016.

1.4 Italian and global competitors

Several global key players operate in the PVD market in addiction to Oerlikon Balzers.
The Japanese group IHI Corporation holds IHI Ionbond AG, a worldwide provider of coating services with over 1000 employees working in 39 service centres in 17 countries in Europe, North America and Asia, and IHI Hauzer Techno Coating B.V., a coating machines manufacturer.
Swiss company Platit AG, part of BCI Group, is another relevant competitor, mainly focussed on coating equipment production.

In the Italian coating service market, the Italian joint-stock company Lafer S.p.A. is one of the greatest players, with a sales revenue of 20.277 k€ in 2016.

Chapter 2

Deposition technologies

The main difference among PVD deposition technologies is the method employed to heat and vaporize the target material.
The basic PVD processes fall into two general categories: sputtering and evaporation. Thickness of the deposits can vary from angstroms to millimetres. A very high deposition rate (i.e. 25 μm/min) has been achieved with the advent of Electron Beam (EB) heated sources. A very large number of inorganic materials (metals, alloys, compounds, and mixtures) as well as some organic materials can be deposited using PVD technologies. Ion plating is a hybrid PVD process because it is defined as an atomistic film deposition process in which the substrate surface and the depositing film is subjected to a flux of high-energy particles that is sufficient to cause changes in the interfacial region between the film and the substrate in addition to changes in the properties of the deposited film as compared to a nonbombarded film. These changes may be in the adhesion of the film to the substrate or in morphology, density, or stress. The source of the depositing species can be evaporation, sputtering, gases, or vapors.
Substrate temperatures can range from approximately 50 °C (120 °F) for some plastics to approximately 600 °C (1100 °F) for the deposition of ceramics and metal carbides. Vacuum-coating processes usually operates at pressures ranging from 13.33 to 1.33×10^{-6} Pa (10^{-1} to 10^{-8} torr). Both amorphous and crystalline microstructures can be produced in a controlled manner at temperatures low enough to prevent distortion or microstructural changes during the coating process.

2.1 Evaporation PVD

The major forms of evaporation PVD include thermal, electron beam, laser beam, activated reactive evaporation, and cathodic arc. In a thermal evaporation process, vapors are produced by evaporating the coating material to be deposited using direct electrical resistance, radiation, or by eddy current. In electron beam (e-beam) evaporation, the coating material (target) is evaporated using an impinging beam of high-energy electrons. Even a laser beam can be used to evaporate or ablate a target.
The substrate, located at an appropriate distance from the evaporation source, can be heated and/or biased to the desired potential using a dc/rf power supply.
Evaporation is carried out in vacuum in a pressure range of 1.3×10^{-3} to 1.3×10^{-8} Pa (10^{-5} to 10^{-10} torr). In this pressure range, the mean free path (MFP) is very large (5 to 10^{5} m, or 16 to 3×10^{5} ft) as compared to the source-to-substrate distance. Hence, the evaporated atoms essentially undergo a collisionless line of sight transport prior to condensation on the substrate, leading to thickness build-up directly above the source that decreases steeply away from it. Planetary substrate holders are therefore used in some cases to even out the vapor flux on multiple substrates. In some cases, an appropriate gas such as argon at pressures of 0.7 to 30 Pa is introduced into the chamber to reduce the mean free path so that vapor species undergo multiple collisions during transport from the source to substrate, thus producing reasonably uniform thickness coatings on the substrate. This technique is called gas scattering evaporation or pressure plating.

The transition of solids or liquids into the vapor phase is an atomistic phenomenon. It is based on thermodynamics and results in an understanding of evaporation rates, source-container reactions, and the accompanying effect of impurity introduction into the vapor state, changes in composition during alloy evaporation, and stability of compounds.
The rate of evaporation is given by the Hertz-Knudsen equation:

$$dN_e/A_e dt = \alpha_v (2\pi mkT)^{-1/2}(p^* - p) \quad (2.1)$$

where α_v is the evaporation coefficient; $dN_e/A_e dt$ is the number of molecules evaporating from a surface area, A_e in time, dt; p^* is the equilibrium vapor pressure at the evaporant surface; p is the hydrostatic pressure acting on the surface; m is the molecular weight; k is Boltzmann's constant; and T is the absolute temperature. Evaporation coefficient, α_v, is very dependent on the cleanliness of the evaporant surface and can range from very low values for dirty surfaces to unity for clean surfaces. [Bun92]
For reasonable deposition rates (100 to 1000 nm/min, or 1000 to 10^5 Å/min) at a source-to-substrate distance of 200 mm (8 in.), the vapor pressure should be about 1.3 Pa (10^{-2} torr). The source temperature should be adjusted to give this value of the vapor pressure.
The directionality of evaporating molecules from an evaporation source is given by the cosine law.
For the ideal case of deposition from a clean, uniformly emitting point source onto a plane receiver, the rate of deposition varies as $(\cos \theta)/r^2$ (Knudsen's cosine law), where r is the radial distance of the receiver from the source and θ is the angle between the radial vector and the normal to the receiver direction.

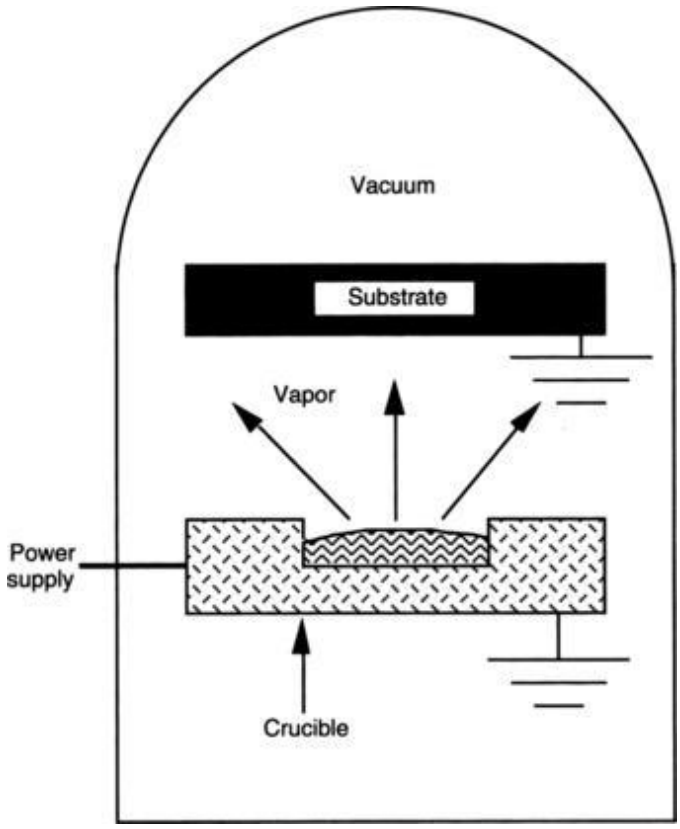

Figure 2.1: Resistance-heated evaporation process [ASM Handbooks]

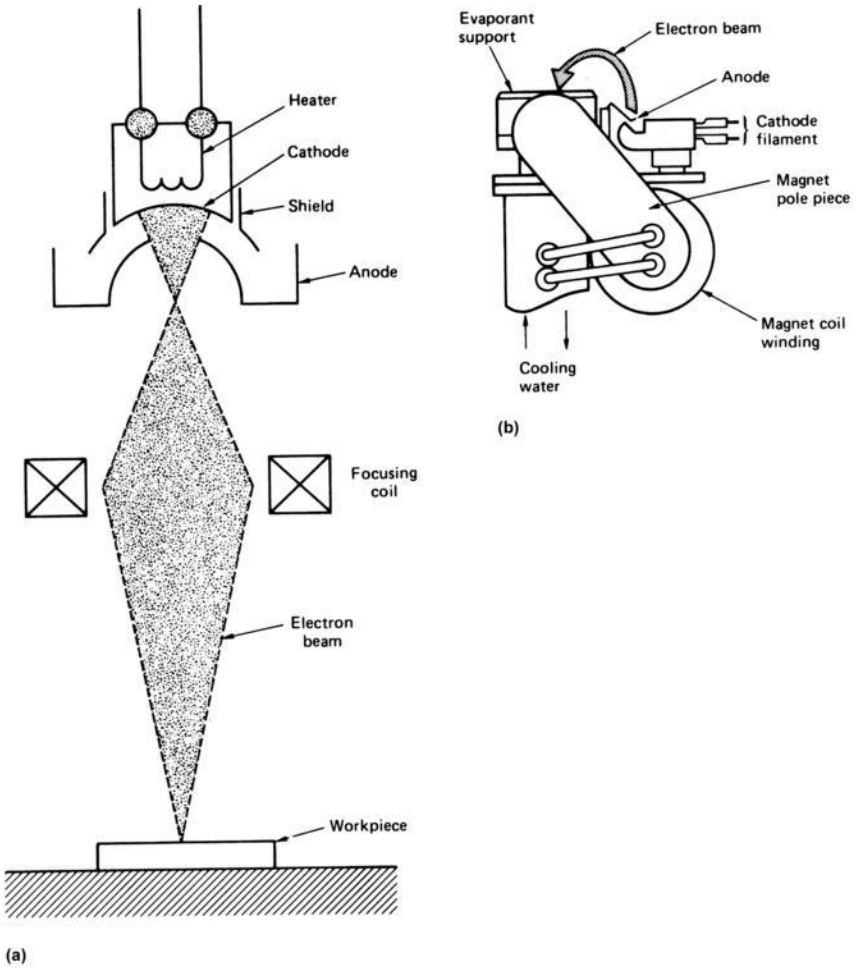

Figure 2.2: Electron beam components for evaporation process. (a) Linear focusing gun. (b) Bent-beam electron gun with a water-cooled evaporant support. [ASM Handbooks]

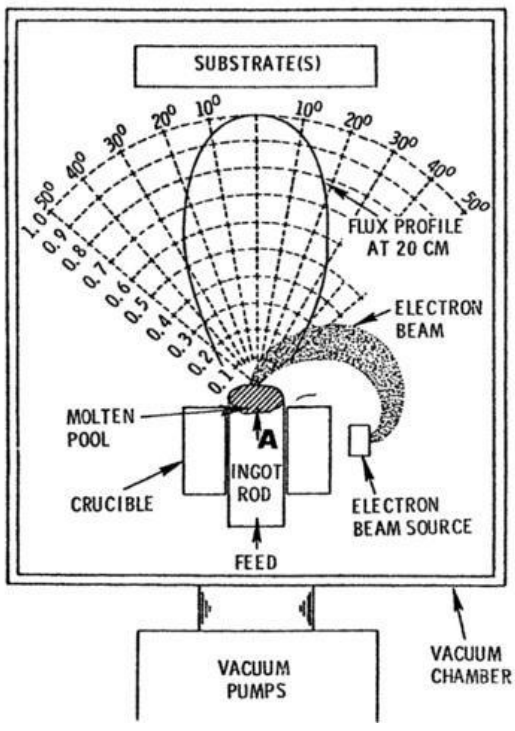

Figure 2.3: Electron beam physical vapor deposition wit magnetically bent electron beam showing the flux profile of the evaporated material. [ASM Handbooks]

In the simplest form of evaporation PVD, the evaporated material undergoes an essentially collision-less line-of-sight transport prior to condensing on the surface of the component being coated. Uniformity of the thickness of the coating can be a concern with evaporative processes, and movement of the surface with respect to the source frequently is required to ensure adequate uniformity. The rate of evaporation is a function of the vapor pressure of a coating material and the ambient pressure. The following table indicates the various temperatures at which certain metals have a vapor pressure of 1.33 Pa (10^{-2} torr), sufficient for coating.

Metal	Temperature	
	°C	°F
Cadmium	265	509
Zinc	345	653
Lead	715	1319
Silver	1030	1886
Aluminium	1220	2228
Copper	1260	2300
Gold	1400	2552
Chromium	1400	2552
Iron	1480	2696
Cobalt	1520	2768
Nickel	1530	2786
Titanium	1740	3164
Hafnium	2400	4352
Molybdenum	2530	4586
Tungsten	3230	5846

Table 2.1: Temperature at which selected metals exhibit a vapor pressure of 1.33 Pa (10-2 torr)

2.1.1 Reactive Evaporation

Direct evaporation of ceramic materials is difficult because of their low vapor pressure and their tendency to dissociate. Reactive evaporation methods therefore are employed to produce coatings of carbides, nitrides, or oxides. In this process, an appropriate gas such as oxygen or nitrogen is introduced into the region where the metal is being evaporated. The reaction to produce the desired coating occurs on the surface of the component.

2.1.2 Activated Reactive Evaporation

In an activated reactive evaporation process, a gas plasma is generated in the space between the evaporation source and the substrate and a reactive gas introduced into the plasma. The high-energy electrons in the plasma ionize the gaseous precursors of the coatings, increasing the rate of reaction on the surface of the substrate, forming the coating.

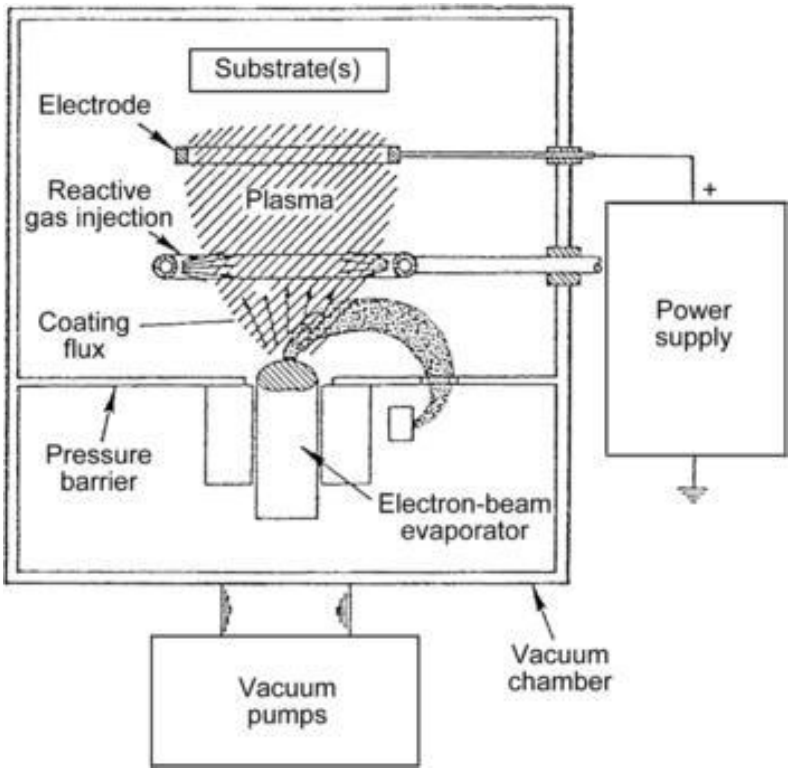

Figure 2.4: Activated reactive evaporation. [ASM Handbooks]

2.1.3 Cathodic Arc Deposition

An electric arc discharge (cathodic arc) also can be used to vaporize a target material. An electric arc is initiated on the target with a high-frequency discharge and then switched to direct current (typically 40 to 300 A at 15 to 40 V), with the target as the cathode. The discharge causes localized melting and vaporization of the target. A high percentage of the vaporized atoms are ionized, 20 to almost 100%, with some particles or ions having multiple charges. However, some macroparticles (clusters of atoms) also may be ejected from the surface. If the macroparticles impinge on the substrate surface, they cause significant imperfections in the coating: poorly bonded lumps and porosity. Because most of the vaporized coating material is ionized, its path can be bent using a magnetic field and directed to the substrate. The macroparticles, however, are only partially ionized or not at all and travel in a straight line. Thus, the substrate can be effectively shielded from the macroparticles by placing it out of the line-of-sight of macroparticles, creating filtered arc or steered arc deposition. Moreover, by negatively biasing the substrate, the ionized coating atoms can be accelerated toward the substrate, thereby improving the coating microstructure and providing greater coverage of the substrate than unbiased line-of-sight deposition, that is, greater throwing power. Velocities of over 10^5 m/s can be achieved.

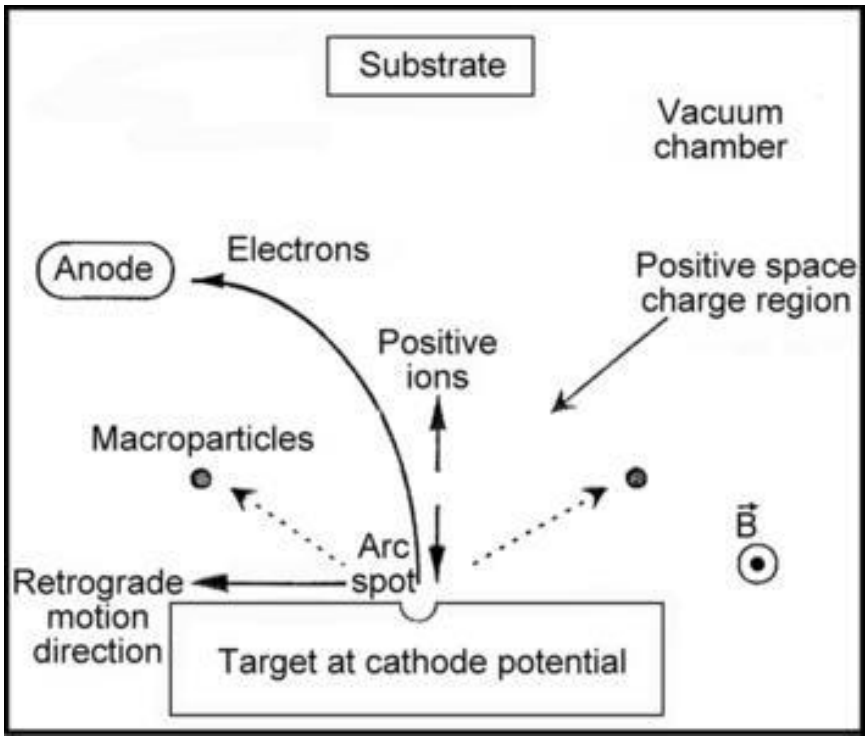

Figure 2.5: Cathodic arc deposition. [ASM Handbooks]

The advantages of cathodic arc deposition include:

- High ionization of target material, which facilitates filtered arc evaporation to eliminate macroparticles and biased deposition for improved bonding, microstructures, and throwing power
- Higher bond strength than sputtering
- High deposition rate
- Simple sources (targets) that can be placed in any orientation within the coating chamber

The disadvantages of cathodic arc deposition include:

- Macroparticle spits that can be eliminated with a filtered arc or steered arc
- Target must be electrically conductive
- Limited throwing power that can be increased with substrate biasing
- A vacuum process with concomitant capital and maintenance costs, batch processing

Applications for evaporated PVD coatings include wear and corrosion resistance, microelectronics, optical coatings for abrasion resistance, reduction of glare, and decorative purposes. The materials deposited by evaporation include pure metals and alloys from single or multiple sources and inorganic compounds either directly or by reaction, including the following:

- *Carbides:* TiC, HfC, ZrC, VC, W_2C, TaC
- *Nitrides:* TiN, HfN, ZrN, CrN, AlCrN, AlTiN
- *Carbonitrides:* TiCN
- *Amorphous structures:* Diamond-Like Carbon (DLC)

2.1.4 Ion Plating

Ion plating is the generic term applied to atomistic film-deposition processes in which the substrate is biased negatively and the coating material and/or an inert gas (argon) is ionized in a gas plasma. The substrate surface and/or the depositing film thus are subjected to a flux of high-energy ions sufficient to cause changes in the interfacial region or film properties, compared to the non-bombarded deposition. Such changes may be in the adhesion of the film to the substrate, film morphology, film density, film stress, or the coverage of the surface by the depositing film material. Ion plating usually is performed in argon at a pressure of approximately 1.33 Pa (10^{-2} torr).

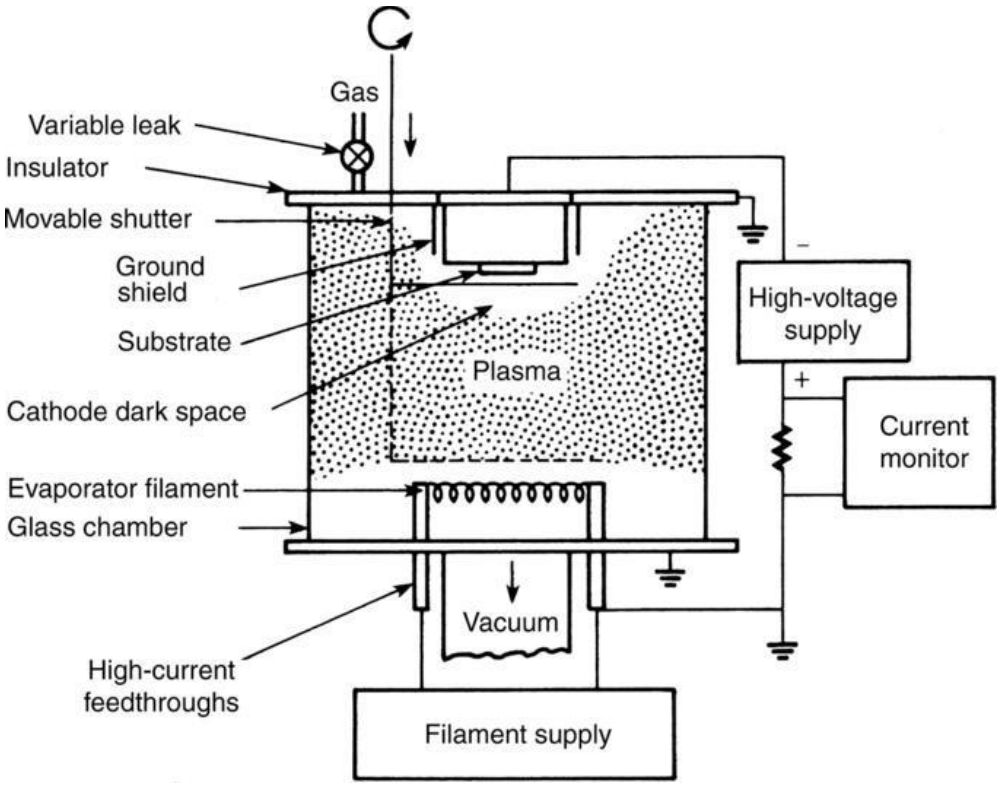

Figure 2.6: Ion plating process. [ASM Handbooks]

A negative potential in the range of 2 to 5 kV is applied to the workpiece so that it becomes the cathode of a glow discharge formed between it and the grounded parts of the apparatus. The resulting argon ion bombardment initially cleans the surface and continues while the coating material is evaporated into the plasma and deposited onto the substrate. This continuing bombardment increases nucleation and improves adhesion. Gas scattering is the major factor in ensuring uniform coating distribution. Applications of ion plating include optical coatings on glass and plastic, coating of electrical contacts, and lubricious metals.

2.2 Sputtering

Sputtering is a phenomenon that occurs when material is removed from a surface through momentum exchange when the surface is bombarded by energetic particles, usually argon ions, drawn from a gas plasma. It essentially is a mechanical process and does not rely on melting or sublimation. There are a number of different types of sputter coating processes (also known as cathode sputtering), including diode, triode, ion beam, and magnetron sputtering. The simplest is diode sputtering in which ions (usually argon ions)

are accelerated toward the cathode target, where their impact ejects atoms from the surface in an inelastic exchange of energy. The target material then flows to the substrate, forming the coating.

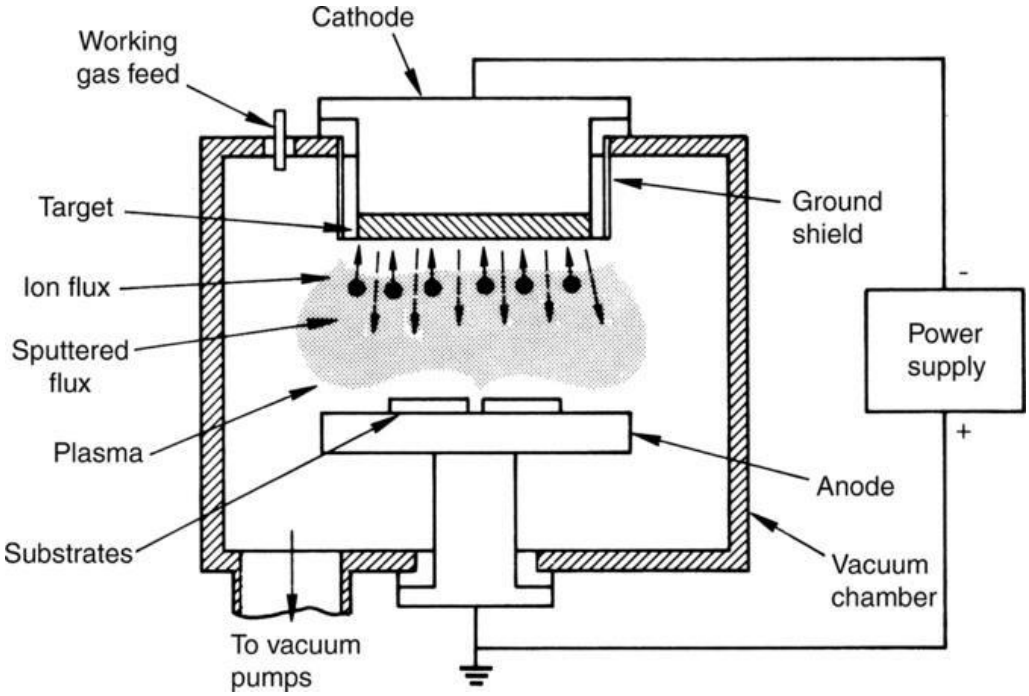

Figure 2.7: Scheme of sputter coating. [ASM Handbooks]

In magnetron sputtering, a magnetic field is used to increase the length of flight of the electrons in the plasma and hence the probability of collision with the argon or other atoms and their subsequent ionization. This increases the amount of ionization in the gas plasma and hence the rate of sputtering. Magnetron sputtering includes planar, unbalanced, gun, cylindrical post, and linear configurations.

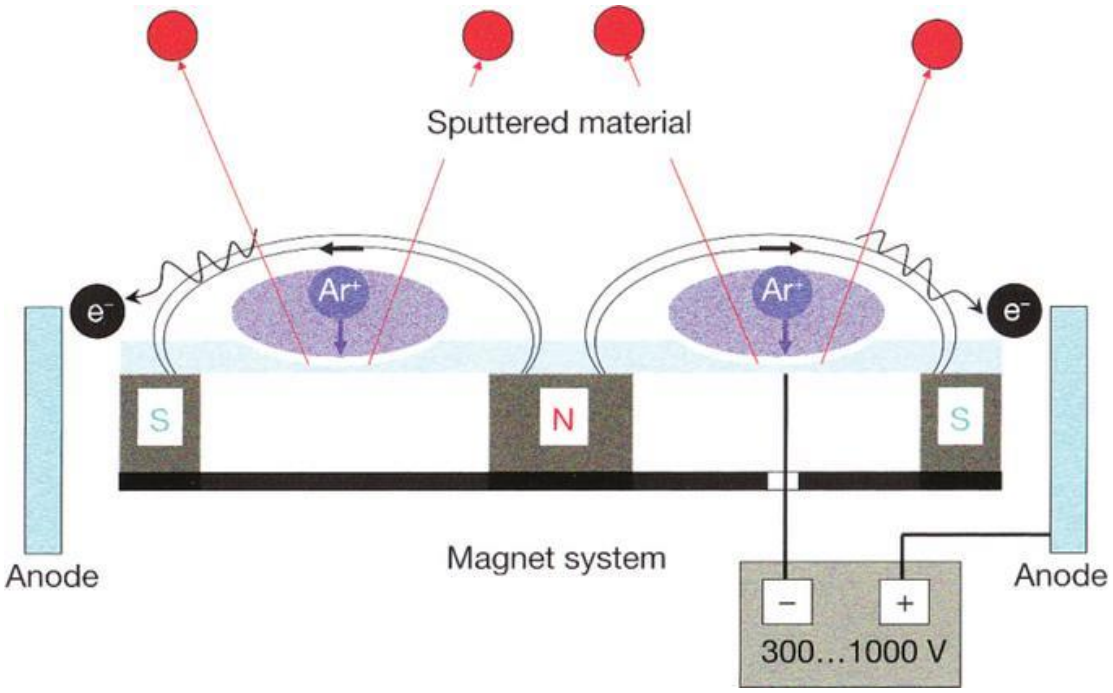

Figure 5: Structure of a magnetron used for coating. [ASM Handbooks]

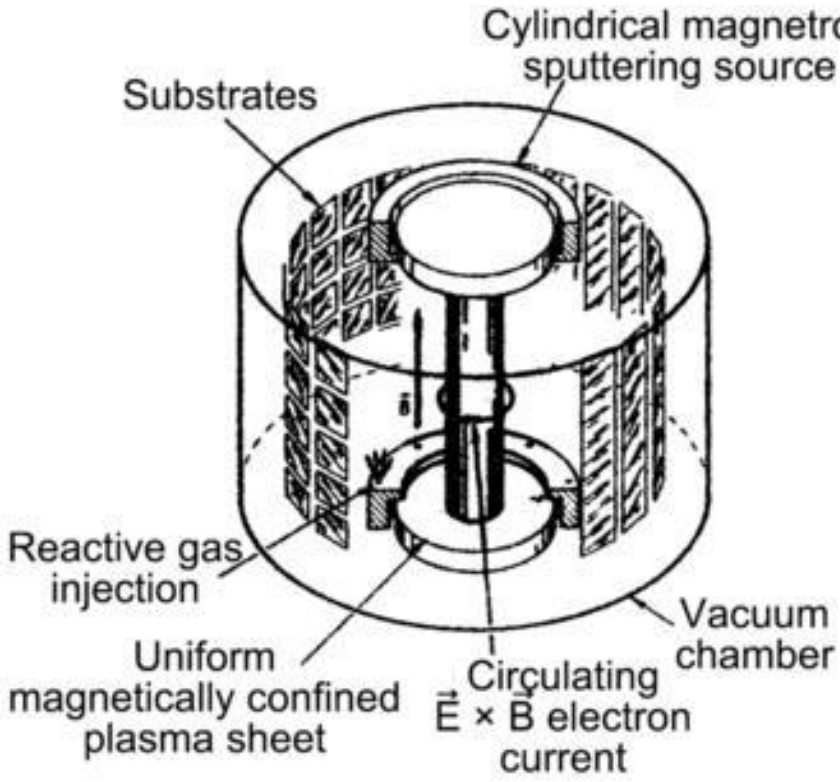

Figure 2.9: Cylindrical magnetron sputtering. [ASM Handbooks]

Direct current (dc) power may be used to generate the glow discharge plasma with a voltage of approximately 300 to 1000 V if the target is conductive. More advanced systems use pulsed dc (unipolar pulsed dc) or bipolar power sources. Radio frequency (RF) power at 13.56 MHz is used when the target is nonconductive. Although both the electrons and ions are accelerated in alternating directions, the electrons, because of their very low mass compared to the ions, are accelerated to a greater extent and tend to accumulate on the surface of the target. This provides a negative charge on the target surface, resulting in the attraction of the positive ions, high energy impact of the ions, and sputtering of the target material. The bombarding species generally are ions of a heavy inert gas such as argon, generated in a glow discharge plasma with a pressure between 0.133 and 13.33 Pa (10^{-3} and 10^{-1} torr) and an applied voltage of approximately 300 to 600 V dc. Because the coating material is passed into the vapor phase by mechanical rather than chemical or thermal processes, virtually any material can be used for sputtered coatings.

As with evaporative methods, ceramics can be deposited by sputtering techniques with the addition of reactive gases and close control of the process.

Variations on the aforementioned basic processes can result in coatings formed by:

- Employing a target that is a mosaic of several materials
- Employing multiple targets simultaneously, of identical or different materials
- Employing multiple targets sequentially to create a layered coating
- Biasing the substrate as an electrode to cause surface ion bombardment during deposition, in order to remove loosely bonded contamination or to modify the structure of the resulting coating. This is known as bias sputtering.
- Employing a gas to introduce one of the coating materials into the chamber. This process is known as reactive sputtering. It permits metal targets and dc power supplies to be used for preparing coatings of nonconducting compounds.

The advantages of sputter coating include:

- Almost any material can be sputtered—dc for metals, RF for nonconductors.
- Multiple materials can be sputtered simultaneously using a mosaic or multiple targets to obtain an alloy coating.
- Reactive sputtering can be used to obtain compound coatings.
- Multiple materials can be sputtered sequentially to produce layered coatings.
- The substrate can be biased to modify the coating with ion bombardment or to increase throwing power.

The disadvantages of sputter coating include:

- Sputter coating is a vacuum process with concomitant capital costs and throughput limitations.
- It has lower deposition rates than thermal spray and some other processes.
- Target costs and utilization efficiency are a concern.

Some of the many applications of sputter coatings include wear and corrosion resistance, amorphous optical films, piezoelectric transducers, photoconductors, and luminescent films. They also are used in microelectronics as dielectrics, conductors, passivation layers, oxidation barriers, and microcircuit photolithographic mask blanks.

2.2.1 Ion Implantation

Ion implantation or ion beam deposition is a development in sputtering technology. It consists in a process conducted in a vacuum (133×10^{-6} to 33×10^{-3} Pa, or 10^{-6} to 10^{-5} torr), wherein a beam of ions is directed and accelerated toward the substrate. Typically, the ions are accelerated to an energy of 100 keV. The ions penetrate to an average depth of 0.1 μm (4×10^{-6} in.) and a maximum depth of 0.25 μm (1×10^{-5} in.). Nitrogen and carbon are the most frequently used elements for implantation. Heavier ions can be implanted with sufficient ion acceleration; however, they are not widely used commercially.

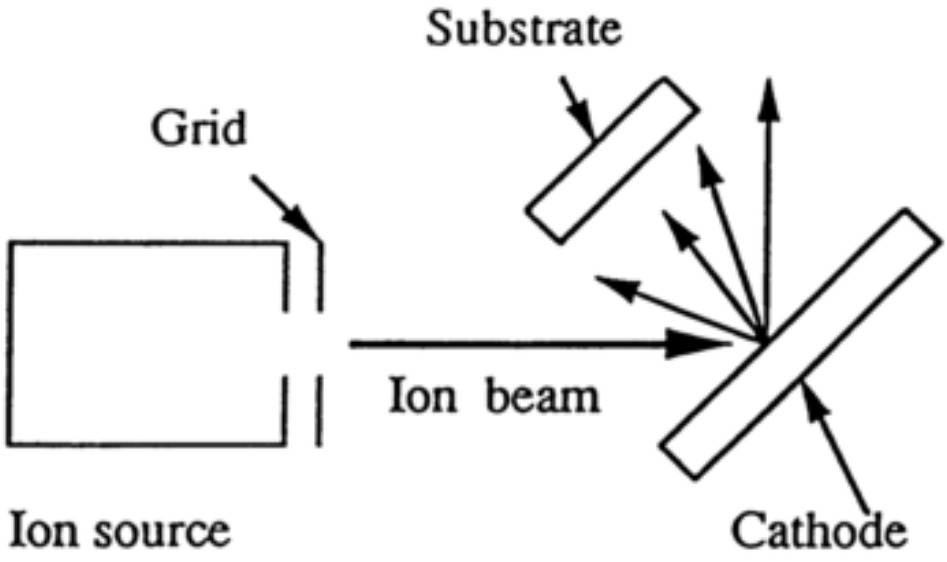

Figure 2.10: Ion beam sputter deposition. [ASM Handbooks]

Advantages of ion beam sputtering includes:

- Excellent adhesion
- A high-purity deposit resulting from the use of low operational pressures (~13 mPa, or 0.1 mtorr)
- Very low substrate hearing effects because the substrate is not in contact with the plasma.

In this technique, an ion beam of high energy (hundreds to thousands of electron volts) extracted from the ion source is directed at a sputtering target of the desired material. An inert or reactive gas is used for the ion beam source. The substrate is suitably located to collect the sputtered species from the sputtering target.

Because the substrate can be isolated from the plasma generation source, ion beam deposition permits independent control over the substrate temperature, gas pressure, and the type of particle bombardment of the growing film. In addition, it is possible to control the energy and the target current density independently in this technique, whereas it can be done only by varying the working gas pressure in conventional glow discharge sputtering technology. The new unbalanced magnetron sputtering systems can also independently vary the ion flux and energy.
In general, the deposition rate in ion beam sputtering (50 nm/min, or 500 Å/min) is lower than that in conventional sputtering. The reason for this low rate is mainly due to the low beam current in the conventional (dual-grid) ion beam sputtering system. This low beam current can be greatly increased by using a single-grid system. In some applications it has been obtained a very high deposition rate (>90 nm/min, or 900 Å/min, for selected materials such as aluminium, copper, and so on) using single-grid ion beam sputtering. A small coverage of deposition area due to the small ion beam size (~10 mm, or 0.4 in.) is another drawback of the ion beam sputtering. The beam size can be increased to ~100 mm (~4 in.) by adaptation of space-type ion engine technology.

Chapter 3

Coating process operations at Oerlikon Balzers

In a coating service centre, the PVD depositon is just one step of a longer production process, which involves different operations and phases.
In this chapter is briefly described the operations route in the Oerlikon Balzers tools service centre located in Brugherio (Italy).

3.1 Acceptance – Incoming Inspection

The process starts from acceptance of the customer shipment.
All packages are opened, and their content is inspected in order to make sure that everything correspond to what is reported on the delivery note for every order line.
Once the production order is inserted in the ERP system, the operations list is printed. This document will follow the pieces during all the manufacturing steps.
Tools are then inspected one by one, under magnifying lens, in order to detect any defect (damages, dents, dirt, burrs, rust etc…) which would make that part not compliant with customer request and object of possible claims.

3.2 Cleaning

A sequence of surface treatments is required to make the surface such that coating adhesion on the substrate is maximized.
The first operation is surface cleaning. Parts are firstly placed specific baskets, then processed in an automated cleaning line, formed by a sequence of tanks filled with several aqueous solutions, with different detergent and anticorrosive agents.

Figure 3.1: Cleaning line manufactured by Novatec.

The cleaning line combines the effect of detergent solutions with ultrasonic cleaning: ultrasonic waves generated in each tank produce the phenomenon of cavitation.
A sound wave is produced when a solitary or repeating displacement is generated in a sound conducting medium, such as by a "shock" event or "oscillatory" movement.
The movement of liquid molecules in each tank caused by ultrasonic generator can be represented as the movement of a coil: the molecules in the medium are influenced by adjacent molecules in much the same way that the coils of the spring influence one another. A scheme of this example can be found in figure 3.2.
Let us assume the source of the sound in the model is at the left. The compression generated by the sound source as it moves propagates down the length of the spring as each adjacent coil of the spring pushes against its neighbour.
It is important to note that, although the wave travels from one end of the spring to the other, the individual coils remain in their same relative positions, being displaced first one way and then the other as the sound wave passes.
As a result, each coil is first part of a compression as it is pushed toward the next coil and then part of a rarefaction as it recedes from the adjacent coil.
In much the same way, any point in a sound conducting medium is alternately subjected to compression and then rarefaction. At a point in the area of a compression, the pressure in the medium is positive. At a point in the area of a rarefaction, the pressure in the medium is negative.

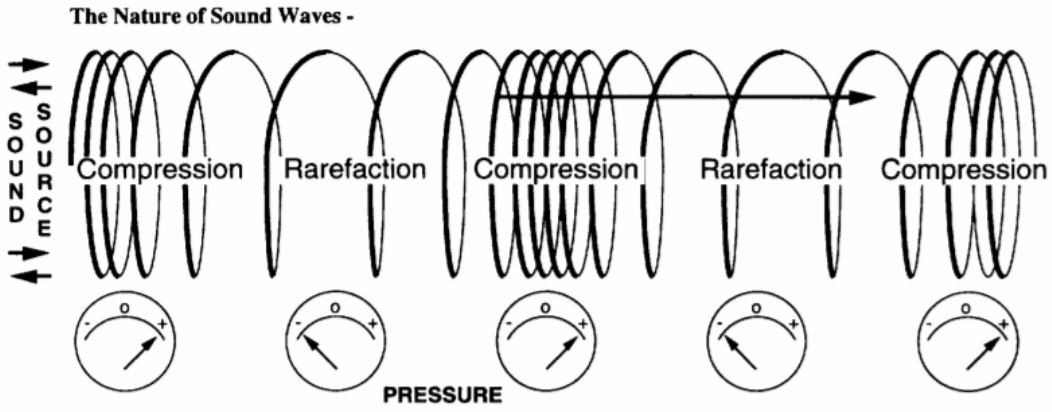

Figure 3.2: Coil analogy for molecules interaction driven by soundwaves [Fuc95]

In elastic media such as air and most solids, there is a continuous transition as a sound wave is transmitted. In non-elastic media such as water and most liquids, there is continuous transition as long as the amplitude or "loudness" of the sound is relatively low.
As amplitude is increased, the magnitude of the negative pressure in the areas of rarefaction eventually becomes sufficient to cause the liquid to fracture because of the negative pressure, causing a phenomenon known as cavitation, explained in figure 3.3.

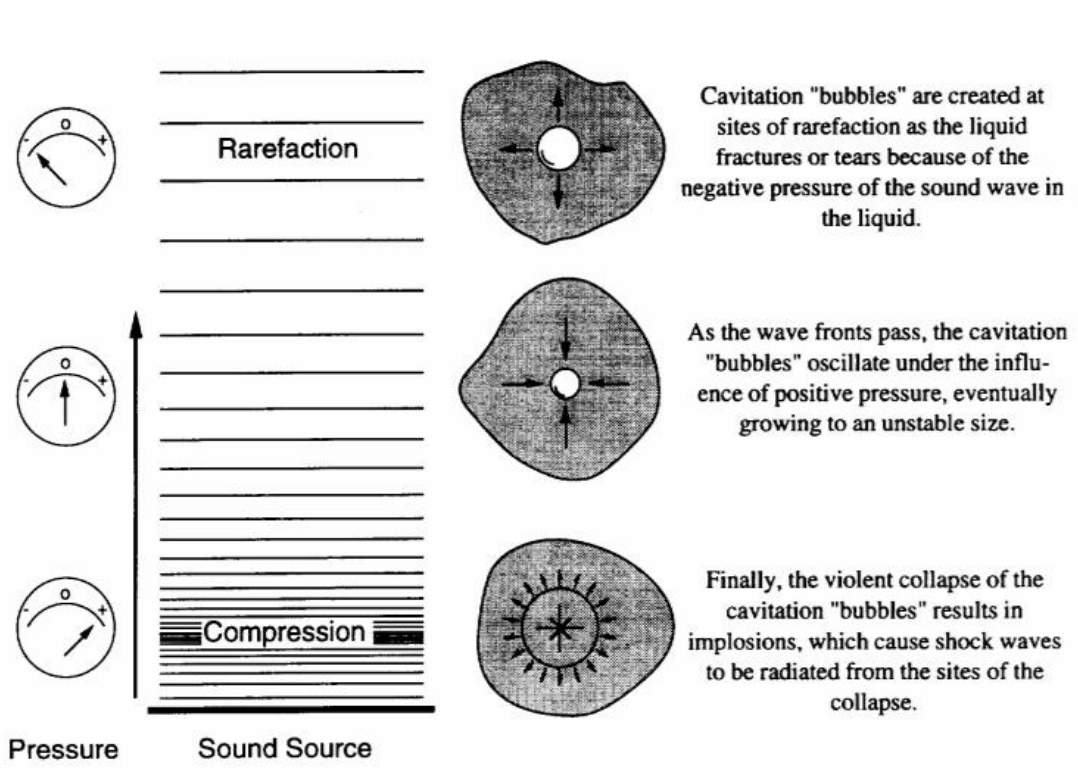

Figure 3.3: Cavitation generated by ultrasonic waves [Fuc95]

The collapse and implosion of myriad cavitation bubbles throughout an ultrasonically activated liquid result in an highly enhanced cleaning action.
Cleaning in most instances requires that a contaminant be dissolved (as in the case of a soluble soil), displaced (as in the case of a non-soluble soil) or both dissolved and displaced (as in the case of insoluble particles being held by a soluble binder such as oil or grease). The mechanical effect of ultrasonic energy can be helpful in both speeding dissolution and displacing particles. Just as it is beneficial in cleaning, ultrasonics is also beneficial in the rinsing process. Residual cleaning chemicals are removed quickly and completely by ultrasonic rinsing.

3.3 Blasting pre-treatment

In the service centre many tools types are processed, and in order to maximize their yield, some product families require additional pre-treatments before the coating step.
Blasting is an operation consisting of propelling a stream of abrasive material against the substrate surface, under high pressure.
Glass beads (SiO2) blasting is carried on substrates, such as gear cutting tools, that could show the presence of burrs on the cutting edge not removed by the customer.
Deburring is an operation of primary importance: if burrs are not removed, once the coated tool is employed in a manufacturing process, they will tend to detach from the rest of the substrate, leaving a local uncoated area which is more exposed to wear consumption with respect to the coated rest of the piece.
Another pre-treatment is blasting with fine grains of corundum (Al2O3), carried out to ensure a good coating adhesion on roughly finished or oxidized surfaces.
This treatment leads to a constant surface quality and less variation in terms of performances of coated tools.

11-14 µm fine grains are employed to obtain an abrasive effect and remove approximately a thin layer of 0.5 µm from the substrate. This allows to keep constant the geometrical characteristics and tolerances of a part.
After micro blasting, surfaces are generally smoother, with no oxide residuals, cutting edges have a homogeneous margin, slightly rounded. All of these characteristics enhance the local adhesion of PVD coating and increase the performance of the tool.
In some cases, blasting treatment can be performed in an additional step, after the coating phase. The final treatment is requested for some cathodic-arc coating types, in order to remove local irregular coating material clusters, called droplets.

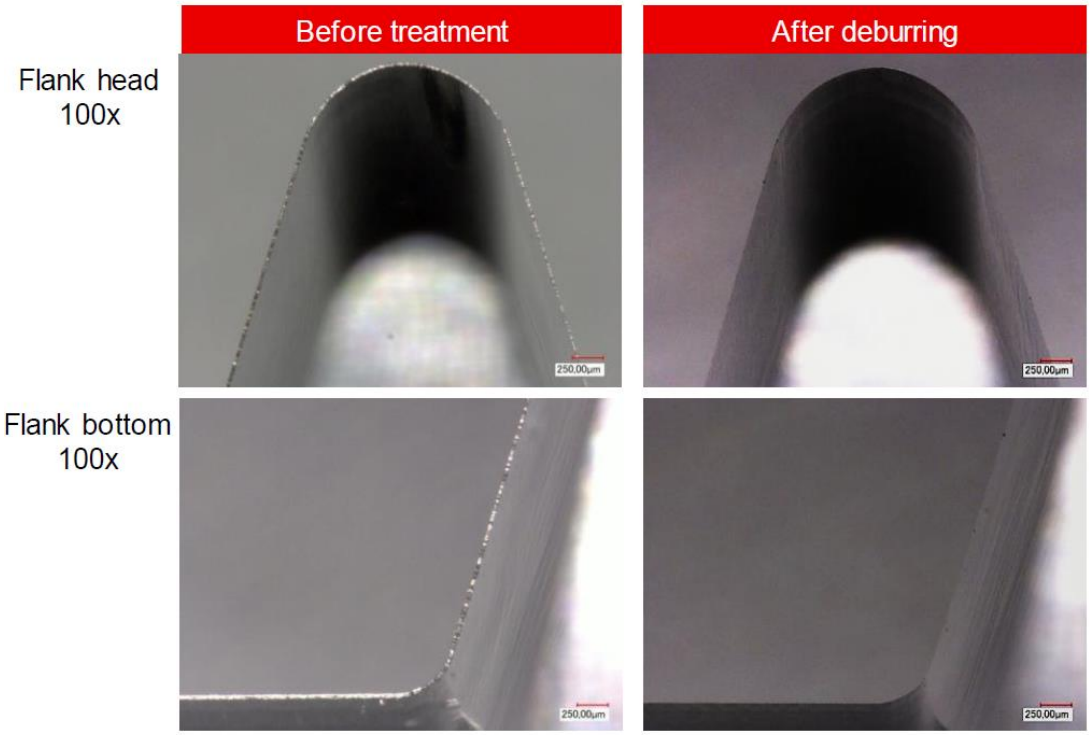

Figure 3.4: Cutting edges of a gear cutting hob before (left) and after (right) deburring treatment. [Courtesy of Oerlikon Balzers]

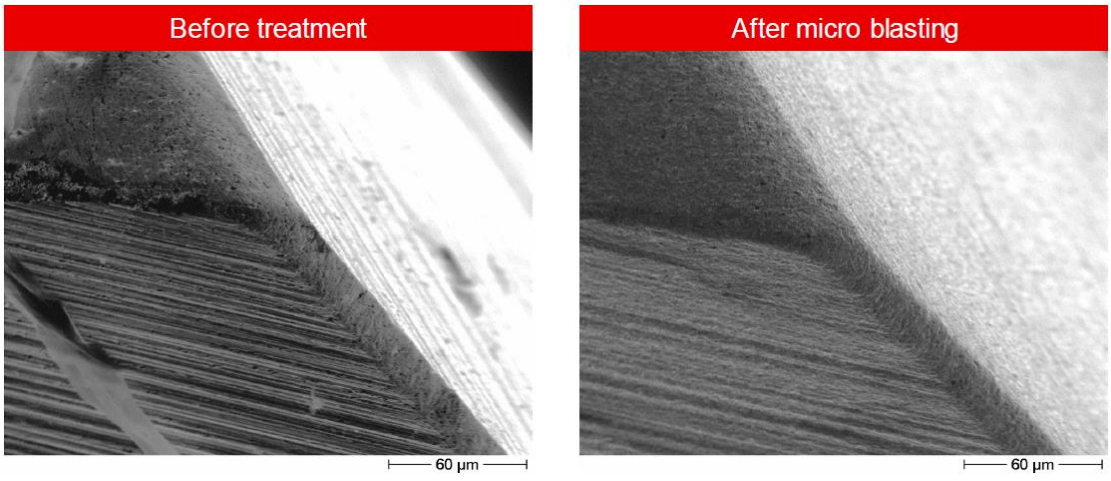

Figure 3.5: Effect of micro blasting on a cemented carbide drill. [Courtesy of Oerlikon Balzers]

3.4 Process steps inside the coating machine

Tools are transferred to the coating room, where they are mounted on a multi-spindle carousel.
The operator chooses the appropriate fixturing for each specific tool type: substrates are mounted on the coating fixtures on the base of the application, geometry and size. As an example, shank tools are placed on fixtures such that they follow a 3-fold rotation around tool axis, spindle axis and carousel axis.
Once all the substrates of the batch are mounted on the carousel, a rotation test is performed, to make sure that pieces do not collide to each other or with fixture equipment due to planetary rotations.

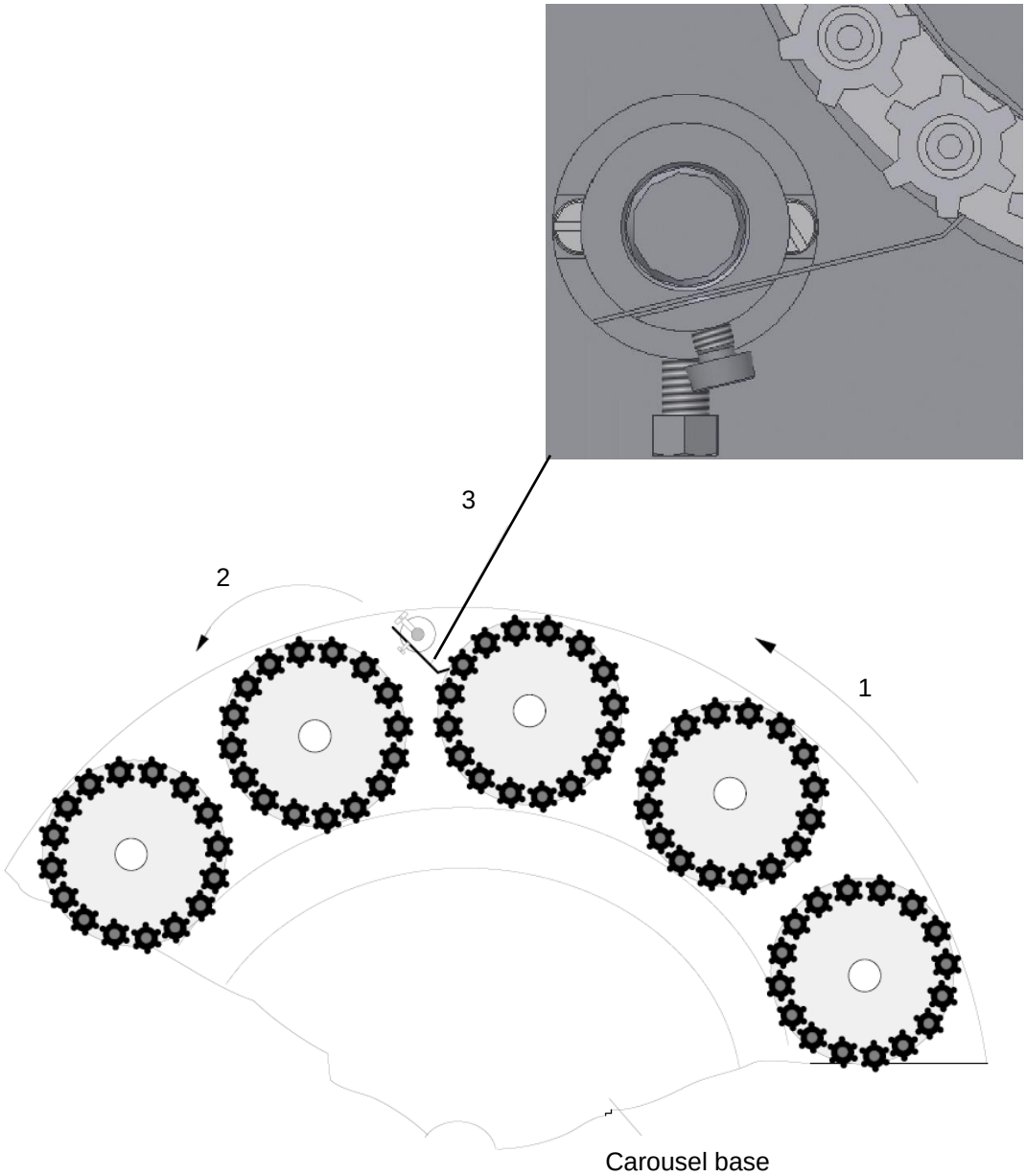

Figure 3.6: Triple planetary rotations of a of a coating fixture. The 3-fold rotation is actuated through flicker fingers acting on small gear wheels placed underneath sleeves in which each shank tool is mounted on. [Courtesy of Oerlikon Balzers]

If the test is passed, the batch is transferred inside the coating machine.
Once the machine door is closed, the operator launches the coating recipe through a control panel.

3.4.1 Pumping

The first step of the coating machine is pumping: a system of vacuum pumps evacuates the gas contained in the vessel, reaching a pressure of 10^-3 mbar (Balzers BAI 1200).
Pumping system control the income/outcome of gases not only in the first pumping phase, but also in the following steps (heating, etching, coating).
Pumping time is variable, as it depends on the condition of the chamber and on moisture content. Time of this phase is reduced if heaters, walls, carrousel and fixtures are clean.

3.4.2 Heating

Next step is **heating**: during this phase the chamber is heated with resistive heaters up to defined temperature levels. Temperature control is performed by 3 thermocouples positioned at specific heights inside the coater.
Heating is required to remove moisture residuals on substrates, and to reach optimal temperature for subsequent phases.
In case of incorrect cleaning or pre-treatments, due to pressure and temperature condition in this phase, out-gassing from the heaters, tools, fixtures or carrousel occurs.
This phenomenon results in a pressure increase, which comes immediately after the heater has started.
Therefore, in the whole heating time, the pumping system is on and removes the outcoming gases, restoring the desired pressure conditions.
From the process and product quality point of view it is essential that all the air and moisture is removed.
If the pumping and heating is very long, all will come out, but it is not economic: the processes get to long, therefore a constant maintenance of the coater and a high grade of cleanliness is always required.

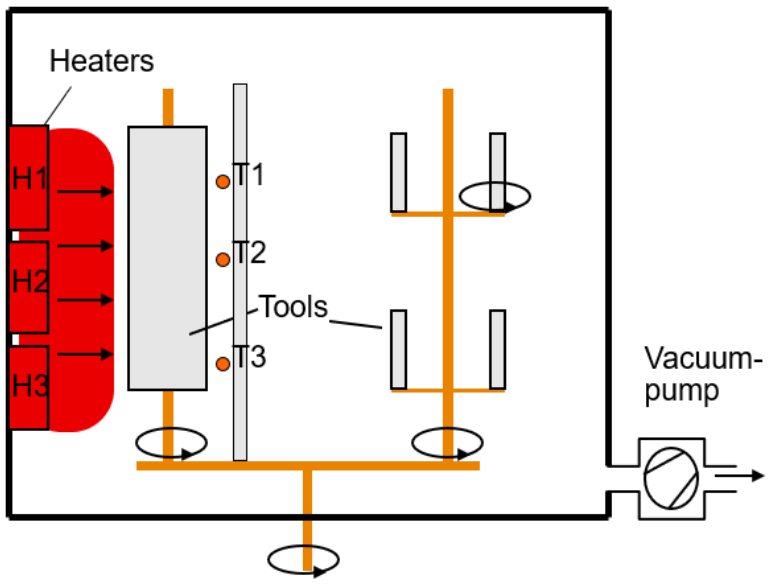

Figure 3.7: Radiation heating. Tools rotate continuously, in order to achieve a uniform temperature.

[Courtesy of Oerlikon Balzers]

3.4.3 Plasma ignition

The subsequent etching and coating steps involve the action of plasma.
Plasma is a mixture of gaseous atoms or molecules (i.e. Argon or Hydrogen), positively charged ions and negatively charged electrons.
A plasma is necessary for the formation of PVD hard coatings.
At temperatures of about 500°C, Titanium, Aluminium and other metals will only react with Nitrogen in a plasma. Without the action of the ionized gas, there is no possibility to form metal nitrides.
Only in CVD, whose process is carried out at more than 900°C, that reactions are possible. The problem is that at such high temperatures metal alloys like tool steel are softened or melted.
Because in the plasma the atoms are split into ions and electrons, reactions are possible at temperatures between 200°C - 500°C. This is the overwhelming advantage of PVD over CVD.
To create plasma, splitting atoms and molecules into positive ions and electrons, a large amount of energy is required.
Plasma can be formed with high temperatures or with electric discharges.
In the high vacuum conditions of the coating machine, gas to be ionized flows the ionisation chamber.
Here is placed a heated filament which emits electrons (thermionic effect).
If a voltage is applied between the cathode (filament) and the anode (placed inside the chamber), the electrons are attracted by the anode (positive voltage). On their way to the anode the electrons collide with gas atoms and produce ions and electrons, in this way a plasma is generated.

3.4.4 Etching

In atmospheric conditions a very tiny oxide layer is formed on substrates.
Etching ensures a perfectly cleaned surface just prior to coating. This is essential for a good adhesion. During this phase, a layer of about 0.1 µm is removed from tools.
Substrates are etched by argon ions, attracted to the tools as they are on a negative voltage of approximately -200 V.
Argon is a noble gas and has no chemical effect on the tool, the action is purely mechanical: by the impact of the argon ion a particle from the tool surface is sputtered off. Mechanical etching with Argon removes a very small amount of the substrate material, therefore, the surface becomes a little dull. A polished surface will not remain polished when the etching time is long.
Only Ar ions can produce this effect, because hydrogen ions, helium ions and electrons are too light to produce a sputter effect.
The plasma is ignited between the filament and the auxiliary anode (figure 3.8).
The removed material is deposited on the walls, fixtures and tools, it is not possible to pump it out of the chamber.
As the material is not only deposited on the walls, it can stick also on area where etching is less effective (i.e. cavities or between the teeth of a hob). Adhesion is not improved by very long etching time.
A contaminated area can emit electrons, like a heated cathode. Due to the high substrate voltage (-200V) an arc discharge is ignited.
If there are electrons additional ions are produced and the arc increases. The only reason why most of the ions go into the direction of the cathode is that there electrons are

produced. The potential on the substrate is more negative and when electrons are emitted the ions will immediately form an arc to this “new cathode”.
In this arc, tool material evaporates, and the tool is destroyed. This arc exists as long as the substrate voltage is applied.
An arc protection device shuts down the substrate voltage and stops the arc. This arc protection can only stop the arc but not prevent it.
If the substrate voltage rises, the arc can start again, and the arc protection shuts down the substrate voltage. The result is an oscillating substrate voltage.
Due to this oscillating voltage the etching effect is reduced. This has a major impact on the adhesion and the performance of the tool.
Arcing can be prevented ensuring that equipment, fixtures and tools are cleaned and dried properly. Special care must be taken in presence of cooling ducts or blind holes.
Keeping clean the internal surface of the chamber, such as the anode, prevent short circuit and arcing due to lack of conductivity.
Reduction of this phenomenon is also performed by the action of heating, and in the combined effect of Argon/Hydrogen etching. Etching with Hydrogen ions is not a mechanical process like Argon etching, as it is based on chemical reactions.
A plasma is necessary in order to split the hydrogen molecules (H2) into hydrogen atoms (H). The hydrogen atoms react with the carbon and oxygen in the contamination and form the gaseous compounds.
In these chemical reactions between the organic contamination and the hydrogen, gaseous hydrocarbons are formed and pumped out of the chamber. The tool surface becomes very clean. No material from the metal is removed, only the contaminations.
It is also possible to remove oxidation by the hydrogen plasma. Oxide layers are removed through reduction reactions.
As Hydrogen atoms can penetrate into holes and remove organic contamination, in many cases an outgassing process in the furnace can be avoided by using a hydrogen plasma in heating or etching. Chemical cleaning can remove organic layers, like plastic residuals or oil, on the other hand it is ineffective against inorganic contaminations.

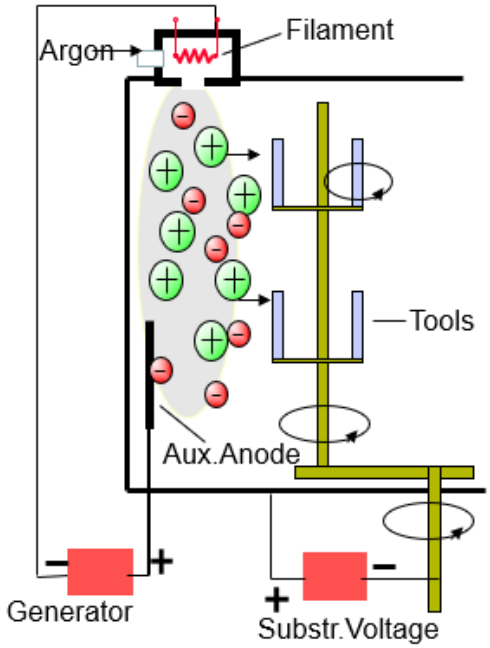

Figure 3.8: Scheme of plasma ignition and etching in a BAI 1200 coater. [Courtesy of Oerlikon Balzers]

3.4.5 Coating

Coating phase is composed by three "sub steps": evaporation of coating material, ionization and transfer to substrate surface.
The first two phases are generally jointed in one single step.
The arc is ignited by an electrical contact between the ignitor finger and the target. A small amount of material evaporates. In the vapour of the evaporated material, the arc can be sustained.
Arc does not stay in a fixed position, but it moves rapidly across the target surface.
The movement can be random or controlled by a magnetic field.
The magnetic field is optimised for the target material and has a big influence on the structure of the coating. Therefore, different magnet systems are used.
Coating physical and chemical proprieties can change with the variation of the magnet system.
When the target is eroded the distance to the magnet becomes smaller, and this results in a higher magnetic field at the surface. The movement of the arc is faster, evaporation rate is reduced and fewer droplets are produced.
One downside of the arc evaporation process is that if the cathode spot stays at an evaporative point for too long it can eject a large number of macro-particles clusters, called droplets. These droplets are detrimental to the performance of the coating, due to poor adhesion to the rest of the layer. Droplets can also reduce the local micro-hardness of the coating, since they are not nitrided.

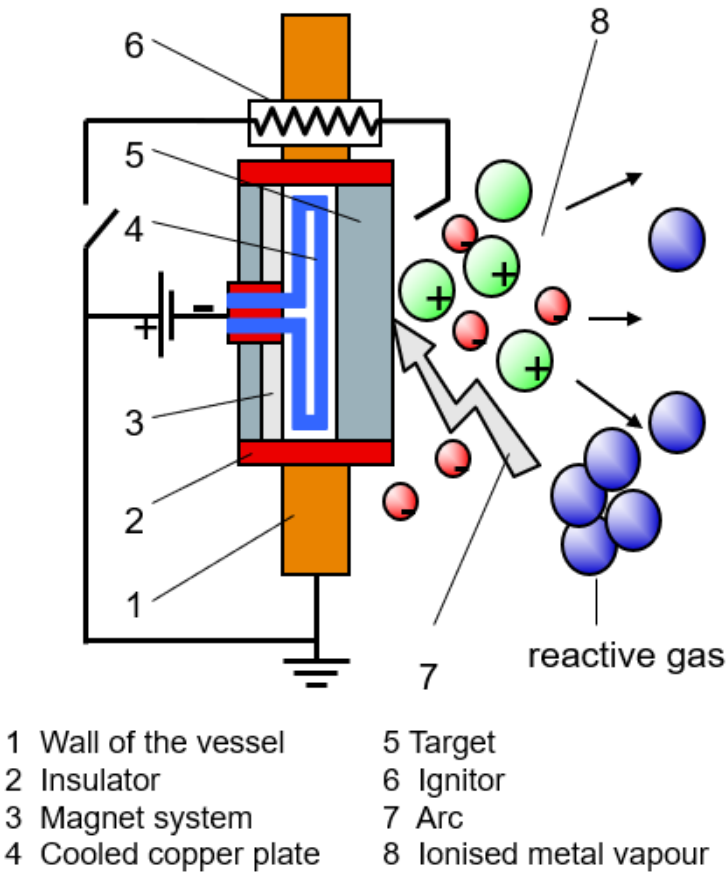

Figure 3.9 Scheme of arc evaporation and ionization of the coating material. [Courtesy of Oerlikon Balzers]

When the arc source is ignited, the target material is evaporated and ionised to nearly 100%. Gasses pumped into the chamber are also ionised.
In order to accelerate the transfer of particles to the substrate surface, a negative voltage is applied to the tool. This voltage is between 40V and about 150V and depends on the process. Tools are on a negative bias; therefore, ions are attracted to them.
In addition to that, coating adhesion is enhanced due to the high ionisation.
The evaporation rate depends on the material, the source current and on target consumption. Evaporation rate is reduced when the target is eroded because the distance to the magnets changes, expected values are in the range of 0.1g/min for TiAl and about 0.2 g/min for Titanium.
Increasing the arc intensity leads to higher evaporation rate, but on the other hand many droplets will be formed.
The material is melted, but only a small area, therefore the sources can be installed in any direction.

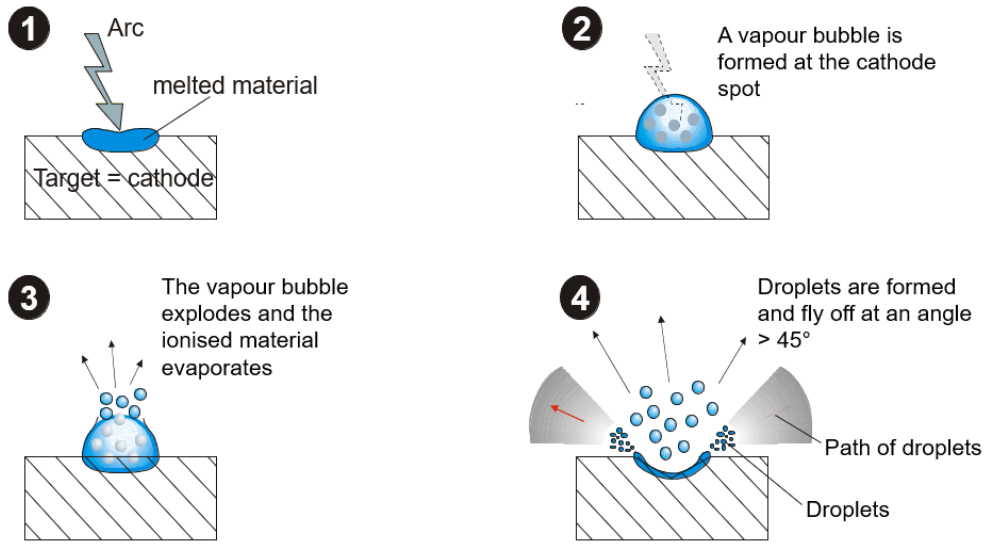

a)

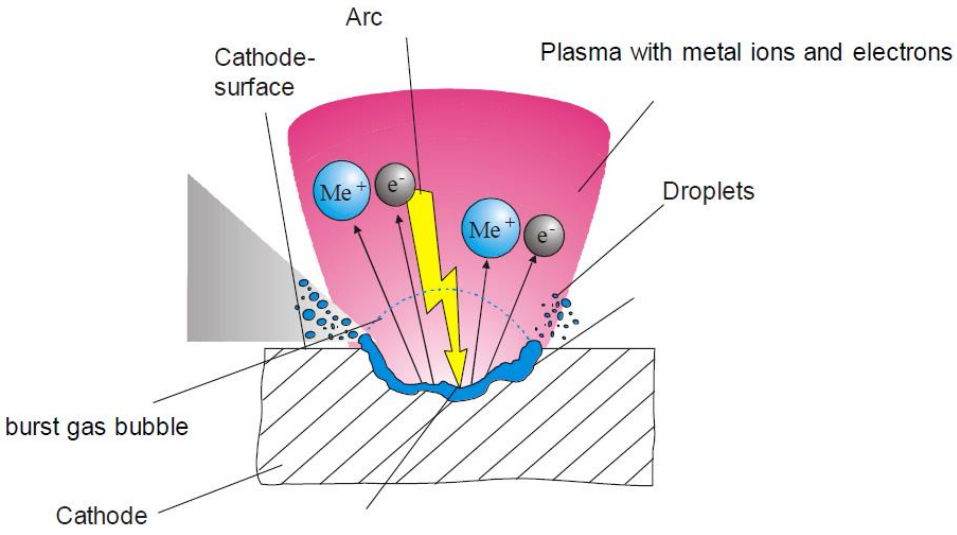

b)

Figures 3.10 a) The sequence of arc evaporation. b) Ions are transferred to surfaces flowing in plasma.

[Courtesy of Oerlikon Balzers]

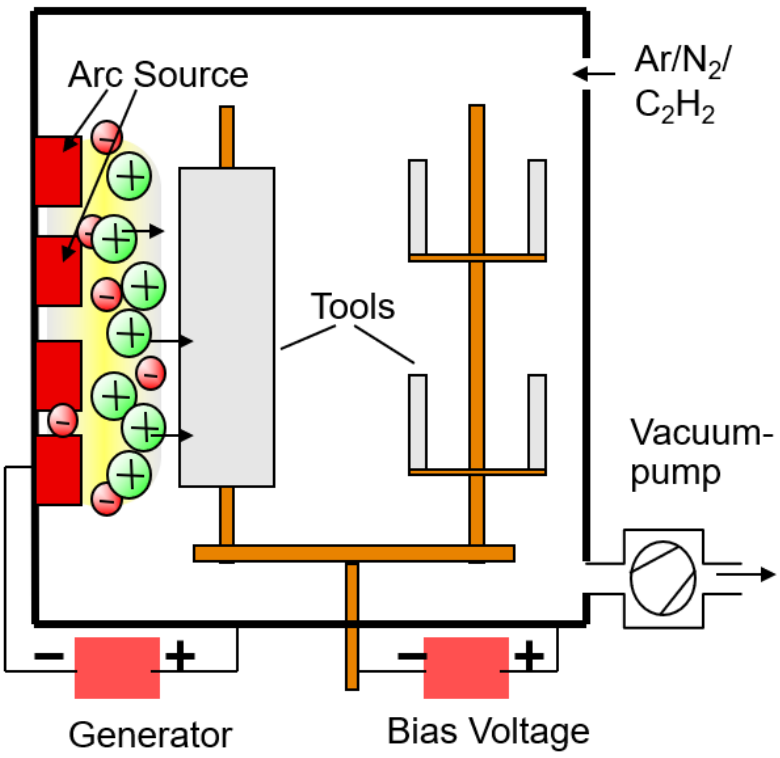

Figure 3.11: Ions produced by arc evaporation attracted to negative bias voltage in tools.

[Courtesy of Oerlikon Balzers]

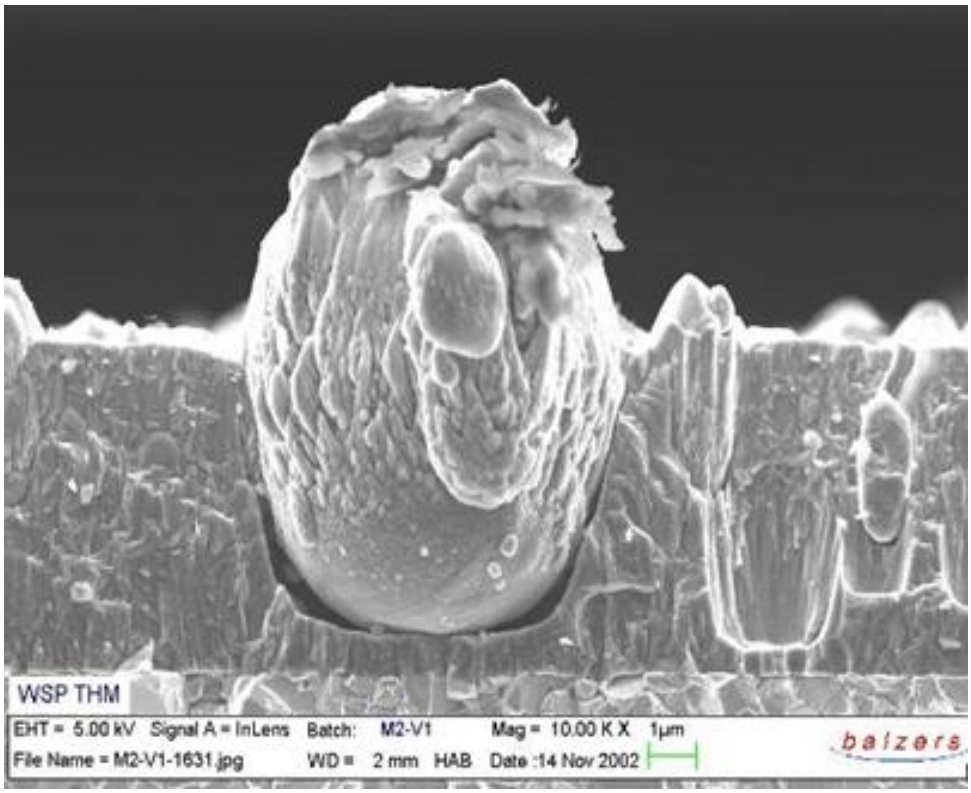

Figure 3.12: SEM image of a droplet deposited inside the coating layer. [Courtesy of Oerlikon Balzers]

3.4.6 Cooling

Once the coating step is concluded, the machine starts cooling down.
Cooling is necessary in order to avoid uncontrolled discoloration due to the reaction with oxygen in the air, as coating colour depends on the process temperature.
As an example, Titanium nitride layer will get slightly darker when exposed to air at high temperature
Cooling is carried out trough cooling gasses, like nitrogen or helium.
Due to the higher heat conductivity, cooling with helium is faster than with nitrogen.

3.5 Post treatments and outcoming inspection

At the end of the machine cycle, ambient pressure is restored, then if the coated tools do not require additional treatments, they are removed from fixtures and transferred to the shipping area.
Some parts, like gear cutting tools, may require additional micro blasting or brushing. These last surface treatment lead to an optimization of surface conditions, removing excess of droplets and friction, therefore increasing tribological performances of coating.
Finally, before packing, tools are visually inspected under magnification lens, in order to check coating uniformity, presence of flaking, discoloration, dents or other local defects.

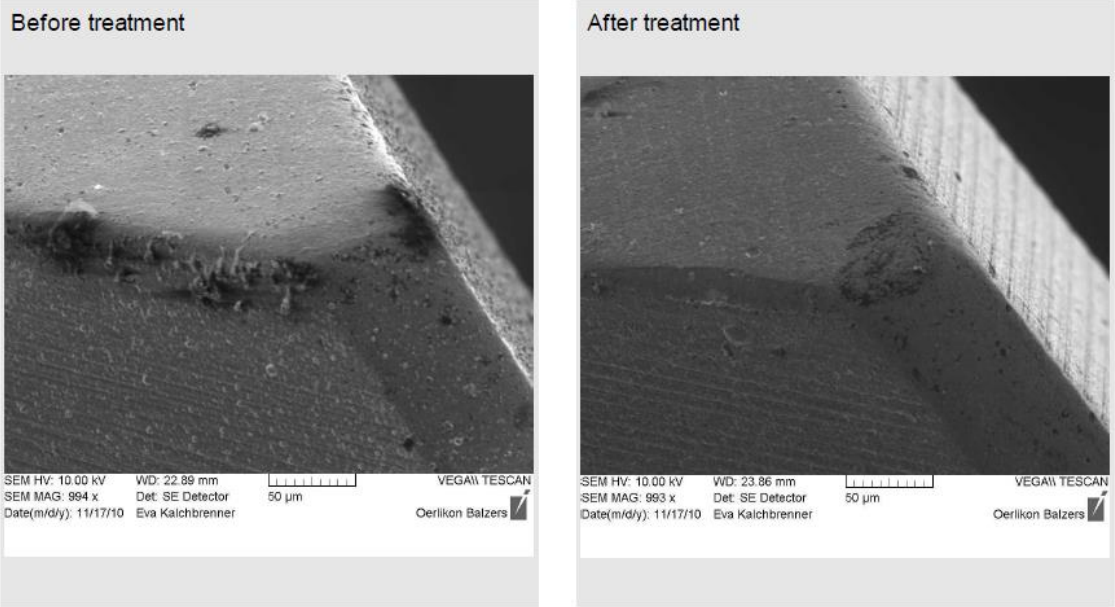

Figure 3.13: Cutting edge before and after post treatments, observed at SEM. [Courtesy of Oerlikon Balzers]

Chapter 4

The problem: Layer thickness control on a PVD coating process

4.1 State of the art

4.1.1 A model for deposition rate

The mechanisms which regulate layer thickness are strictly related to deposition rate. Indeed, integrating along time the deposition rate, it is possible to obtain the coating thickness.
[Mah00] provides a model for deposition rate in an evaporation process.
PVD sources are fundamentally characterized with a beam intensity, i.e. the number of particles per second being emitted by the source in directions within a solid angle dΩ ($\sin\theta\, d\theta\, d\varphi$), expressed in a spherical coordinate system, where θ is the polar angle and φ the azimuthal angle.

For an ideal small evaporation source:

$$J_\Omega = \frac{z\,\delta A\,\cos\theta}{\pi} \tag{4.1}$$

Where z is the thermal equilibrium impingement rate of the evaporant at the temperature of the source, δA is the source area.
For this cosine law to hold, the source of the area must be both flat (planar) and small. What makes a source "small" is simply that the linear extent of its source area $\delta A^{1/2}$ must be sufficiently small compared to the distance of the surface.
The impingement rate z is the number of collision per unit area per second a material in a gaseous state makes with a surface, and is expressed as:

$$z = \frac{P}{\sqrt{2\pi mkT}} \tag{4.2}$$

Where P is the gas pressure, m is the particle mass, k is Boltzmann's constant, and T is the temperature.
Many practical applications of PVD require the use of a large substrate, and a high uniformity of the deposit. These circumstances demand a "large" sources (one for which the lateral size is not negligible relative to the distance to the substrate). For a large-sized source, a differential beam intensity is assigned to each infinitesimal area element of the source dA. A large source can be assumed as "ideal" if the differential source areas have the differential beam intensity of the ideal small source and if dJ_Ω is uniform across the source area:

$$dJ_\Omega = \frac{z\,dA\,\cos\theta}{\pi} \tag{4.3}$$

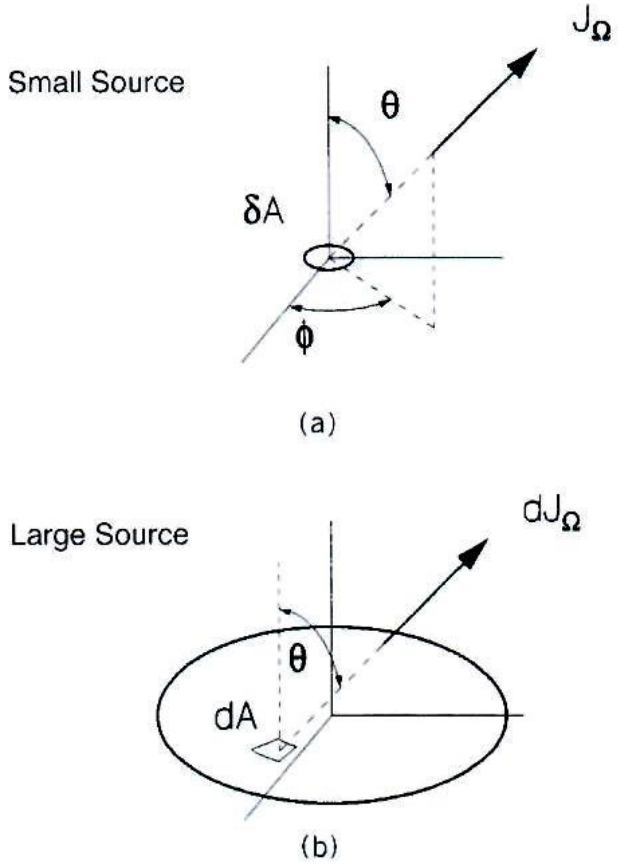

Figure 4.1: Physical vapor deposition sources are fundamentally characterized with (a) a beam intensity or (b) a differential beam intensity [Mah00]

When combined with specific substrate configurations, a given beam intensity leads to a specific *incident flux* and a lateral film thickness profile across the substrate.

The local incident flux of particles onto a receiving surface for a given beam intensity depends on the position and orientation of the surface.
It is intended as the rate of arrival of particles per unit area of the receiving surface $[length^{-2} \cdot time^{-1}]$.
From solid geometry, a surface element dA_s subtends a solid angle $d\Omega$ with respect to a point *O* which is given by

$$d\Omega = \frac{(\vec{R}\cdot\vec{n})dA_s}{R^3} \tag{4.4}$$

$\vec{R}$ is the vector from *O* to the element and $\vec{n}$ is the unit vector inwardly normal to the element. Multiplying J_Ω by $d\Omega$ and then dividing by dA_s gives a general expression for the local incident flux onto the receiving surface:

$$j_i = \frac{J_\Omega(\vec{R}\cdot\vec{n})}{R^3} \tag{4.5}$$

If the angle between $\vec{R}$ and $\vec{n}$ is β, then the expression for the incident flux reduces to

$$j_i = \frac{J_\Omega \cos\beta}{R^2} \tag{4.6}$$

This depends on the beam intensity, β, and on the distance to the point of deposition. β is called *deposition angle.*

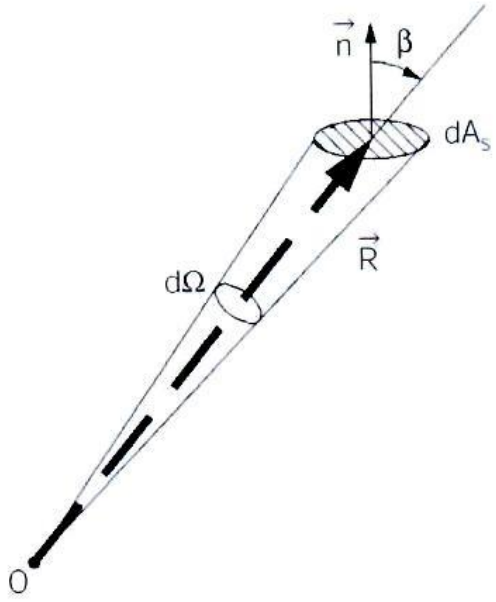

Figure 4.2: A differential area element subtends a differential solid angle dΩ with respect to a point O. [Mah00]

Now let us define the *condensation coefficient* (α_c), which is the fraction of the incident flux that actually condenses on the substrate.

$$j_c = \alpha_c j_i \tag{4.7}$$

Where j_c is the *condensation flux.*
For most strongly bonded elements, such as refractory metals, α_c is very close to unity. However, in molecular, ionic or other complex and anisotropic solids, α_c can be very much less than unity. The condensation coefficient can vary, depending on the temperature and on the structure of the surface as it may have been affected by previous condensation or adsorption.
Given a net condensation flux, the *deposition rate* can be defined as the rate of change of the film thickness in the direction perpendicular to the local surface, along $\vec{n}$.
This may be calculated with the continuity equation, which expresses the principle of conservation of matter:

$$\nabla \cdot j_c = \frac{-\partial n_f}{\partial t} \tag{4.8}$$

Referring to figure (4.3), j_c goes to zero over a distance equal to the thickness of one monolayer of the condensing film (α_{ml}). Thus, the divergence of the condensation flux may be approximated with $-j_c/\alpha_{ml}$. At this growth front, the density of film which has condensed increases at a rate given by n_f/t_{ml}, where t_{ml} is the monolayer deposition

time, given by a_{ml}/v_n, and n_f is the atomic density of the deposited element. v_n is the speed of the growth front in the normal direction, or *deposition rate*.

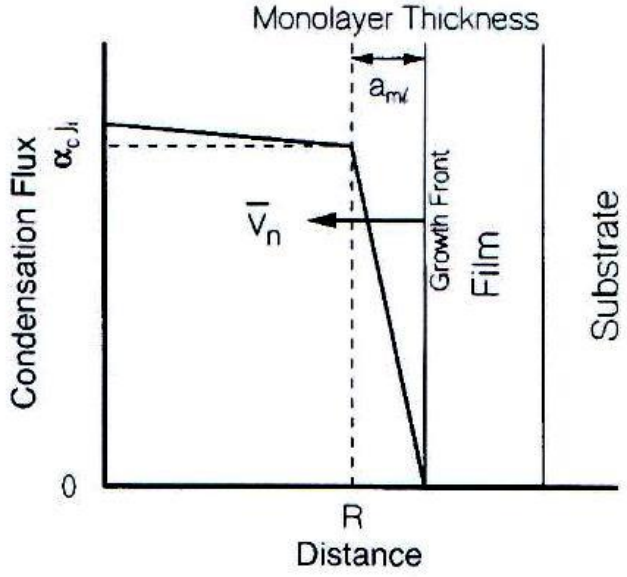

Figure 4.3: Application of the continuity equation to calculation of film growth rate. The condensation flux falls to zero over a distance equal to the monolayer thickness. [Mah00]

The continuity equation previously introduced (4.8) becomes $\frac{j_c}{\alpha_{ml}} = \frac{n_f v_n}{a_{ml}}$, which may be solved for deposition rate:

$$v_n = \frac{j_c}{n_f} \tag{4.9}$$

Example:

Let us assume an evaporation and deposition of an aluminium film on a certain substrate in a defined configuration with condensation flux equal to $0.703\ \text{Å}^{-2} \cdot s^{-1}$.
The atomic density of crystalline aluminium is $0.0602\ \text{Å}^{-3}$.
The deposition rate is then equal to $v_n = \frac{0.703\ \text{Å}^{-2} \cdot s^{-1}}{0.0602\ \text{Å}^{-3}} = 11.7\ \text{Å/s}$.

4.1.2 Deposition with substrate rotation

In PVD, the material is vaporized from a target and deposited around the vacuum chamber. In contrast to chemical vapor deposition, the vapor flux in PVD is highly directional since the material originates from a spatially located area, i.e., from a target or more specifically from a small part of the target (e.g. racetrack or cathode spot). Due to directionality of the flux the material is deposited on those surfaces that are in the line-of-sight of the target. Line-of-sight deposition is disadvantageous for many applications where a whole or most of the substrate with complex shape must be covered. Several approaches are used to improve uniformity of the line-of sight deposition.
One way is to increase scattering of the vaporized material and thus reduce the directionality of the flux. This can be achieved by working at high pressures where mean

free path of the vaporized species is significantly smaller than the target–substrate distance.

Majority of PVD techniques operate at pressures where the mean free path of vaporized species is larger or comparable to the target–substrate distance therefore only a small amount of material reaches shaded areas of a substrate through scattering. High-pressure PVD techniques have been developed to improve uniformity of deposition but such methods are rarely used in practice and acceptable uniformity can be realized only for specific deposition parameters and substrate geometries. More importantly, high-pressure PVD techniques are disadvantageous compared to low-pressure PVD techniques since the scattering reduces energy of the vaporized species and thus produces thin films with lower quality. The surface of a large substrate can be uniformly coated if several targets are positioned around the substrate. This approach is not practical since it requires several target sources and is only useful for coating one substrate; coating several substrates would be less uniform due to shading by other substrates. The only practical way to improve the uniformity of the deposition in the line-of-sight processes is to rotate the substrates. Rotation ensures that substrates, which usually have complex geometry, are more or less uniformly exposed to the vaporized material. Practically all PVD systems employ some type of substrate rotation which is performed by a turntable. Typically turntables perform planetary type of rotation where turntable rotates around its central axis, while the substrate holders and substrates rotate around their axes.

Industrial PVD systems can be classified into the designs where substrates are always in the view of the vaporization sources and designs where they are not. In the first type of the design the target sources are normally positioned on the bottom of the deposition chamber whereas the turntable is on the top of the chamber. In this configuration, substrates are always in the view of the targets but only one side of the substrate is coated. If the opposite side has to be covered then substrates are turned around and deposition is repeated. PVD systems with the top-bottom design are mainly utilized for the deposition of optical coatings (e.g. anti-reflective coatings on lenses). [M. Panjan]

In the literature, the influence of the substrate rotation on the deposition and properties of coatings has not been given much attention; there are only a few studies on this topic. J. E. Mahan portrays a model suitable for system in which the substrate is always on the line of sight of the source, i.e. one or more rotation axes are normal with respect to the source plane.

The usual forms which substrate movement takes are *simple* and *planetary rotations*; the latter is a combination of simultaneous rotations about two different axes.

A small source may be thought of as zero-dimensional; using several small-area sources gives a superposition of zero-dimensional sources. Simple substrate movement converts it to one-dimensional, a line as seen by a selected point on the substrate.

The average value of the incident flux at a certain point on a rotating substrate is obtained from an expression based on:

$$j_{i,av} = \frac{1}{T} \int_0^T J_\Omega\,(t)\,\frac{\cos\beta(t)}{[R(t)]^2}\,dt \tag{4.10}$$

where T is the period of the substrate rotation. This single integral shows the effectively one-dimensional nature of the source. Planetary movement would effectively convert it to a two-dimensional source, replacing the single interval of (4.10) by a double integral. Thus, large sources may be simulated to a limited extent by moving the substrate during deposition.

Let us consider a rotating planar substrate situated off the axis of an ideal small source.

At a moving point $P'(r', \varphi')$ on the rotating substrate, the contribution to the incident flux during an incremental rotation $d\varphi'$ is

$$dj_i = \frac{z\delta A \cos\theta \cos\beta}{\pi R^2} \cdot \frac{d\varphi\prime}{2\pi} \tag{4.11}$$

with $\theta = \beta$, $\cos\theta = \cos\beta = h/R$, where $R^2 = h^2 + (W - r'cos\varphi')^2 + (r'sin\varphi')^2$. All dimensions are defined in the picture (4.4).

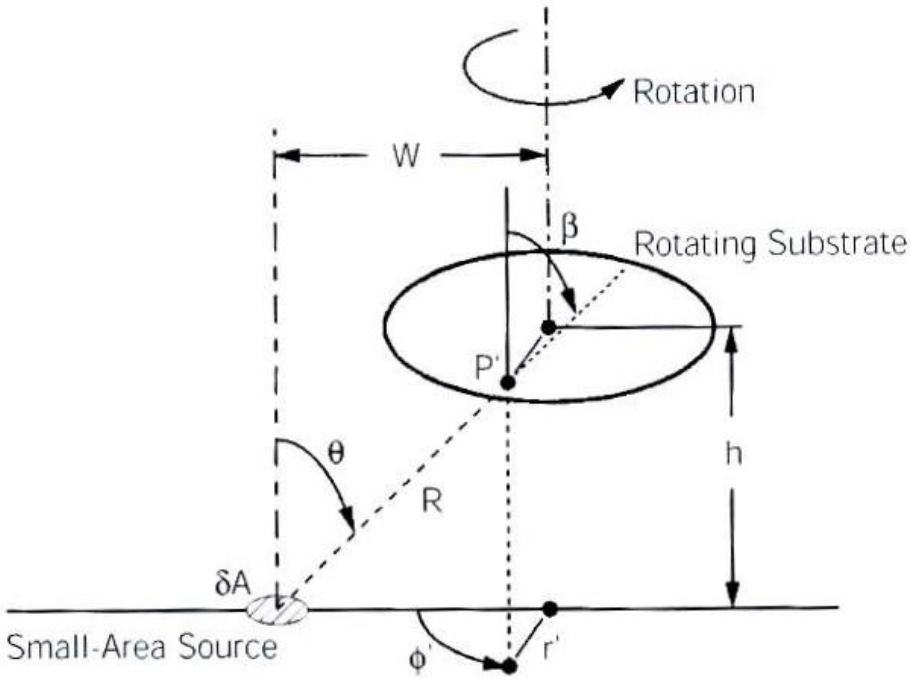

Figure 4.4: Film thickness uniformity with a small source and a flat substrate is drastically improved with off-axis substrate rotation. [Mah00]

Thus, we may calculate the average incident flux at P' during one revolution using (4.10):

$$dj_i = z \cdot \delta A \cdot \frac{h^2}{\pi[h^2+(W-r'cos\varphi')^2+(r\prime sin\varphi\prime)^2]^2} \cdot \frac{d\varphi\prime}{2\pi} \tag{4.12}$$

The average flux (after rearranging the denominator) is:

$$j_{i,av} = \frac{z\,\delta A h^2}{2\pi^2} \int_0^{2\pi} \frac{d\varphi\prime}{[h^2+W^2+r'^2-2r'Wcos\varphi\prime]^2} \tag{4.13}$$

Once integrating, we can express the average flux in function of the normalized radial position $\frac{r\prime}{h}$ and the normalized offset $\frac{W}{h}$:

$$j_{i,av}\left(\frac{r'}{h},\frac{W}{h}\right)=\frac{z\,\delta A}{\pi h^2}\cdot\frac{1+\left(\frac{r'}{h}\right)^2+\left(\frac{W}{h}\right)^2}{[1+\left(\frac{r'}{h}\right)^4+\left(\frac{W}{h}\right)^4+2\left(\frac{r'}{h}\right)^2+2\left(\frac{W}{h}\right)^2-2\left(\frac{r'W}{h^2}\right)^2]^{3/2}} \tag{4.14}$$

Relative film thickness profiles are portrayed in figure (4.5). It is clear that off-axis substrate can drastically improve film thickness uniformity, but there is a trade-off with the deposition rate.

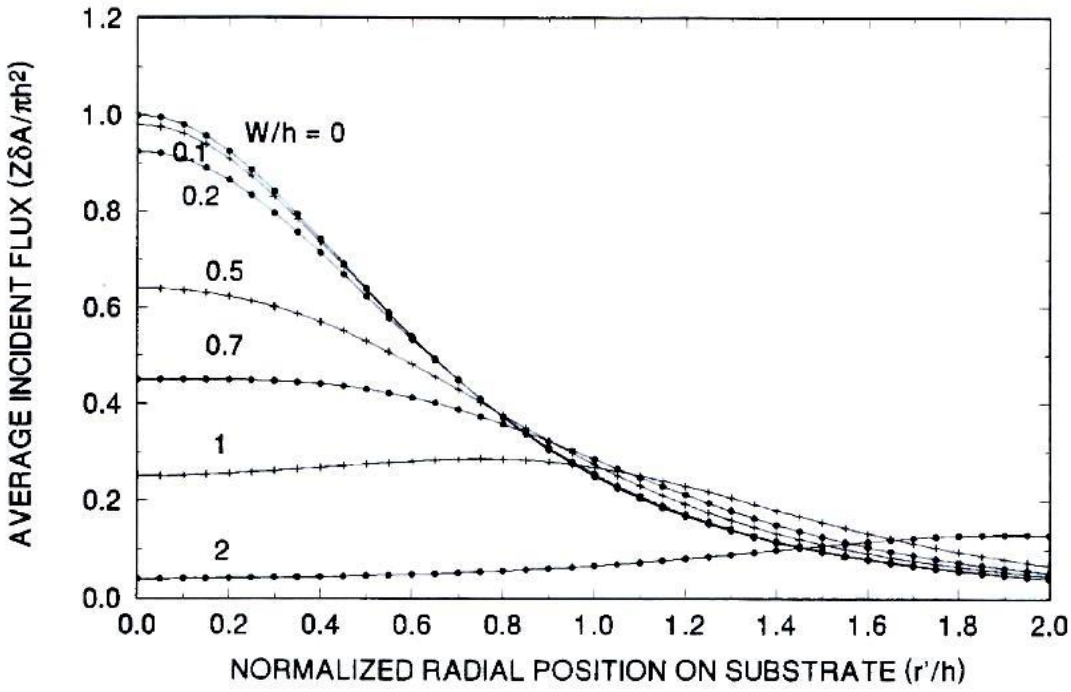

Figure 4.5: Relative film thickness profiles for off-axis substrate rotation.

The offset is W, and the throw distance is h. [Mah00]

The second type of PVD systems employs a design where several vaporization sources are positioned around the vacuum chamber in vertical position while the turntable is in the centre of the chamber. Such design is used for coating the whole surface area of numerous substrates in a single deposition process.

For this system type, [Pan13] simulated a deposition process with different rotation configuration in a specific magnetron sputtering machine (CemeCon CC800/9 SinOx ML), using a computational model previously developed [Pan07].

In this paper, a previously developed computer simulation of coating growth in an industrial deposition system with planetary type of substrate rotation has been utilized. The computer simulation enables calculation of the deposition rate on the surface of a rotating substrate and calculation of individual layer thicknesses that can be visually represented in the form of a multi-layer structure.

The aim of his study is to perform a computer simulation for different sets of parameters and give a detailed analysis of the substrate rotation and target arrangement on the periodicity and uniformity of layered coatings.

In many industrial deposition systems, the turntable rotates around several axes and moves substrates along different targets. The substrate rotation and the target arrangement therefore determine the uniformity of the deposited material. When

different target materials are used coatings can be prepared in a layered structure; in such a case, the rotation and the target arrangement also determine the layer structure of the coating.

Exact periodicity of layered coatings can be calculated from the least common multiple of revolution times around individual axes. Calculations of coating thickness and composition on the perimeter of a round tool show that the uniformity also depends on the deposition time. Configuration with maximally separated targets produces better coating uniformity than configuration with closely positioned targets.

The rotation ensures that the surface gets uniformly exposed by all target sources; in this way, a relatively good coating uniformity can be achieved. This type of PVD systems is mainly utilized for the deposition of protective coatings on substrates with complex geometry where small variations in coating uniformity can be tolerated (e.g. tools, machine components, consumer products, medical instruments).

If the rotation in the PVD system is not designed properly, it may cause substantial non-uniformities. In the top-bottom design where substrates are always in the view of the vaporization sources, variations in the deposition rate are minor. On the contrary, in the deposition systems where the turntable is positioned between the vaporization sources, variations in the deposition rate are large.

In these systems the distance and the angle between the substrate and individual source change significantly due to rotation. When the substrate travels toward a particular vaporization source, the deposition rate increases to the maximum and decreases when the substrate moves away from the source.

If the rotation is highly periodic and substrates return into the same position and orientation for every rotational cycle of the turntable, then a large coating nonuniformity will be produced. The deposition rate variations are especially critical in the reactive deposition mode because they can affect the composition of coatings and, consequently, their properties. In the reactive deposition process the partial pressure of the reactive gas is constant, while the flux of the material on the surface of the substrate changes due to rotation. Since the ratio between the flux of the reactive gas and the vaporized material is not constant, variations in the stoichiometry can occur.

Studies of nanolayered TiAlN/CrN coatings deposited in an industrial magnetron sputtering system with planetary type of rotation revealed that the rotation can produce large differences in the stoichiometry; in some cases, variations were so large that the growth of hexagonal Cr2N phase was initiated within the cubic CrN phase. It was also shown that variations in the deposition flux caused by the rotation have a strong influence on the microstructure and mechanical properties of coatings.

Therefore, rotation should be regarded as one of the deposition parameters since it can significantly influence properties of coatings. Substrate rotation can have an important effect particularly in the case of nanolayered coatings where the thickness of individual layers determines the mechanical properties of coatings. Substrate rotation can cause significant variations in the thickness of individual layers therefore required layer thickness cannot be satisfied for all layers.

The uniformity and the layer structure of nanolayered coatings are also influenced by the target arrangement. Targets can be arranged in different configurations, e.g., targets of the same type can be next or opposite to each other. In nanolayered coatings the sharpness of interfaces plays an important role on the mechanical properties, therefore targets should be arranged in such a way that the intermixing between the materials is minimized.

The accuracy of the calculations was verified by comparing calculated layered structures with the deposited nanolayered coatings.

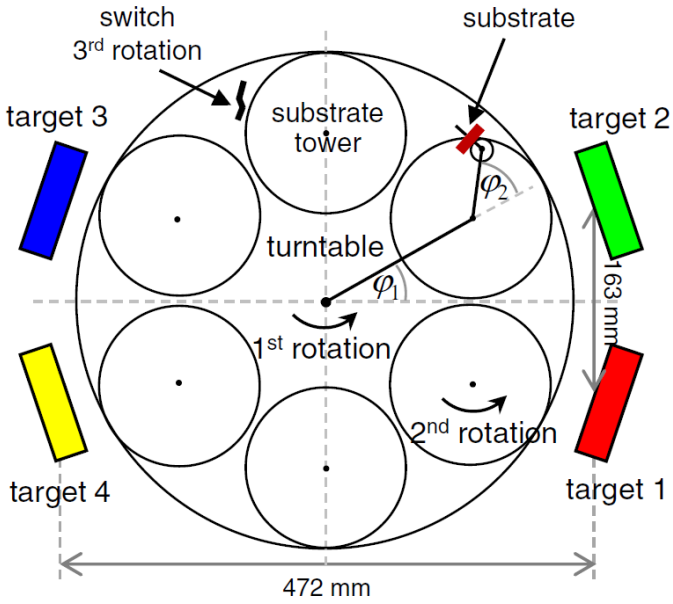

Figure 4.6: Schematic diagram of the CemeCon CC800/9 SinOx ML deposition system.

An example of a simulation is illustrated in Fig. (4.7) showing results for the 3-fold rotation. Normalized deposition rate as a function of time is presented in Fig. (4.7(a)). Calculation was made for arrangement of targets shown in Fig. (4.6) and for two rotational cycles of the turntable. The deposition rate strongly depends on the rotation of the substrate. In each rotational cycle, the material is deposited from all targets but the amount of material from a particular target differs considerably. For example, in the first rotational cycle, the deposition rate from the target 2 is much higher than the deposition rate from other targets. On the other hand, in the second rotational cycle, the deposition rate from the target 2 is low, while the deposition rate from the target 3 is high.
The deposition rate as function of time can be better understood by following the trajectory of the substrate. Fig. (4.7(b)) depicts calculated trajectories for the first and the second rotational cycle. Black arrows indicate the position and the orientation of the substrate in the first rotational cycle and grey ones in the second cycle. In the first rotational cycle, the substrate travels close to the target 2 while facing its direction, therefore, the deposition rate is high. In the second rotational cycle, the substrate also travels close to the target but is facing away from the target, therefore, the deposition rate is low. Note that after the first rotational cycle the substrate does not return in the same initial position and orientation. High deposition rate occurs when the substrate is close to the target and facing its direction, whereas the deposition rate is low when the substrate is far from the target and/ or faces the target under a high angle. In positions where the substrate is not in the direct view of the target the deposition rate is zero.
The thickness of the individual layers and the total thickness of the coating can be calculated by integrating the deposition rate with respect to the time. The calculated layer structure is presented in the horizontal direction above Fig.(4.7(a)).
It can be seen that the individual layers have considerably different thicknesses.
The first layer produced by the target 2 is much thicker than the second layer produced by the same target. In contrast, the first layer produced by the target 3 is much thinner than the second layer produced by the same target, whereas the first and the second layer from the target 4 have approximately equal thickness. Such simulations were performed for different rotation parameters and will be discussed in the following sections.

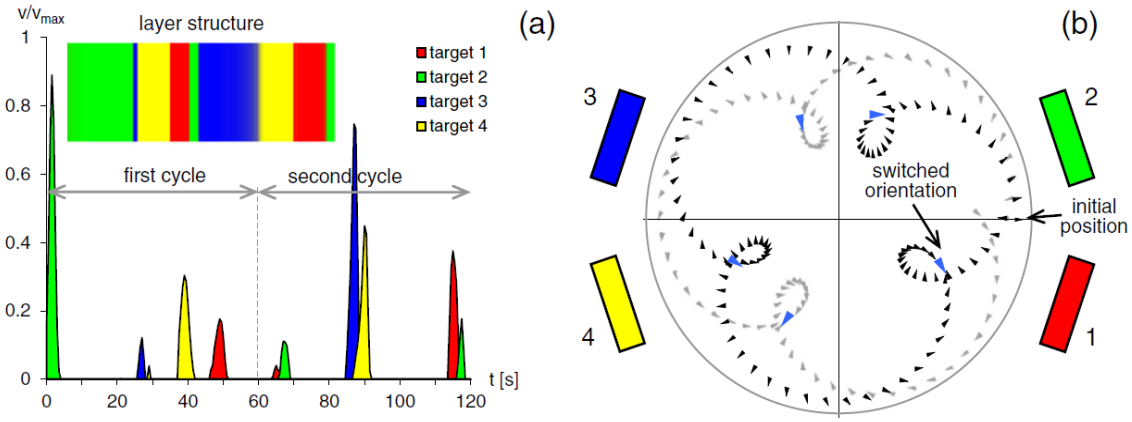

Figure 4.7 (a) Normalized deposition rate in dependence of time and corresponding layered structure for the 3-fold rotation. (b) Trajectory of the substrate for two rotational cycles. Larger (blue) arrows indicate positions where the switch turns the surface (in this case by 165°).

The size of substrate (e.g. tool) determines the type of rotation used in a particular deposition process. The 1-fold rotation, i.e., rotation of a turntable around its axis, is used for coating large tools (e.g. large moulds), while 2- and 3-fold rotations are used for coating smaller tools. Trajectory of the substrates is defined by the revolution times around the individual axes and by the distance between the axes — these are determined by the design of the system and cannot be varied independently. The revolution time around the first and the second axis is defined by the gear ratio between the turntable and the substrate tower, thus, the coupling between these two gears determines the revolution time around the second axis. The rotation around the third axis, in most PVD systems, is realized by a *switch*; normally a steel strip fixed on the rod that turns the substrate for a certain angle for every rotation of the substrate tower around its axis. Switch angle is difficult to control because it depends on the fixture of the switch, as well as on the size and the weight of the tool. The only parameter, which can be adjusted, is the speed of the turntable.

Panjan made a comparison of layer structures produced by different types of rotations. The calculated deposition rate and layer structures for 1-, 2- and 3-fold rotations are shown in Fig. (4.8). Calculations were made for the target arrangement with two types of target material on one side of the deposition chamber, and the other type of material on the other side. The material from the targets 1 and 2 (Fig 4.7) is represented by darker grey colour (i.e. material A), while material from targets 3 and 4 is represented by brighter grey colour (i.e. material B). Layer structures produced by 1-, 2-, and 3-fold rotations differ considerably between each other. In the simple case of 1-fold rotation, a periodic layer structure is formed.

Calculated deposition rate (Fig 4.8(a)) displays that the substrate is periodically exposed to the targets, thus, the individual layers are equally thick. The 1-fold rotation is trivial as the substrate travels on the identical trajectory for each rotation of the turntable. On the other hand, the deposition rates and the layer structures for 2-fold and 3-fold rotations are more complicated and will be discussed later. The thickness of individual layers and the total thickness of the coatings differ between the three types of the rotation.

For the selected calculation parameters (a process with 10 complete rotational cycles), the thickness of individual layers in 1-fold rotation is 90 nm, while in the 2- and 3-fold rotations the thickness varies between 35–40 nm and 7–32 nm, respectively. As a

consequence, the total thicknesses of coatings are: ~1800 nm for 1-fold rotation, ~700 nm for 2-fold rotation and ~400 nm for 3-fold rotation, and the corresponding average deposition rates are ~3 nm/s, ~1.2 nm/s, and ~0.7 nm/s. The rotation around the additional axis considerably lowers the average deposition rate. In this case, the average deposition rate for the 2-fold rotation is ~40% of the deposition rate for the 1-fold rotation, while for the 3-fold rotation the deposition rate is only ~20% of the deposition rate for the 1-fold rotation. In addition to that, the author notices also that these values are the same for different rotational speeds of the turntable and for different initial positions of substrates. The accuracy of the calculations was verified by comparing calculated layered structures with the actual deposited nanolayered coatings [Pan13]

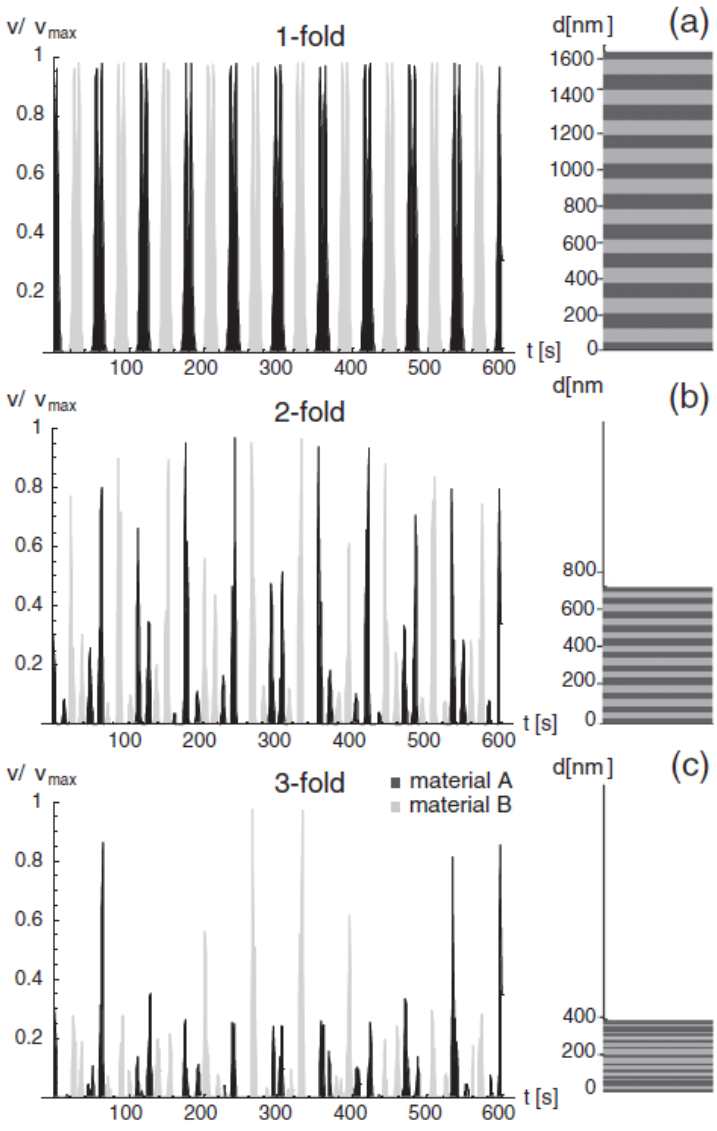

Figure 4.8: Deposition rate and layer structure for (a) 1-, (b) 2-, and (c) 3-fold rotations. Calculations are made for 10 rotational cycles of the turntable with a revolution time of 60 s.

The results obtained by Panjan shows a great influence on deposition rate by the rotation modes of the turntable. Even if the study was limited to a specific model of coating machine, there is a great chance that other coating machines with rotating fixtures follow a similar model.

4.2 Industrial case

Oerlikon Balzers produces in Brugherio plant a high variety of PVD coating, among them BALINIT Alcrona® Pro is the one with the highest and constant demand.
This product is an AlCrN based coating, and it is suitable for improving wear resistance of many tools types: from HSS and carbide gear cutting tools, to mills, drills, punches, small inserts and metal forming moulds.

Figure 4.9: Different cutting tools coated in Balinit ALCRONA PRO

Its wide applicability is the key of its success, indeed at least two batches of Alcrona Pro are daily carried out in the Balzers BAI 1200 coating machine in the tools department.
But due to the heterogenic nature of each batch the coating thickness is not always easy to control and maintain in the desired tolerance interval.

4.2.1 Qualitative Analysis

In accordance with the production and quality management, a process optimization has been set up.
The first step of the process analysis consists in identifying the relevant factors which influences the output of the process (coating thickness).
At this purpose, several brainstorming sessions has been organized, which have involved production, quality, technology and application specialists of the company.
At the end of the brainstorming, seven possible influencing factors are identified.
In the Ishikawa diagram below, every factor is coupled with a score from 1 to 5 which represents the expected grade of influence on the coating thickness.
The seven factors are:

- *Substrate Material*: The base material of the part to be coated.
- *Weight*: The presence of big tools/mould in the batch could influencethe temperature and the electromagnetic field inside the coating chamber.

- *Position*: Vertical position in the chamber (e.g. high, medium, low).
- Rotation: Number of rotation axis of the substrate.
- *Maintenance*: The machine undergoes a scheduled preventive maintenance cycle
- *Target Weight*: Target contains the deposition material, before each batch they are weighed in order to estimate their grade of consumption.
- *Microblasting*: Substrate surfaces are often microblasted in order to polish the surface, uniform roughness and enhance coating adhesion.

The following Ishikawa diagram displays the factors grouped into categories and with an associated expected relevance score:

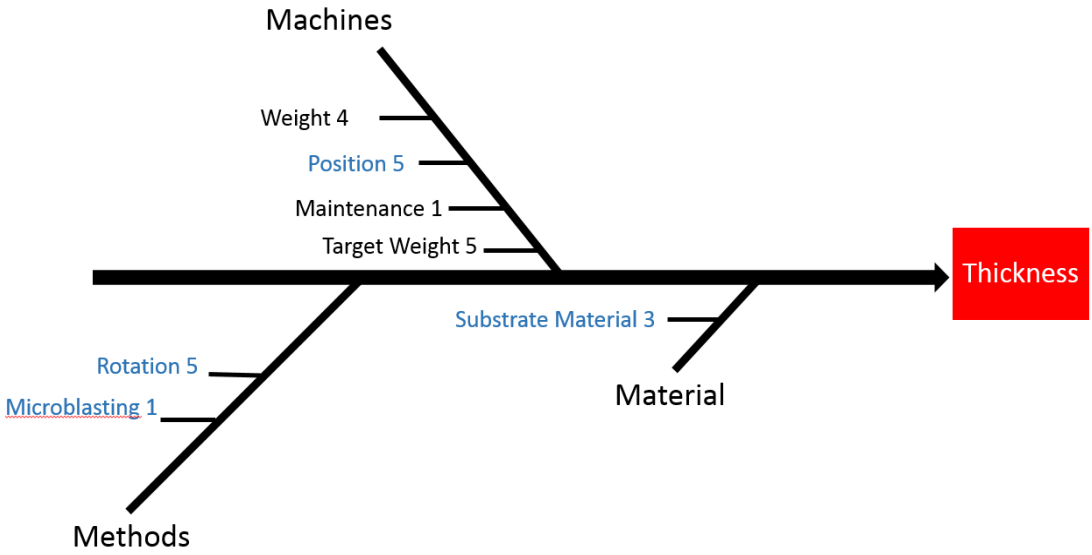

Figure 4.10: Expected significant factors affecting coating thickness, selected at the end of brainstorming sessions. Factors which can be different within a single batch are marked in blue.

Chapter 5

Coating thickness measurement system

Every experimental study requires an appropriate measurement system.
In this chapter will be presented the two methods to evaluate layer thickness; both methods have been analysed with a MSA approach, to evaluate the amount of variability they introduce in the process evaluation.

5.1 Instruments for layer thickness measurement and control

5.1.1 Calotest

Coating thickness plays a major role in the performance of coated tools and machine parts; therefore, many different techniques have been developed for assessing the coating thickness. Among these, the crater-grinding method is easy to perform and applicable to most coated systems.
The method is simple and straightforward, and it is defined in EN ISO 26423:2016.
A crater is ground into the coated part by means of a rotating ball wetted by an abrasive slurry.
The thickness of the coating is derived from the ball and crater dimensional characteristics. Contrast between the different materials constituting the coating and substrate is a prerequisite for the method, to enable detection of the interface between the coating and the surface. Test specimens should be either flat or cylindrical. Flatness can be considered as sufficient if the local specimen radius of curvature r_s, satisfies the relation $r_s > 100 \times r_b$, where r_b is the ball radius.

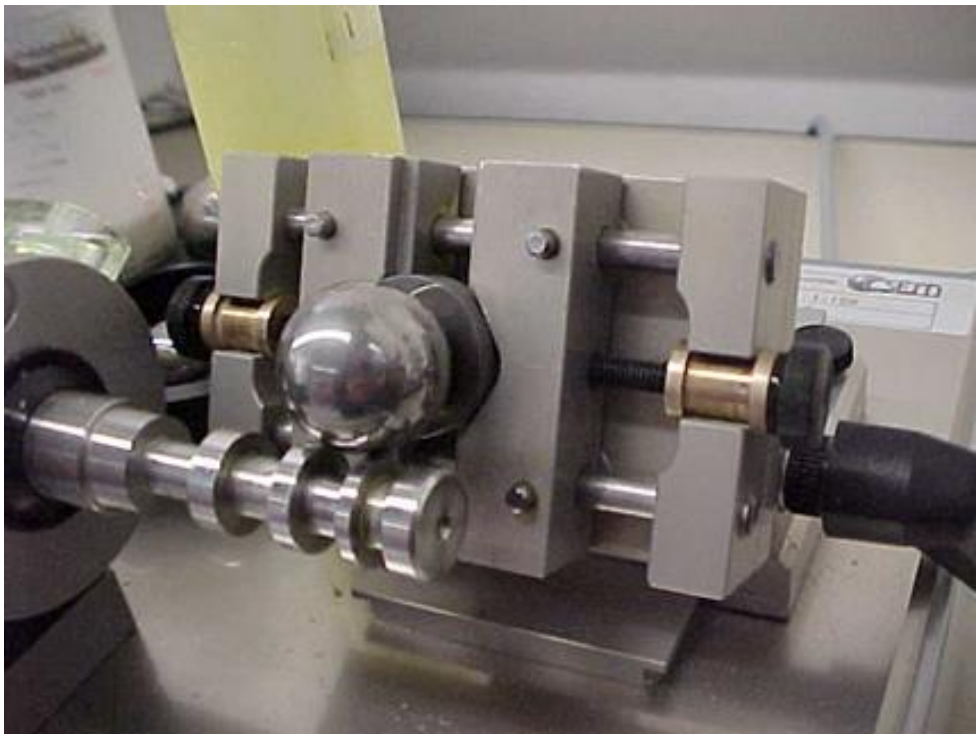

Figure 5.1: Ball grinding of a flat specimen. [Courtesy of Oerlikon Balzers]

The ball wetted by an abrasive slurry is rotated against the surface of the test piece. A spherical wear crater is produced, and the test is finished when the depth of penetration of the spherical crater is greater than the coating thickness. The coating thickness is then derived from the dimensions of the wear scars (full crater and substrate crater diameters) and the ball diameter. Different test rig set-ups maybe used. The ball can be rotated freely on a drive shaft, whereby its mass is used to produce the contact load, or it may be clamped in the drive axis while the specimen is loaded by means of a lever system. Different abrasives (e.g. diamond, alumina, silica) can be used, and commercially available suspensions based on alcohol, oil or water may be applied. The abrasive slurry may be smeared onto the ball surface prior to testing, but more repeatable measurements are achieved when the abrasive slurry is drip-fed into the contact region.
The grain size of the abrasive shall be small enough to avoid roughening of the crater borders. For example, 1 μm diamond paste suspended in ethanol is often used. (Commonly employed in Oerlikon Balzers labs).
To define the geometrical model on which this measurement system is based, it is necessary to introduce the following dimensions, with reference to figure (5.2):

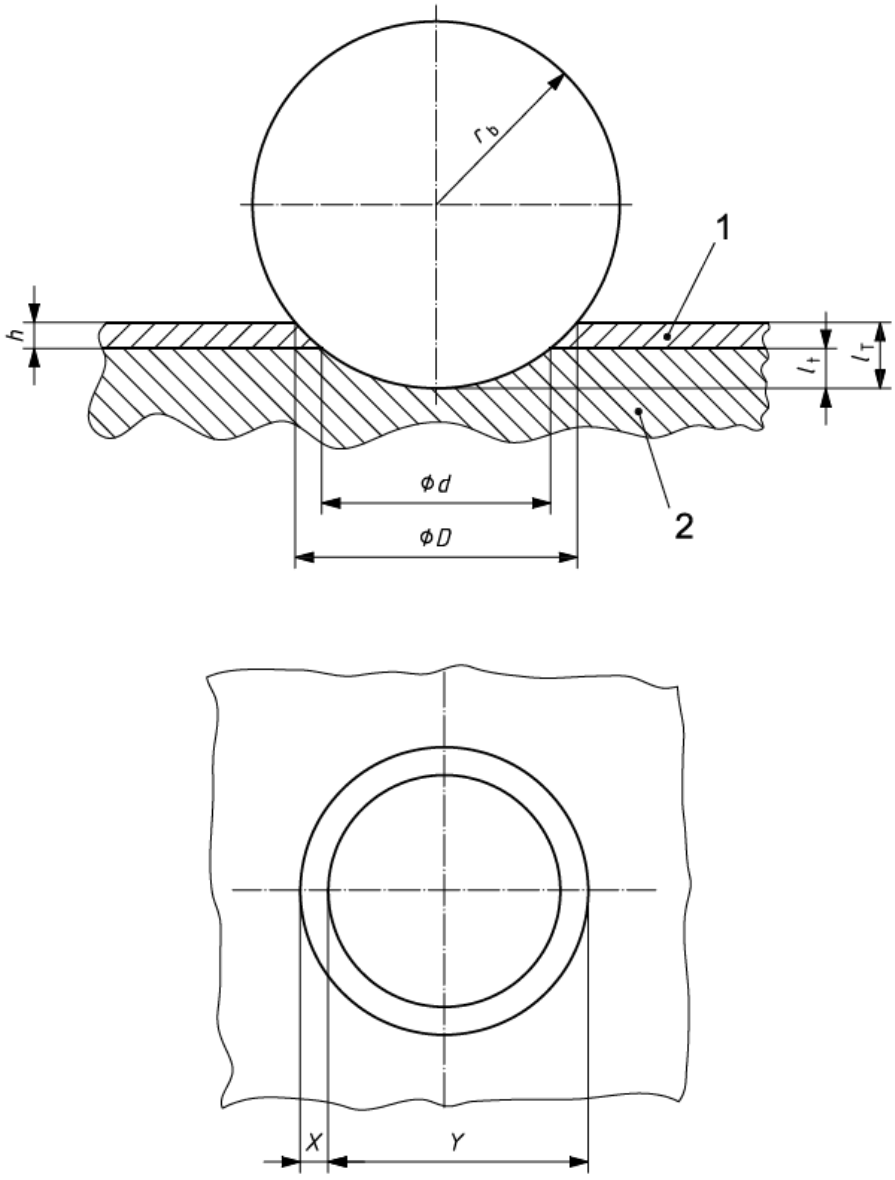

Figure 5.2: Calotest model. (1) Coating layer. (2) Substrate. [EN ISO 26423:2016]

D best estimate of the outer diameter of the crater, at the surface of the coating [µm]

d estimate of the inner diameter of the crater, defined by the bottom of the coating layer [µm]

h thickness of the coating [µm]

m subscript indicating mean value (D_m, $d_m X_m$, Y_m)

r_b radius of the ball [µm]

l_T Total penetration depth of the ball [µm]

l_t penetration depth of the ball in the substrate [µm]

X distance, on a coplanar projection of the two craters, between the periphery of the outer crater and a diametrically equivalent point on the same side of the inner crater [µm]

Y distance, on a coplanar projection of the two craters, between the periphery of the outer crater and a diametrically equivalent point on the opposite side of the inner crater [µm]

Once the crater is grinded, its dimensions must be measured in an appropriate way, using a calibrated measuring device, like a light microscope with digital image processing, connected to a pc.
For flat specimens, measures required are the diameters D, d, or lengths X, Y of the craters, which can be taken in both parallel and perpendicular direction with respect to ball rotation. For cylindrical specimens, measure only the largest dimensions of the craters parallel with the specimen axis. At least 5 measurements shall be carried out, to define the repeatability of the measurement.
Due to surface roughness effects, the boundaries of the layer(s) may not be well defined and the best estimate of the centreline of a boundary shall be used.
If possible, it can be useful etching the crater to increase the contrast between substrate and coating with metallographic etchants (e.g. Nital 2%).
Many steel substrates can be etched. Nital can be used for etching carbon steels, low-alloy steels and grey cast iron., but it is not applicable for stainless steel or carbide materials.

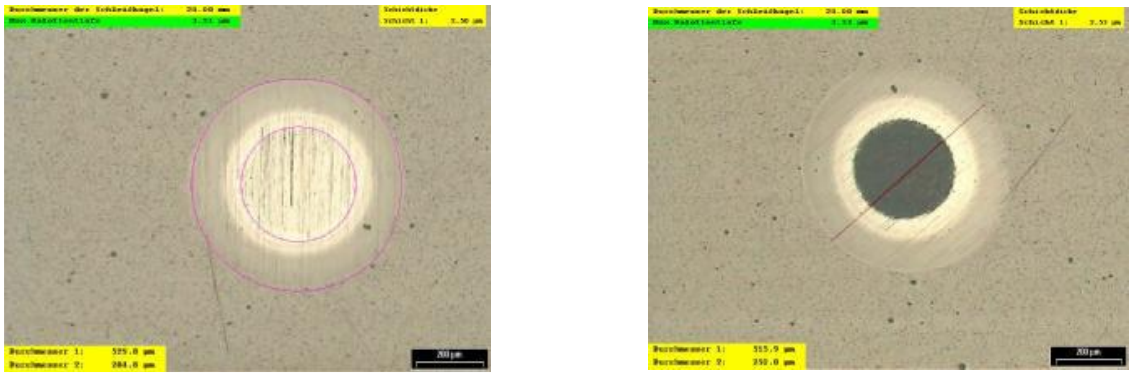

(a) *(b)*

Figure 5.3: Ball grinded crater before (a) and after (b) Nital etching [Courtesy of Oerlikon Balzers]

The total penetration depth of the spherical crater is calculated using:

$$l_T = r_b - \sqrt{r_b^2 - D_m^2/4} \tag{5.1}$$

whereas the penetration depth in the substrate below the coating/substrate interface is given by:

$$l_t = r_b - \sqrt{r_b^2 - d_m^2/4} \tag{5.2}$$

The coating thickness can thus be calculated from:

$$h = l_T - l_t \tag{5.3}$$

or

$$h = \sqrt{r_b^2 - d_m^2/4} - \sqrt{r_b^2 - D_m^2/4} \tag{5.4}$$

For thin coatings, the penetration depth is small in comparison to the radius r_b of the ball. Therefore, the simplified Equation (5.5) can be used to determine the thickness:

$$h = \frac{D^2 - d^2}{8r_b} \tag{5.5}$$

or, by substituting D=X+Y and d=Y-X:

$$h = \frac{X_m Y_m}{8r_b} \tag{5.6}$$

The quality of the grinded crater has an high influence on the measurement accuracy. Many factors can lead to an incorrect crater shape:

- If the calo grinds for a too short time, the transition points between the substrate and the first layer as well as between the single layers are unclear and hard to determine. In most cases is possible to continue the erosion on the same grinding crater.

- If the calo grinds for a too long time, the transition points between the substrate and the different layers are hard to determine. A new crater is to be grinded.
  As an empirical recommendation, for a good measure calo craters require a diameter relationship of 2/1 (Coating/substrate).

- If the grinding speed is too fast, the ball can move during the erosion process, and generate a wrong shaped crater. It can happen also if the edges of the ball slot on the rotary shaft are dirty or worn. A new crater is to be grinded.

- If the surface roughness is high, transition points between layers are very hard to be detected. If there is not the possibility to polish the surface and reduce the roughness, multiple measurement within a calo crater and between several craters can be lead to estimate the variability.

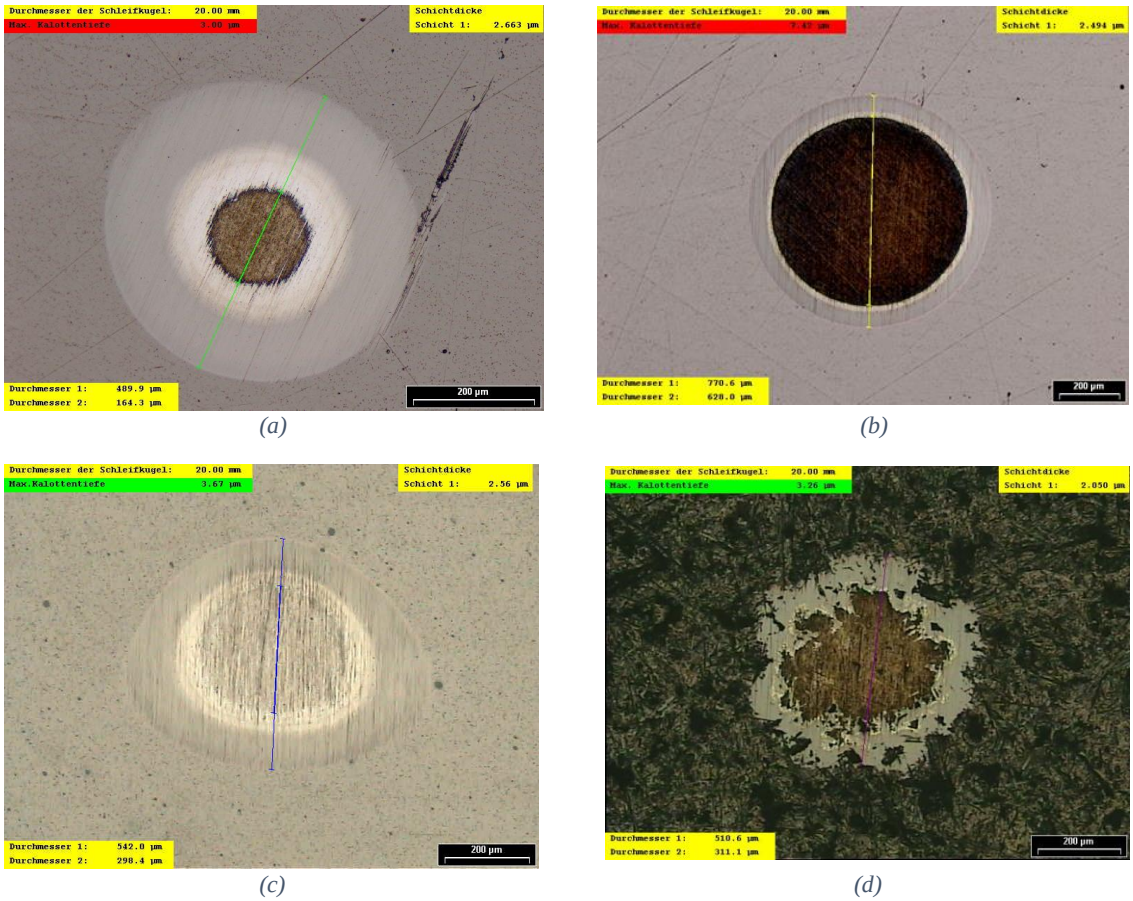

Figure 5.4: Wrong ball craters. (a) Short grinding. (b) Long grinding. (c) Fast grinding. (d) Highly rough surface finishing. [Courtesy of Oerlikon Balzers]

5.1.2 X-Ray Fluorescence Spectrometer (Fisherscope® X-DAL)

In Oerlikon Balzers laboratory it is available another instrument to measure coating thickness, based on X-Ray spectroscopy.
The Helmut Fischer Fischerscope® X-DAL allows a simple and quick determination of the local layer thickness for all metallic coatings.
The photo effect is the mechanism by which X-ray fluorescence is generated. It is the interaction of an electro-magnetic radiation quantum with the energy within an atom.
X-ray fluorescence is generated in the following manner:

- Absorption of the entire energy of an X-ray photon E_{ph} by an electron of an inner shell

  $$E_{ph} > E_I$$

  E_I is the ionization energy.
- Recombination, where the freed-up spot of the inner shell is filled by an electron of an outer shell.
- Emission of an X-ray photon or of an Auger electron.
- The X-ray fluorescence energy is always smaller than the ionization energy ($E_F < E_I$)
- The photo absorption process generates the characteristic fluorescence radiation of the material (the signal). This radiation is designated as “Secondary X-radiation” in Figure 5.5.

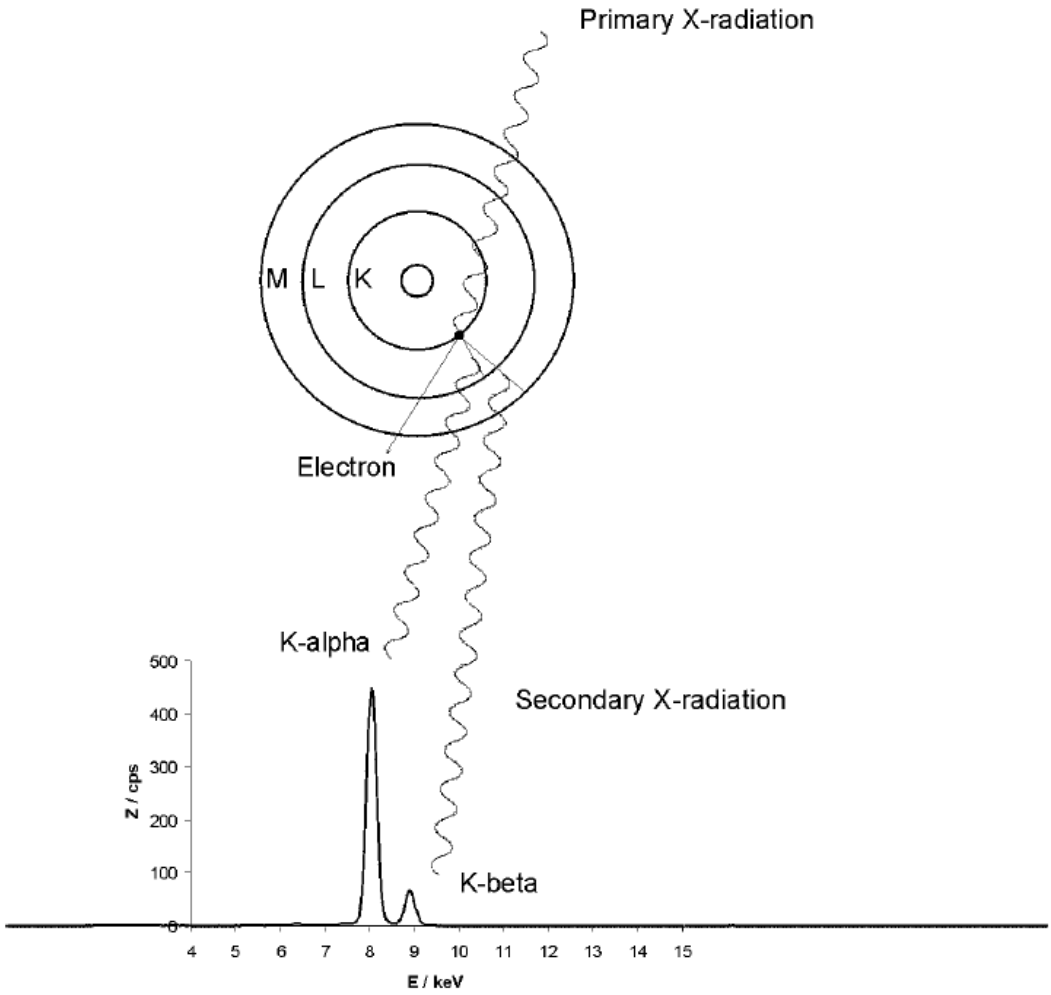

Figure 5.5: Generation of the X-Ray fluorescence radiation. [Helmut Fischer]

The energy dispersive X-ray fluorescence method (ED-XRF) is one of the easiest and most accurate analysis methods for determining the chemical composition of various materials as well as the coating thickness: ED-XRF is a non-destructive and dependable method that requires little or no sample preparation, is suited for solid as well as liquid and powdery samples, covers a broad element range from low atomic numbers up to uranium (Z=92) and that measures concentrations from about 0.1 to 100 percent. The type of detector and the sample chamber (vacuum or no vacuum) determine the lower limit of the element range.
Helmut Fisher, a technological leader and manufacturer of energy dispersive X ray fluorescence spectrometers, has significantly advanced the development of this technology in the past years and decades.
The energy-dispersive X-ray fluorescence method (ED-XRF) is an analysis method that allows for quick and easy coating thickness measurements and element analyses. Essentially all metallic coating systems, solid and liquid samples as well as dust and powder can be measured accurately. The method conforms to DIN 50 987 and ISO 3497.
The technical functional principle is then explained, with reference to figure (5.6):

- (1-3) The heated cathode (2) in the X-ray tube (1) emits electrons.
  Accelerated by a variable high voltage of max. 50 kV, these electrons are bombarded onto the anode (3, usually made of tungsten or molybdenum).

- (4) Basically, the kinetic energy of the electrons is converted into bremsstrahlung. In addition, the characteristic X-ray fluorescence radiation of the anode, e.g. tungsten, is generated and recognizable by the distinct high intensity lines. The primary radiation (4) is a combination of these two types of radiation. Its max. energy is 50 keV.

- (3) Using suitable collimators with different dimensions and shapes (circular, square, slot-shaped), only a portion of the X-radiation emitted by the X-ray tube is employed for the measurement. This allows for the creation of "measurement spot dimensions" as small as about 50 µm x 50 µm. The collimator is made of translucent material for optical imaging of the measurement spot.

- (5-7) A light source (not shown) illuminates the sample. A mirror (5) and lens (6) direct the reflected light to a colour video camera (7). The mirror has a hole in its centre for the primary radiation to pass through.

- (11) The primary radiation excites the coating and substrate materials to emit X-ray fluorescence radiation (11). The reason for this is that a primary radiation quantum knocks an electron from one of the inner electron shells (photo effect). For energy reasons, the resultant void is filled by an electron of an outer shell and energy in the form of X-ray fluorescence radiation (K alpha, K beta - radiation, etc.) is emitted. This energy is characteristic for the respective material.

- (12) The radiation is measured using a radiation detector (12), usually a proportional counter tube filled with xenon gas. The X-ray fluorescence radiation ionizes the xenon atoms. The released electrons accelerate towards the counter wire that is at a high voltage potential and located in the centre. The number of free electrons is proportional to the energy of the X-ray fluorescence radiation.

- (13) The electrons striking the counter wire are converted into electrical pulses using a charge amplifier. The height of the pulses is proportional to the radiation energy.

- (14) The pulses are sorted according to energy and frequency (intensity) of their occurrence. From this, the spectrum (14) of the X-ray fluorescence radiation of the given coating/substrate material combination is obtained. Based on the fundamental parameter method, the WinFTM® software computes the thickness(es) and composition(s) of the coating(s), taking into account all physically relevant processes, and even allows for standard-free measurements.

- (15-16) The measurement data and the video image of the specimen are presented on a color monitor.

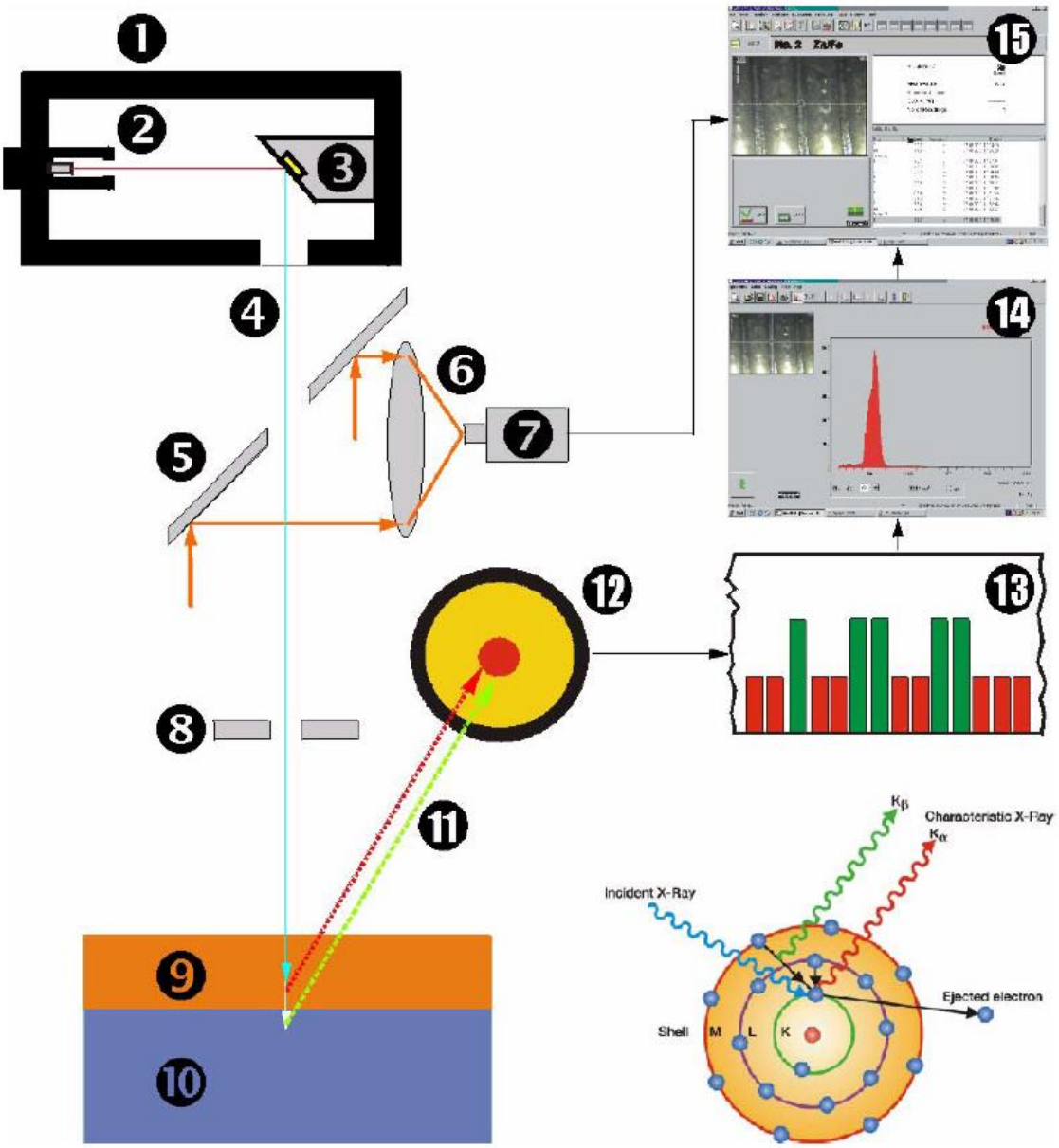

Figure 5.6: Coating specimen and Components of the Fischerscope® X-DAL. (1) X-Ray tube. (2) Cathode. (3) Anode. (4) Primary X-radiation. (5) Mirror. (6) Lens. (7) Video camera. (8) Collimator. (9) Coating Layer. (10) Base material. (11) Secondary X-radiation. (12) Detector. (13) Electrical pulses. (14 Spectrum. (15) WinFTM® main window

5.2 Measurement System Analysis: Gage R&R Study

It is important to remember that measurement system includes not only instruments, but also measurement procedures, operators, and any other factor that affect the measurement of a part.
Measurement systems analysis (MSA) is a method for determining whether a measurement system is acceptable.
This approach is suitable both for measurement of continuous response variables and for attribute response variables. For a continuous response variable, measurement system analysis is used to determine the amount of total variation introduced by the measurement system. For an attribute response variable, MSA is employed to evaluate the consistency and accuracy of appraisers.

MSA is a critical component for any quality improvement process: if the accuracy and precision of a measurement system is proved, any further analysis will be based on reliable data.
In measuring a quantitative continuous variable, the study on the amount of variation introduced in a measurement process by a measurement system is called Gage R&R (Repeatability and Reproducibility).
The amount of variation in an observed process can be split into two main components:

- Part-to-part variation, i.e. the variability in measurements across different parts. Ideally, differences between parts (Part-to-Part) should explain most of the variability.
- Measurement system variation, it is all variation associated with a measurement process. Potential sources of variation include gages, standards, procedures, software, environmental components, and so on.

Like any other process, a measurement system is subject to both common-cause and to special-cause variation.
To control the measurement system variation, it is mainly important to identify the sources of the variation, which can be either eliminated or reduced the various causes.
Measurement system variation is composed by two sources:

- Repeatability: it is the variation due to the measurement device, that is observed when the same operator measures the same part many times, using the same gage, under the same conditions.
- Reproducibility: it is the variation due to the measurement system, that is observed when different operators measure the same part many times, using the same gage, under the same conditions.
  In addition, reproducibility can be split into two sources:

  - Operator: The variability in measurements due to different operators.
  - Operator-by-Part: The variability in measurements due to different operator/part combinations after considering part and operator separately.

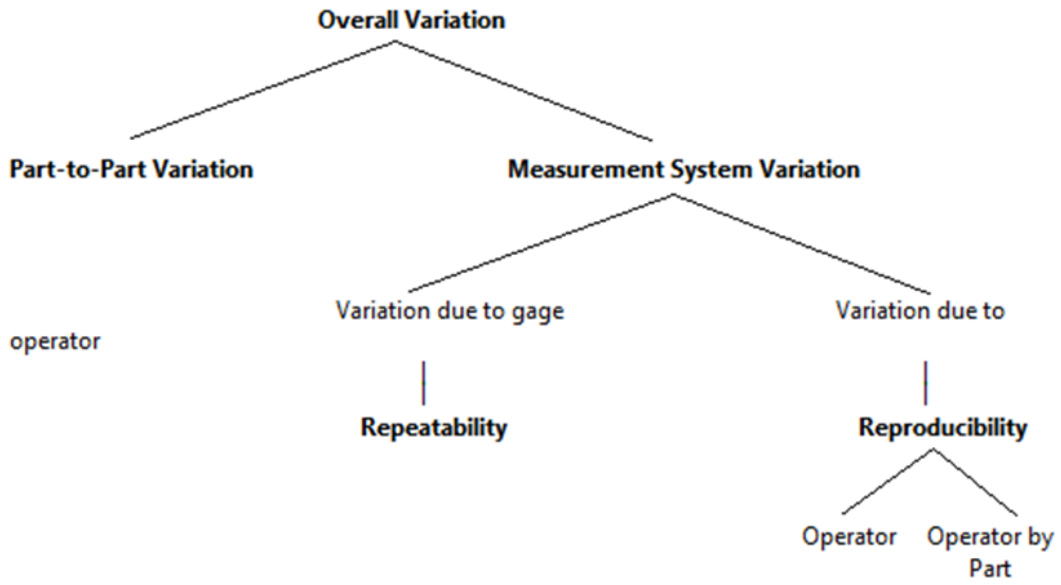

Figure 5.7: Components of variation in an observed process [Minitab Inc.]

The Automotive Industry Action Group (AIAG) has developed criteria to evaluate the acceptability of a measurement system.
The AIAG is a global organization that provides an open forum for companies from around the world to develop and share information that contributes to the automotive industry.
A lot of companies in many industries use AIAG publications for guidelines and methods for process improvement.
According to [AIAG10], if measurement system variation is less than 10% of process variation, then it is acceptable.
To evaluate process variation, it is possible to compare the Total Gage R&R contribution in terms of standard deviation with respect to the overall value: the thresholds suggested by AIAG are below reported:

Percentage of process variation	**Acceptability**
Less than 10%	The measurement system is acceptable.
Between 10% and 30%	The measurement system is acceptable depending on the application, the cost of the measurement device, cost of repair, or other factors.
Greater than 30%	The measurement system is not acceptable and should be improved.

The same approach can be adopted using variance components instead of standard deviation. In this case the following acceptability limits should be adopted:

Percentage of variance components	**Acceptability**
Less than 1%	The measurement system is acceptable.
Between 1% and 9%	The measurement system is acceptable depending on the application, the cost of the measurement device, cost of repair, or other factors.
Greater than 9%	The measurement system is not acceptable and should be improved.

Although the number of appraisers, trials and parts may be varied, it is also AIAG has defined a detailed procedure for this study:
1) Obtain a sample of $n > 10$ parts, that represent the actual or expected range of process variation.
2) Refer to the appraisers as A, B, C, etc. and number the parts as 1 through *n* so that the numbers are not visible to the appraisers.
3) Calibrate the gage if this is part of the normal measurement system procedures. Let appraiser A measure *n* parts in a *random* order.
4) Let appraisers B and C measure the same *n* parts without seeing each other's readings;

5) Repeat the cycle using a different random order of measurement.
6) Steps 4 and 5 may be changed to the following when large part size or simultaneous unavailability of parts makes it necessary:

- Let appraiser A measure the first part and record the reading in row 1. Let appraiser B measure the first part and record the reading in row 6. Let appraiser C measure the first part and record the reading in row 11.
- Let appraiser A repeat reading on the first part and record the reading in row 2, appraiser B record the repeat reading in row 7, and appraiser C record the repeat reading in row 12. Repeat this cycle and enter the results in rows 3, 8, and 13, if three trials are to be used.

7) An alternative method may be used if the appraisers are on different shifts. Let appraiser A measure all 10 parts and enter the reading in row 1. Then have appraiser A repeat the reading in a different order and enter the results in rows 2 and 3. Do the same with appraisers B and C.

5.2.1 Gauge R&R – Calotest

The first R & R evaluation has been performed on Calotest.
The design of the experiment is composed by 4 appraisers (operators), which have to measure 15 coated samples (parts), each of them for 5 runs.
Number of operators, parts and runs is higher with respect to the minimum configuration (3 operators, 10 parts, 2 runs), reported in [AIAG10].
Data have been collected in a full randomized order, and then processed through an ANOVA (Analysis of variance) using Minitab® software.
The 15 parts have been selected randomly from the collection of coated samples of the same coating type. All samples are grinded and polished disks, ⌀22 x 5 mm.
The following graph shows the boxplots of the coating thickness measured on the 15 samples by the 4 appraisers. Measures of each pats have a comparable variability, but the random sampling seems to have selected a very short thickness range, shorter than the expected one. Many parts have a thickness point estimate within the interval (3.0 – 3.5 µ). This amount of parts with a similar coating thickness value, could lead to an underestimation of the part-to-part variability of the process.

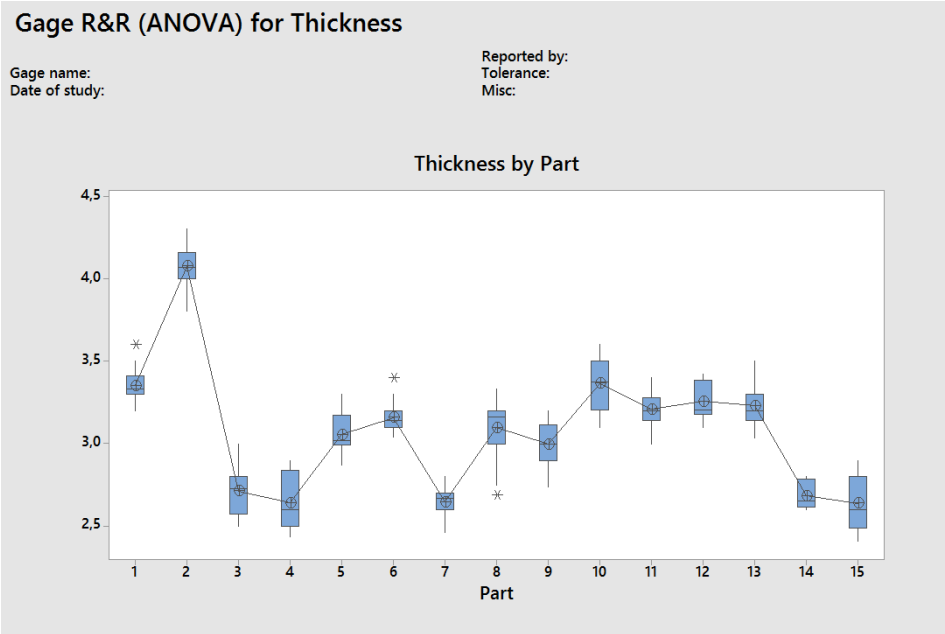

Figure 5.8

Part * Operator interaction seems to be not significant:

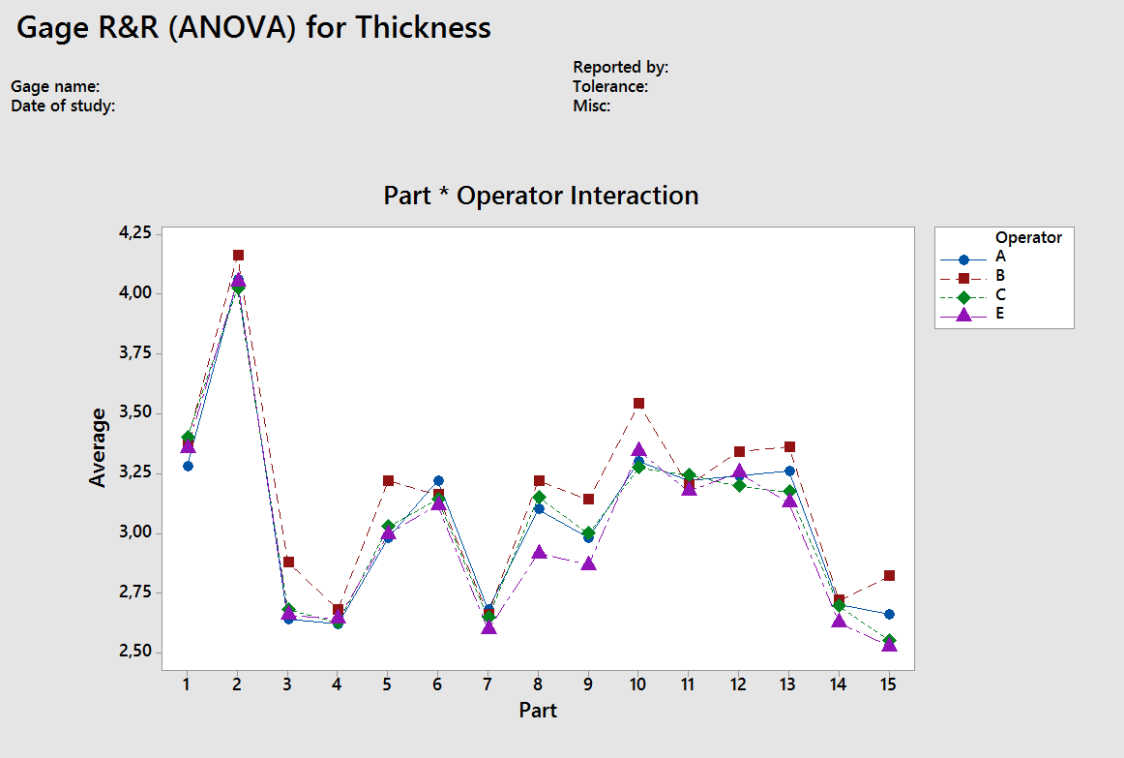

Figure 5.9

The Run Chart shows all the measures divided into parts and operators. This graph can be useful to state whether an appraiser has measured one or more parts not consistently. In this specific case, there are no apparent inconsistencies.

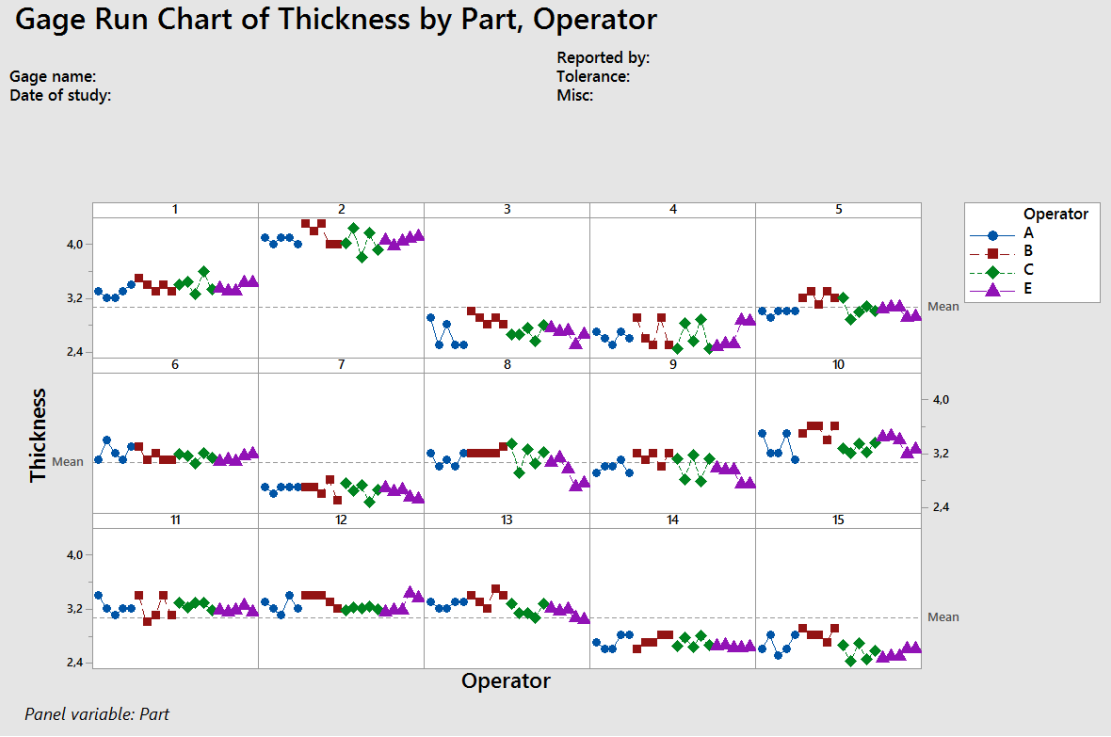

Figure 5.10

Before showing the ANOVA analysis, it can be useful to show the results obtained with Xbar-R method for gauge R&R .
If the Xbar chart (i.e. the graph of part point estimates for each operator) looks “out of control”, and the R chart of ranges appears in control, then the measurement system introduces less variability with respect to the difference between parts.

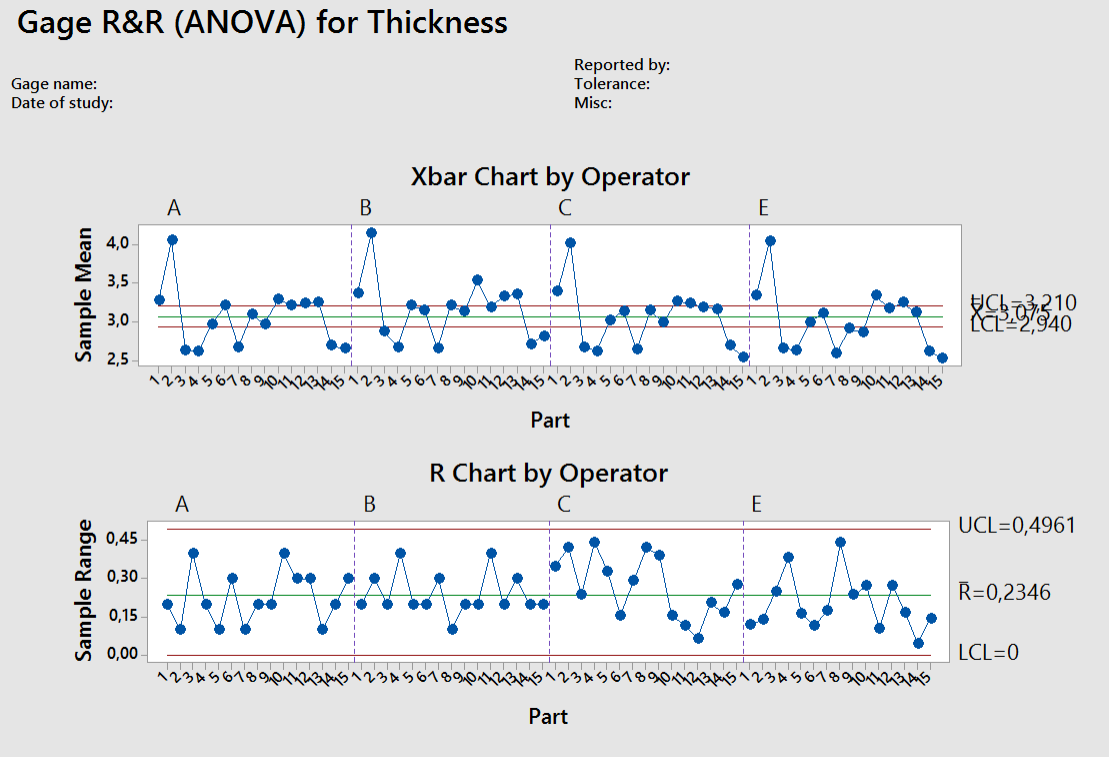

Figure 5.11 XBar and R Charts

The ANOVA table is reported below. Factors “parts”, ”operators” seem to be significant. Also, their interaction appears slightly significant.

Two-Way ANOVA Table With Interaction

Source	DF	SS	MS	F	P
Part	14	41,8582	2,98987	157,698	0,000
Operator	3	0,9044	0,30146	15,900	0,000
Part * Operator	42	0,7963	0,01896	1,469	0,040
Repeatability	240	3,0966	0,01290		
Total	299	46,6554			

α to remove interaction term = 0,05

Figure 5.12

It is important to check the ipothesis of the analisys of variance.
The normality hypothesis cannot be refused:

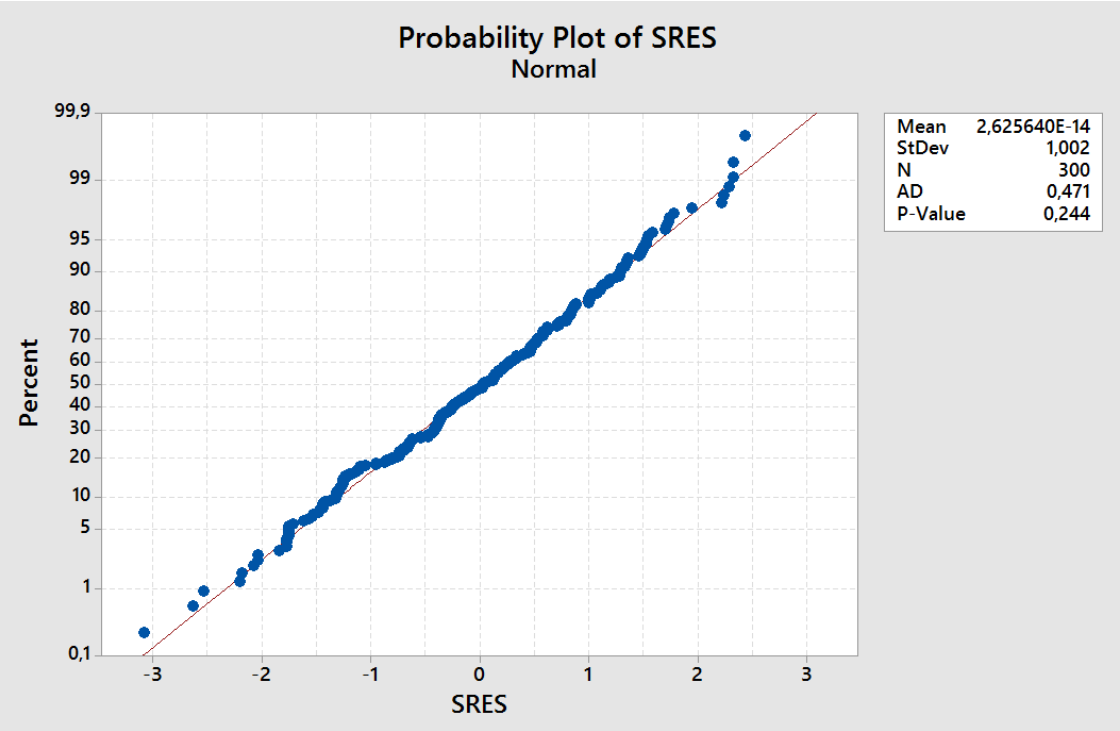

Figure 5.13

Equality of variances cannot be refused:

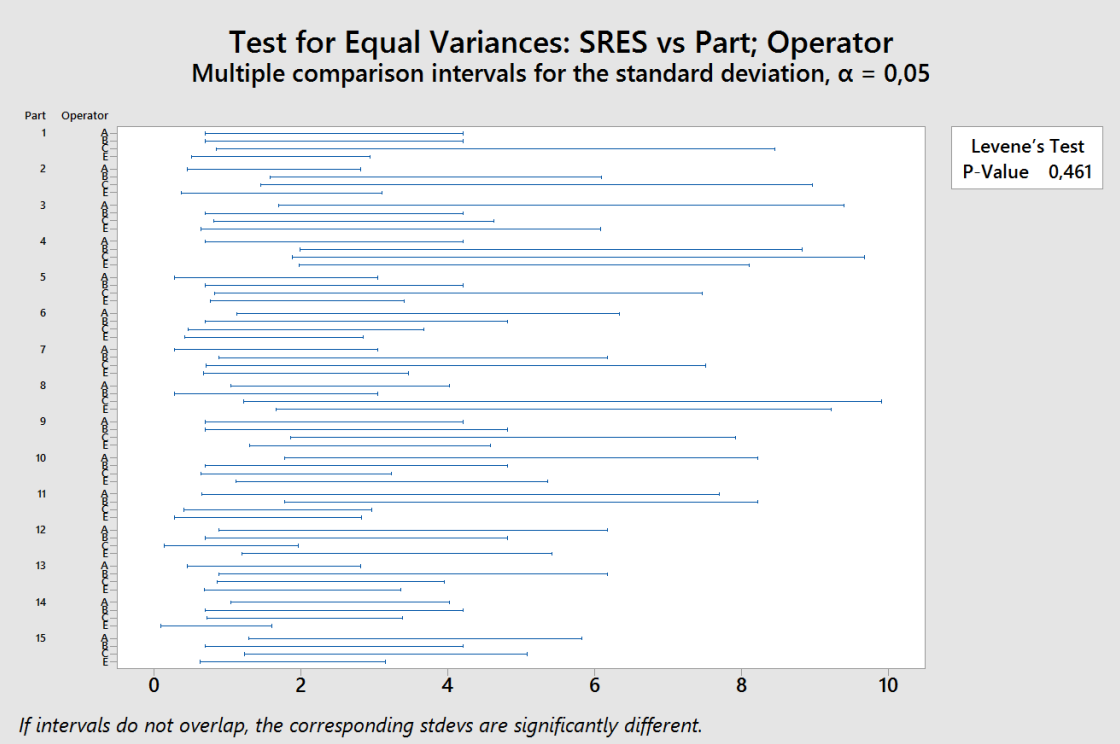

Figure 5.14

Only 1 out of 300 residuals does not belong to (-3,+3) interval, but there are no evident outliers. No obvious residuals distribution appears.

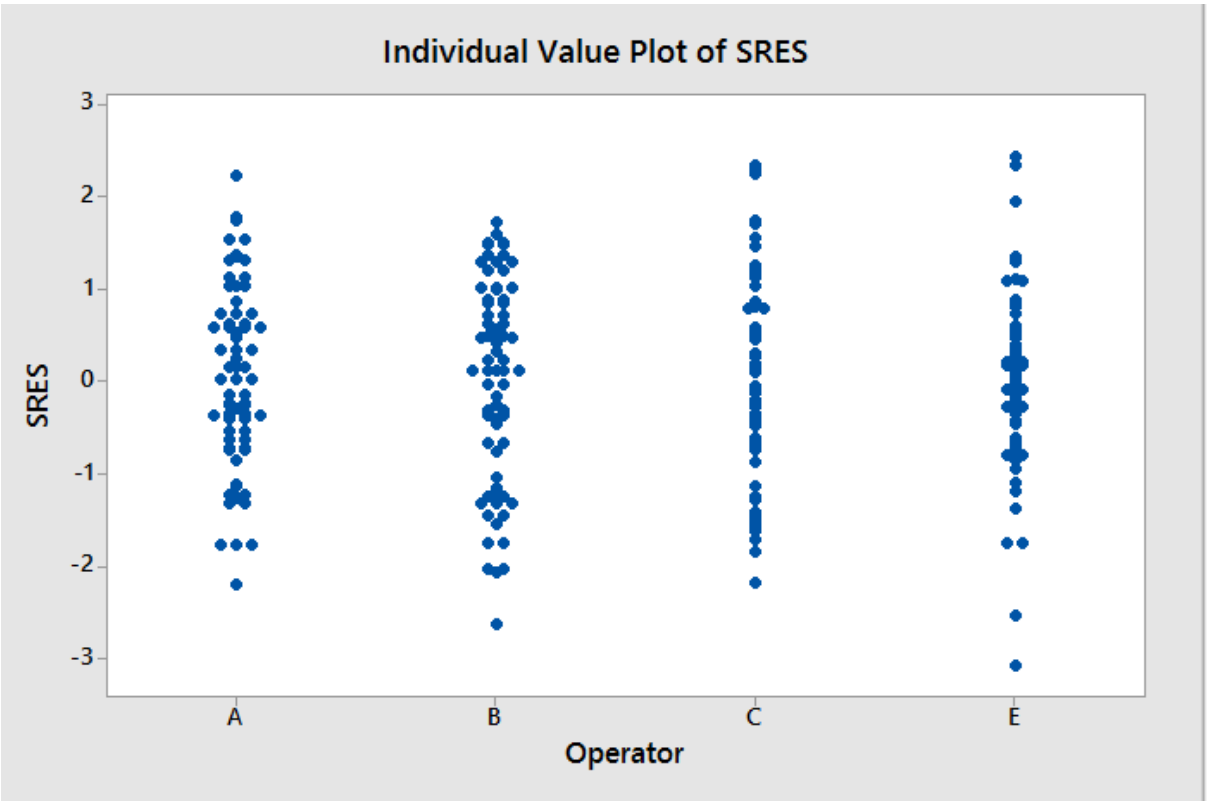

Figure 5.15

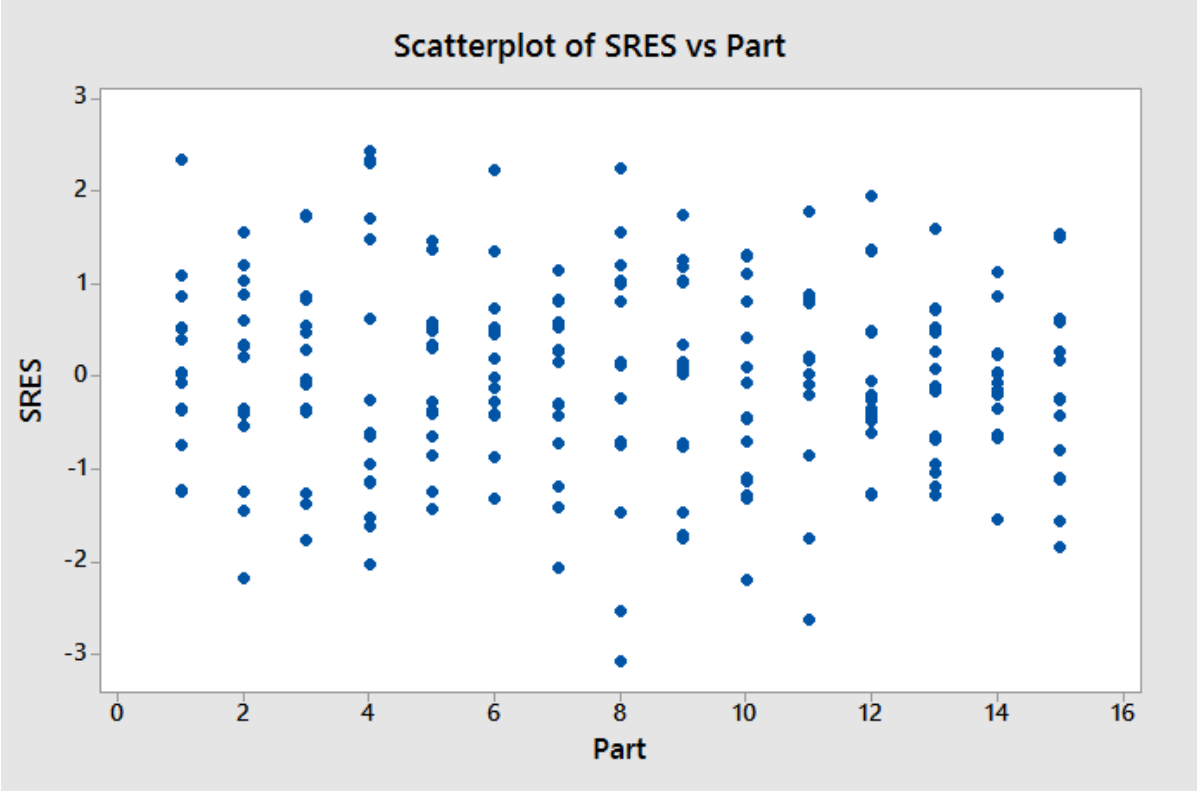

Figure 5.16

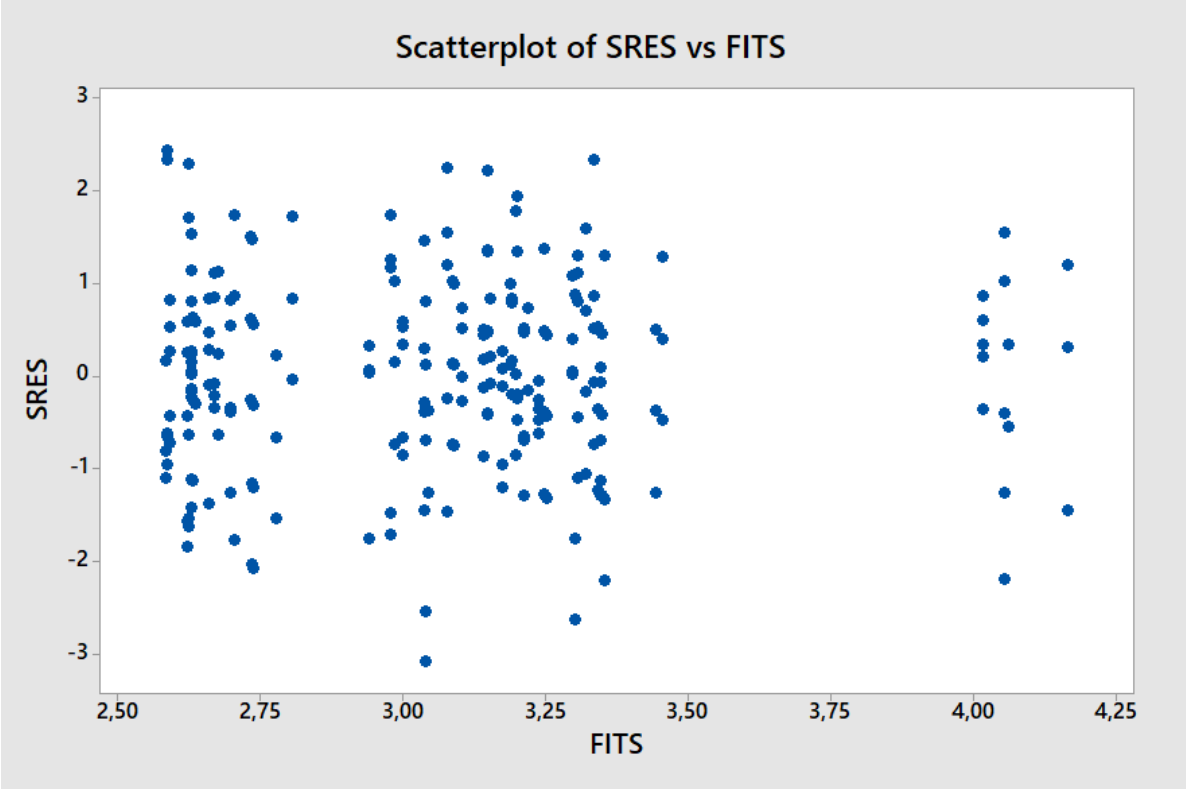

Figure 5.17

Autocorrelation analysis does not show any periodicity.

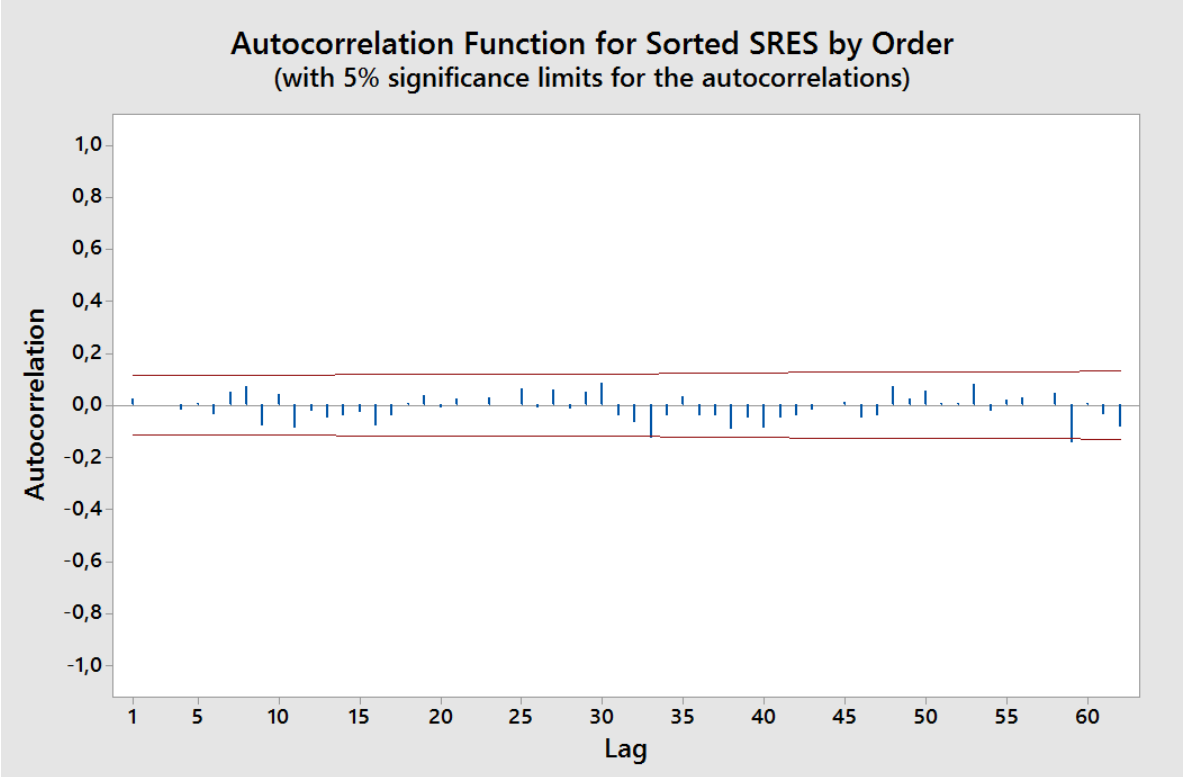

Figure 5.18

The following graph shows the amount of variability introduced by the measurement system both in terms of standard deviation and variance.

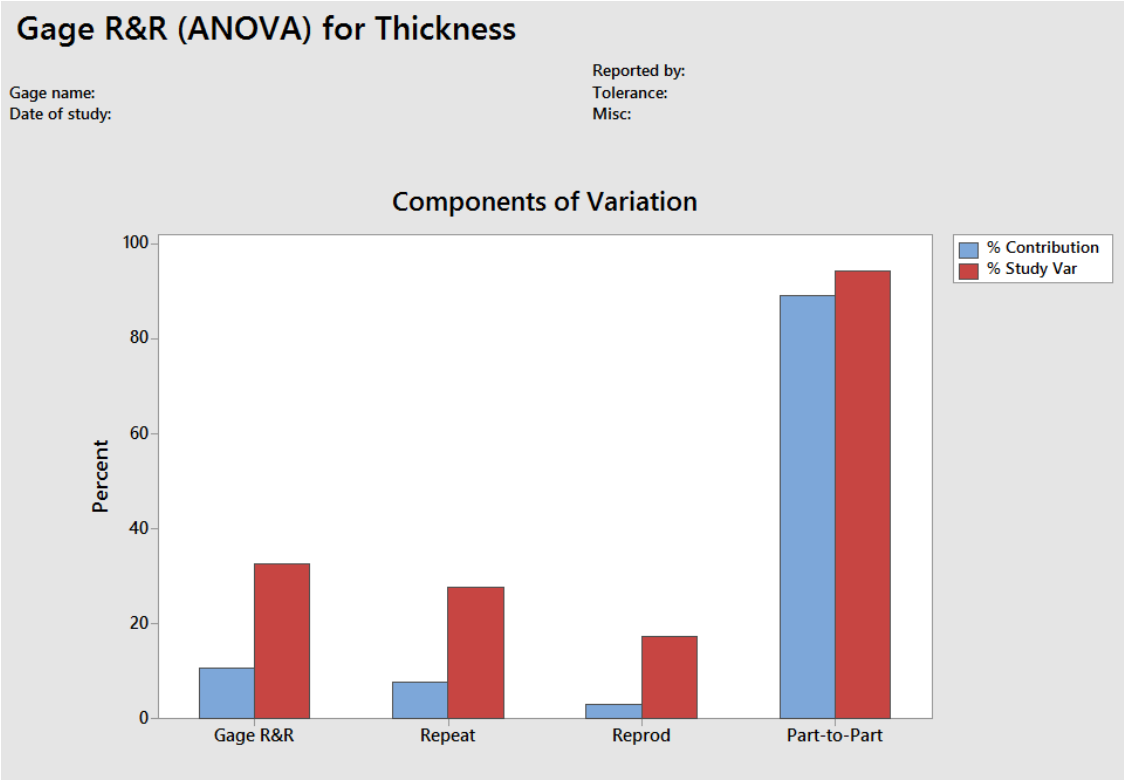

Figure 5.19

Gage R&R

Source	VarComp	%Contribution (of VarComp)
Total Gage R&R	0,017881	10,74
Repeatability	0,012902	7,75
Reproducibility	0,004978	2,99
Operator	0,003767	2,26
Operator*Part	0,001211	0,73
Part-To-Part	0,148545	89,26
Total Variation	0,166426	100,00

Source	StdDev (SD)	Study Var (6 × SD)	%Study Var (%SV)
Total Gage R&R	0,133718	0,80231	32,78
Repeatability	0,113589	0,68153	27,84
Reproducibility	0,070556	0,42333	17,30
Operator	0,061373	0,36824	15,04
Operator*Part	0,034805	0,20883	8,53
Part-To-Part	0,385416	2,31250	94,48
Total Variation	0,407953	2,44772	100,00

Number of Distinct Categories = 4

Figure 5.20

The point estimate of the total Gage R&R variance percentage contribution is equal to 10.74 %, while the standard deviation component is the 32,78 %

Gage R&R

Source	VarComp	95% CI	%Contribution (of VarComp)	95% CI
Total Gage R&R	0,017881	(0,015; 0,070)	10,74	(4,49; 33,37)
Repeatability	0,012902	(0,011; 0,016)	7,75	(3,23; 13,75)
Reproducibility	0,004978	(0,002; 0,057)	2,99	(0,80; 26,39)
Operator	0,003767	(0,001; 0,056)	2,26	(0,50; 25,72)
Operator*Part	0,001211	(0,000; 0,004)	0,73	(0,00; 2,49)
Part-To-Part	0,148545	(0,079; 0,371)	89,26	(66,63; 95,51)
Total Variation	0,166426	(0,097; 0,395)	100,00	

Source	StdDev (SD)	95% CI	Study Var (6 × SD)	95% CI	%Study Var (%SV)
Total Gage R&R	0,133718	(0,120; 0,264)	0,80231	(0,723; 1,586)	32,78
Repeatability	0,113589	(0,104; 0,125)	0,68153	(0,626; 0,748)	27,84
Reproducibility	0,070556	(0,042; 0,238)	0,42333	(0,250; 1,431)	17,30
Operator	0,061373	(0,032; 0,236)	0,36824	(0,192; 1,415)	15,04
Operator*Part	0,034805	(0,000; 0,060)	0,20883	(0,000; 0,358)	8,53
Part-To-Part	0,385416	(0,281; 0,609)	2,31250	(1,688; 3,654)	94,48
Total Variation	0,407953	(0,311; 0,628)	2,44772	(1,869; 3,770)	100,00

Source	95% CI
Total Gage R&R	(21,19; 57,77)
Repeatability	(17,99; 37,08)
Reproducibility	(8,94; 51,37)
Operator	(7,04; 50,72)
Operator*Part	(0,00; 15,78)
Part-To-Part	(81,63; 97,73)
Total Variation	

Number of Distinct Categories = 4

Figure 5.21

95% confidence interval can be more useful than the point estimate in understanding the amount of variability indroduced by this system.
The gage R&R percentage contribution confidence interval is (4,49 % , 33,37%).
[AIAG2010] defines as optimal a variance ratio equal to 1%, but values up to 9% can be assumed
The point estimate is slightly over these second treshold, as well as the higher c.i. limit, which is three times greater than the limit.
On the contrary, the lower interval bound lays between the 1% and the 9% limit.
As already said, the random samplying could have lead to an underestimation of the process variability, and a consequent negative performance of the measurement system in this test.
A possible improvement of this gage study, excluding a repetition with new samples, could derive from reducing the width of the 95% confidence interval
In [Bur05], Burdick et al. studied the expression of Gauge R&R confidence intervals, and their dependence from number of part, operators and repetitions employed.
The most relevant confidence interval in a gauge R&R study is the one associated to the ratio $\frac{\gamma_M}{\gamma_M+\gamma_P}$, where γ_M is the measurement system variance and γ_P is the process vaiance, so $\gamma_M + \gamma_P$ is the total variance. It is also defined $1 - \frac{\gamma_M}{\gamma_M+\gamma_P} = \frac{\gamma_P}{\gamma_M+\gamma_P} = \rho$, as the ratio between the process variance and the overall variance.
If $\gamma_R = \frac{\gamma_P}{\gamma_M}$, since $\rho = \frac{\gamma_P}{\gamma_M+\gamma_P} = \frac{\gamma_R}{1+\gamma_R}$, then the confidence interval of ρ can be derived from γ_R confidence interval through a sequence of simple operations:

of these parameters. To demonstrate, suppose $[L, U]$ is an exact 95% two-sided confidence interval for γ_R. This means

$$\Pr[L \le \gamma_R \le U] = 0.95.$$

Thus

$$\begin{aligned}\Pr[L \le \gamma_R \le U] &= \Pr\left[\frac{1}{L} \ge \frac{1}{\gamma_R} \ge \frac{1}{U}\right] \\ &= \Pr\left[\frac{1}{L}+1 \ge \frac{1}{\gamma_R}+1 \ge \frac{1}{U}+1\right] \\ &= \Pr\left[\frac{1+L}{L} \ge \frac{1+\gamma_R}{\gamma_R} \ge \frac{1+U}{U}\right] \\ &= \Pr\left[\frac{L}{1+L} \le \frac{\gamma_R}{1+\gamma_R} \le \frac{U}{1+U}\right] \\ &= 0.95.\end{aligned}$$

So from the definition of ρ shown in Equation (1.4), the 95% confidence interval for ρ is

$$\left[\frac{L}{1+L}, \quad \frac{U}{1+U}\right].$$

Figure 5.22 Extract from [Bur05]

Therefore, for $1-\rho = \frac{\gamma_M}{\gamma_M+\gamma_P}$ confidence inteval limits will end up in $\left[\frac{1}{1+U}, \frac{1}{1+L}\right]$.

Two methods are then proposed for calculating intervals: a Modified Large Samples (MLS) method to calculate approximate ranges in a closed form, and a method called GCI, a "computer intensive" approach, which calculates intervals by considering percentiles of a generated pivot quantity (GPQ).
Both methods, according to the authors, often offer very similar results.
Considering the MLS method for a model of two factors plus interaction, formulas for the lower and upper bound of 100(1-α) % confidence interval for γ_R are defined:

$$L = \frac{p(1-G_1)(S_P^2 - F_1 S_{PO}^2)}{po(r-1)S_E^2 + o(1-G_1)F_3 S_O^2 + o(p-1)S_{PO}^2} \tag{5.1}$$

$$U = \frac{p(1-H_1)(S_P^2 - F_2 S_{PO}^2)}{po(r-1)S_E^2 + o(1-H_1)F_4 S_O^2 + o(p-1)S_{PO}^2} \tag{5.2}$$

The other constants present in these formulas are defined in the following table:

Constant	Definition	Value
G_1	$1 - F_{\alpha/2:\infty,p-1}$	0.4217
G_2	$1 - F_{\alpha/2:\infty,o-1}$	0.6104
G_3	$1 - F_{\alpha/2:\infty,(p-1)(o-1)}$	0.2330
G_4	$1 - F_{\alpha/2:\infty,po(r-1)}$	0.2116
H_1	$F_{1-\alpha/2:\infty,p-1} - 1$	1.133
H_2	$F_{1-\alpha/2:\infty,o-1} - 1$	5.015
H_3	$F_{1-\alpha/2:\infty,(p-1)(o-1)} - 1$	0.3586
H_4	$F_{1-\alpha/2:\infty,po(r-1)} - 1$	0.3104
F_1	$F_{1-\alpha/2:p-1,(p-1)(o-1)}$	1.876
F_2	$F_{\alpha/2:p-1,(p-1)(o-1)}$	0.4503
F_3	$F_{1-\alpha/2:p-1,o-1}$	6.344
F_4	$F_{\alpha/2:p-1,o-1}$	0.3001
G_{13}	$\frac{(F_1-1)^2 - G_1^2F_1^2 - H_3^2}{F_1}$	0.006771
H_{13}	$\frac{(1-F_2)^2 - H_1^2F_2^2 - G_3^2}{F_2}$	−0.0276

Figure 5.23: Constants used in confidence intervals for the two factors model Gage R&R. Values in the last column are for a reference design of α=0.05, p=20, o=6, and r=2 [Bur05]

Source of variation	Degrees of freedom	Mean square	Expected mean square
Parts (P)	$p-1$	S_P^2	$\theta_P = \sigma_E^2 + r\sigma_{PO}^2 + or\sigma_P^2$
Operators (O)	$o-1$	S_O^2	$\theta_O = \sigma_E^2 + r\sigma_{PO}^2 + pr\sigma_O^2$
P×O	$(p-1)(o-1)$	S_{PO}^2	$\theta_{PO} = \sigma_E^2 + r\sigma_{PO}^2$
Replicates	$po(r-1)$	S_E^2	$\theta_E = \sigma_E^2$

Figure 5.24 Anova table

Statistic	Definition
S_P^2	$\frac{or\Sigma_i(\overline{Y}_{i**}-\overline{Y}_{***})^2}{p-1}$
S_O^2	$\frac{pr\Sigma_j(\overline{Y}_{*j*}-\overline{Y}_{***})^2}{o-1}$
S_{PO}^2	$\frac{r\Sigma_i\Sigma_j(\overline{Y}_{ij*}-\overline{Y}_{i**}-\overline{Y}_{*j*}+\overline{Y}_{***})^2}{(p-1)(o-1)}$
S_E^2	$\frac{\Sigma_i\Sigma_j\Sigma_k(Y_{ijk}-\overline{Y}_{ij*})^2}{po(r-1)}$
$\overline{Y}_{i**}$	$\frac{\Sigma_j\Sigma_k Y_{ijk}}{or}$
$\overline{Y}_{*j*}$	$\frac{\Sigma_i\Sigma_k Y_{ijk}}{pr}$
$\overline{Y}_{ij*}$	$\frac{\Sigma_k Y_{ijk}}{r}$
$\overline{Y}_{***}$	$\frac{\Sigma_i\Sigma_j\Sigma_k Y_{ijk}}{por}$

Figure 5.25 Mean squares and means for the model

As an estimate of S_P^2, S_o^2 e S_{PO}^2 it is possible to use the value previously calculated with Minitab®:

Two-Way ANOVA Table With Interaction

Source	DF	SS	MS	F	P
Part	14	41,8582	2,98987	157,698	0,000
Operator	3	0,9044	0,30146	15,900	0,000
Part * Operator	42	0,7963	0,01896	1,469	0,040
Repeatability	240	3,0966	0,01290		
Total	299	46,6554			

α to remove interaction term = 0,05

Therefore, using the values of p=15, o=4, r=5, chosen for the design of the Gauge R&R of Calotest, and inserting them in equation (5.1) and (5.2), L and U are obtained. Knowing L and U, $1-\rho=\frac{\gamma_M}{\gamma_M+\gamma_P}$ confidence interval bounds are consequently obtained, since they are equal to $\left[\frac{1}{1+U},\frac{1}{1+L}\right]$.

These are the limits of the confidence interval for the percentage of variation introduced by the total Gage R&R.
Calculation of $\left[\frac{1}{1+U}, \frac{1}{1+L}\right]$ with Matlab® end up in:

```
lb_GoverT_p =

    0.0419


ub_GoverT_p =

    0.3609
```

If we compare the values above with the results provided with Minitab®, the two confidence intervals appear very similar:

Gage R&R

Source	VarComp	95% CI	%Contribution (of VarComp)	95% CI
Total Gage R&R	0,017881	(0,015; 0,070)	10,74	(4,49; 33,37)
Repeatability	0,012902	(0,011; 0,016)	7,75	(3,23; 13,75)
Reproducibility	0,004978	(0,002; 0,057)	2,99	(0,80; 26,39)
Operator	0,003767	(0,001; 0,056)	2,26	(0,50; 25,72)
Operator*Part	0,001211	(0,000; 0,004)	0,73	(0,00; 2,49)
Part-To-Part	0,148545	(0,079; 0,371)	89,26	(66,63; 95,51)
Total Variation	0,166426	(0,097; 0,395)	100,00	

Confidence interval estimation method previously described can be iterated varying the number of parts, result is expressed in the following graph

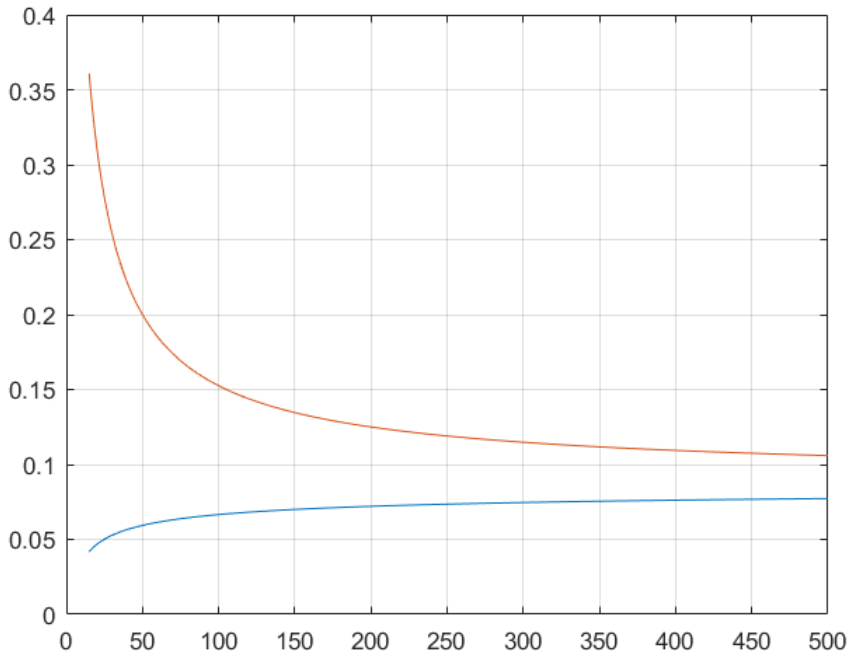

Figure 5.26: Lower and upper confidence interval limits of the Total Gage R&R variance contribution, in function of the amount of parts (samples) employed.

It is possible to see that the width of the interval can be highly reduced increasing the number of parts employed in the Gage R&R study.

5.2.2 Repeatability of Fischerscope® X-DAL

Fischerscope® X-DAL is the other coating thickness measurement device, available in Oerlikon Balzers laboratory.
This instrument performs non-destructive measurement of the coating thickness, but it can measure only metal-based coating (e.g. not suitable for DLC coatings).
In addition to that, it is possible to measure only substrate-coating couples which have a defined "recipe" in the machine software. Therefore, materials must be completely known from a physical and chemical point of view.
XRF measurement process is considered a priori to be perfectly reproducible, since the operator have just to place the sample on the measurement plate and launch the automatic measurement from the machine software.
Since any appraiser source of variation is considered negligible, the total Gage R&R variation component comes just from the instrument repeatability.
The design of experiment is composed by 15 parts, each of them will be measured for 5 repetitions, by 1 appraiser.
The following graph displays measurements of the 15 sampled parts.
Part to part variation appears overwhelmingly higher than repeatability.

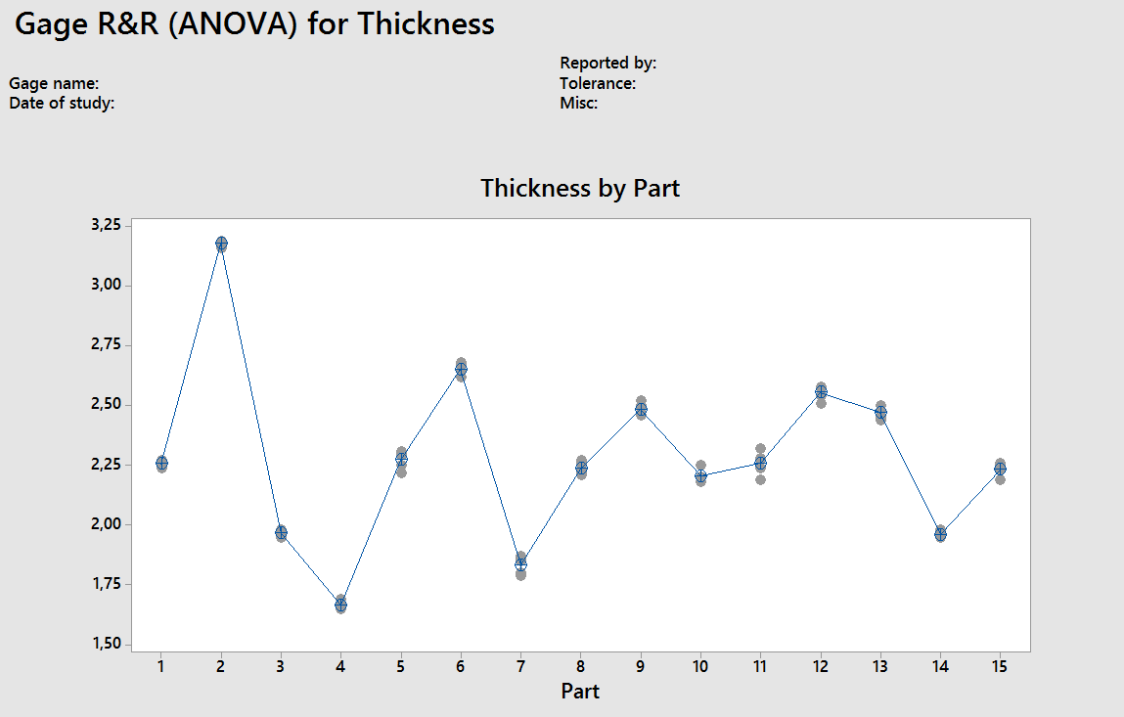

Figure 5.27

Anova table confirms the previous impression.
The instrument is able to discriminate the difference from part to part.

Analysis of Variance

Source	DF	Adj SS	Adj MS	F-Value	P-Value
Part	14	9,45307	0,675219	920,75	0,000
Error	60	0,04400	0,000733		
Total	74	9,49707			

Model Summary

S	R-sq	R-sq(adj)	R-sq(pred)
0,0270801	99,54%	99,43%	99,28%

Before introducing the repeatability estimate, it is necessary to check ANOVA hypothesis.
Equality of variance of standardized residuals cannot be refused.

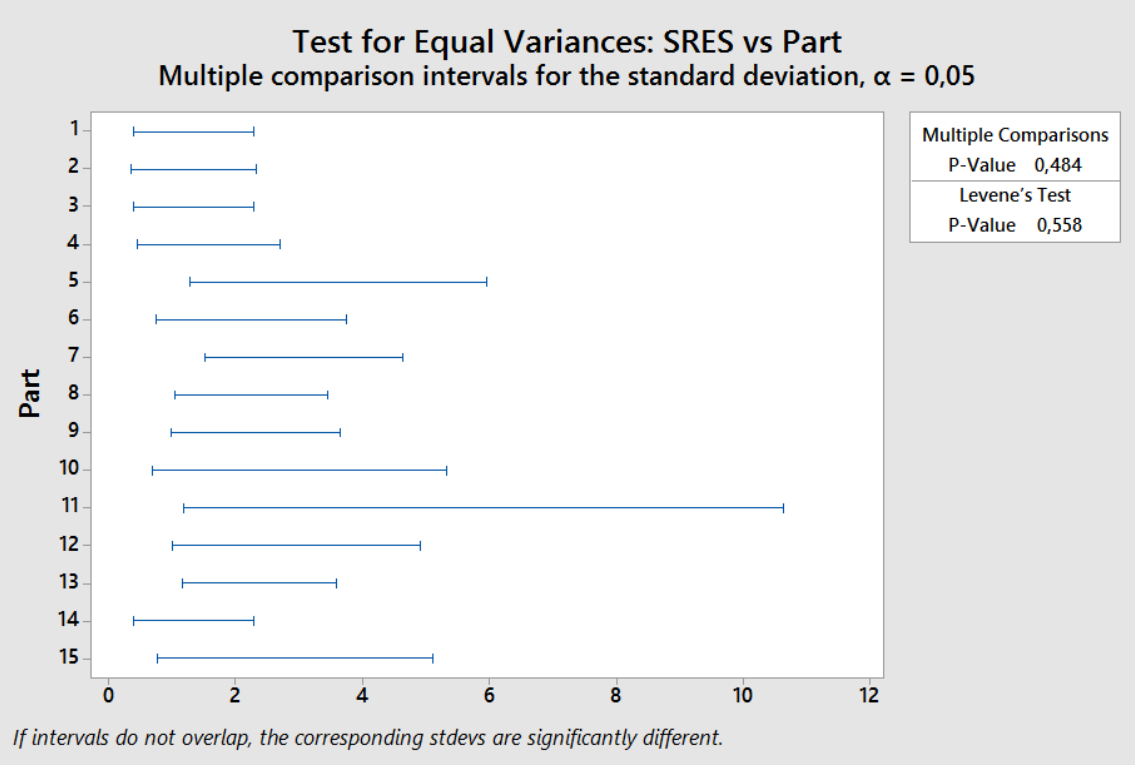

Figure 5.28

Equality of variance cannot be refused.

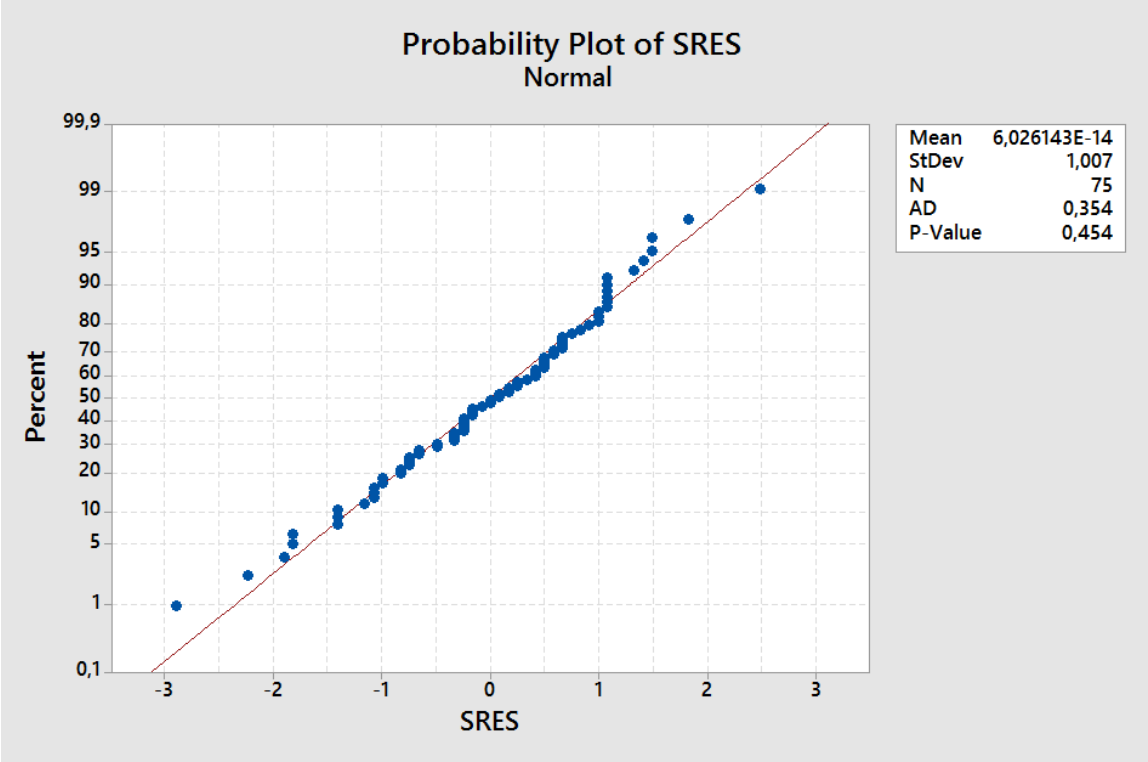

Figure 5.29

Residuals are within the interval of (-3,+3), no obvious patterns are observed.

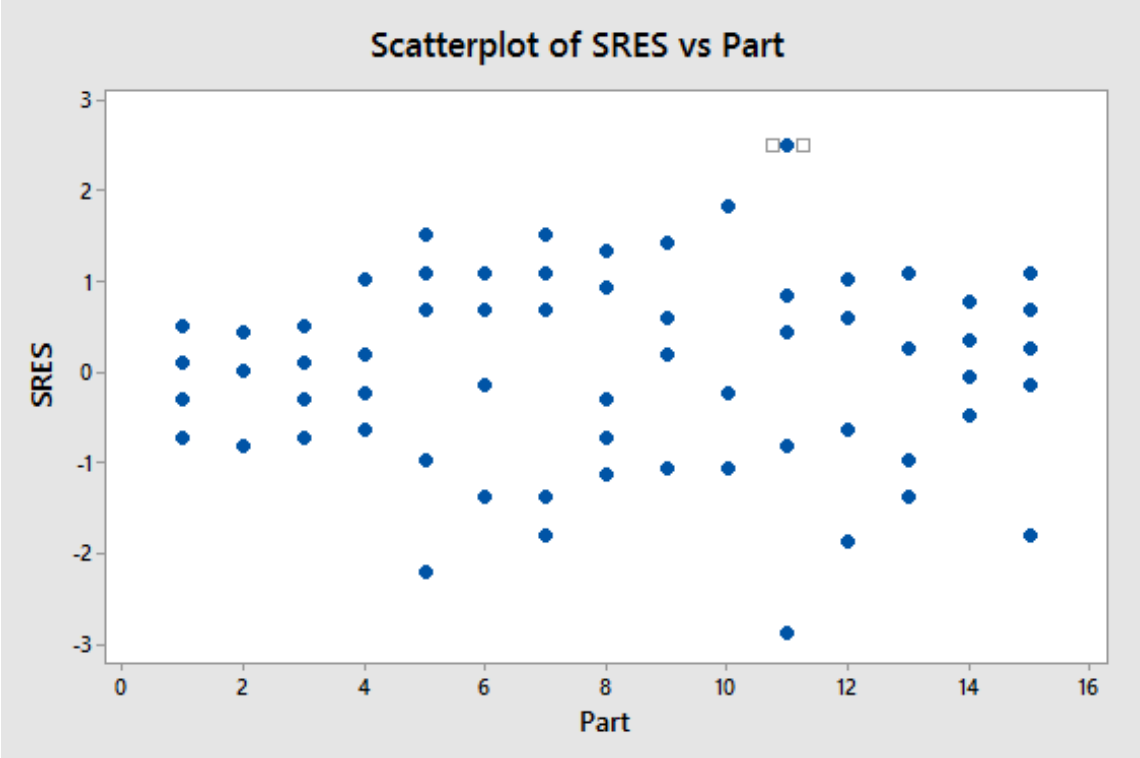

Figure 5.30

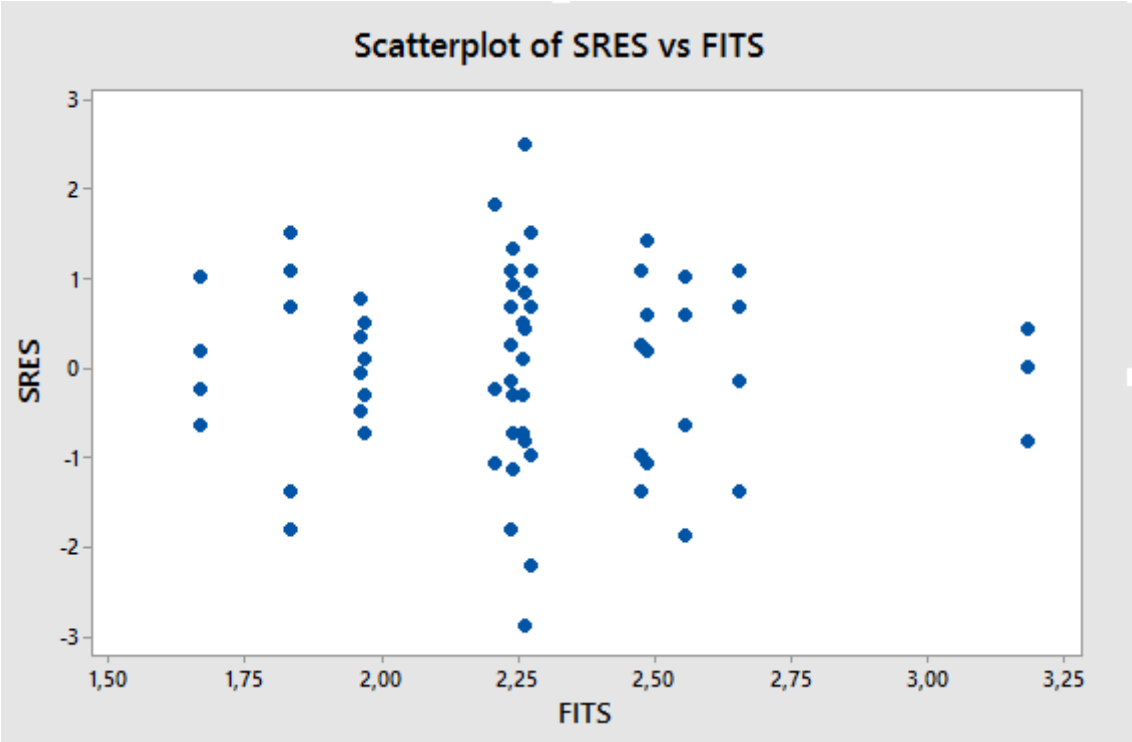

Figure 5.31

Autocorrelation is not significant; therefore, time dependency can be excluded.

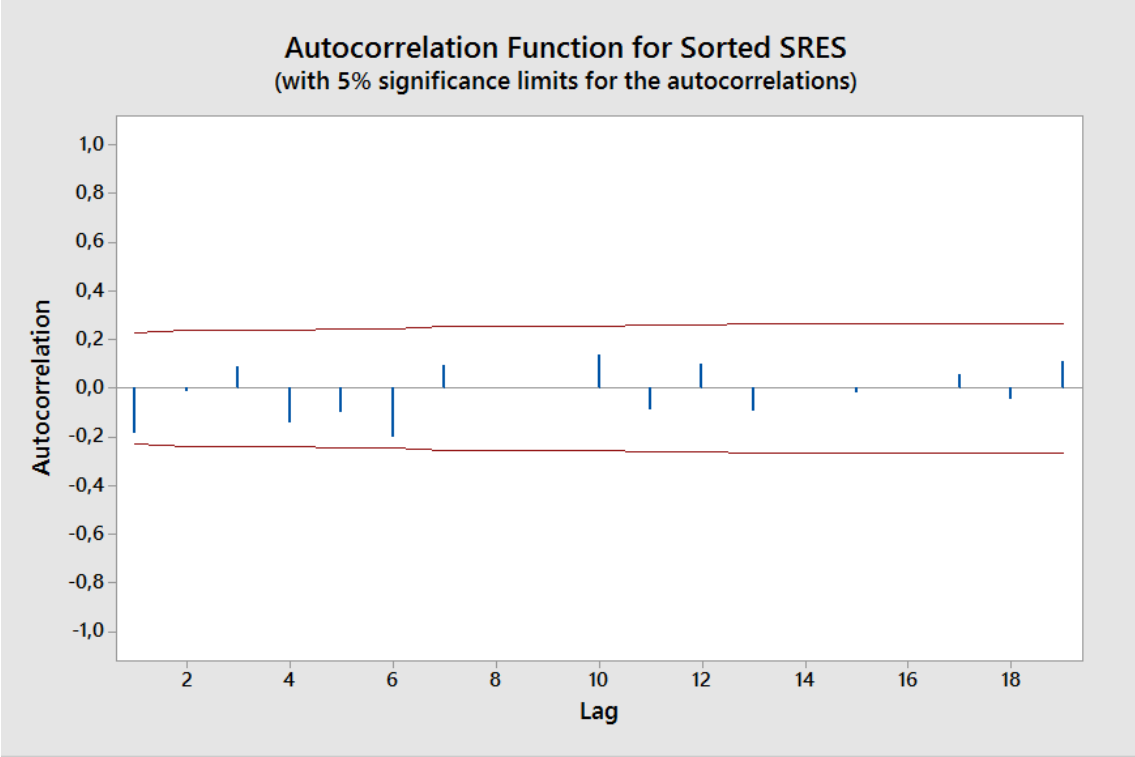

Figure 5.32

As previously said, total Gage R&R variation component is made just by repeatability.

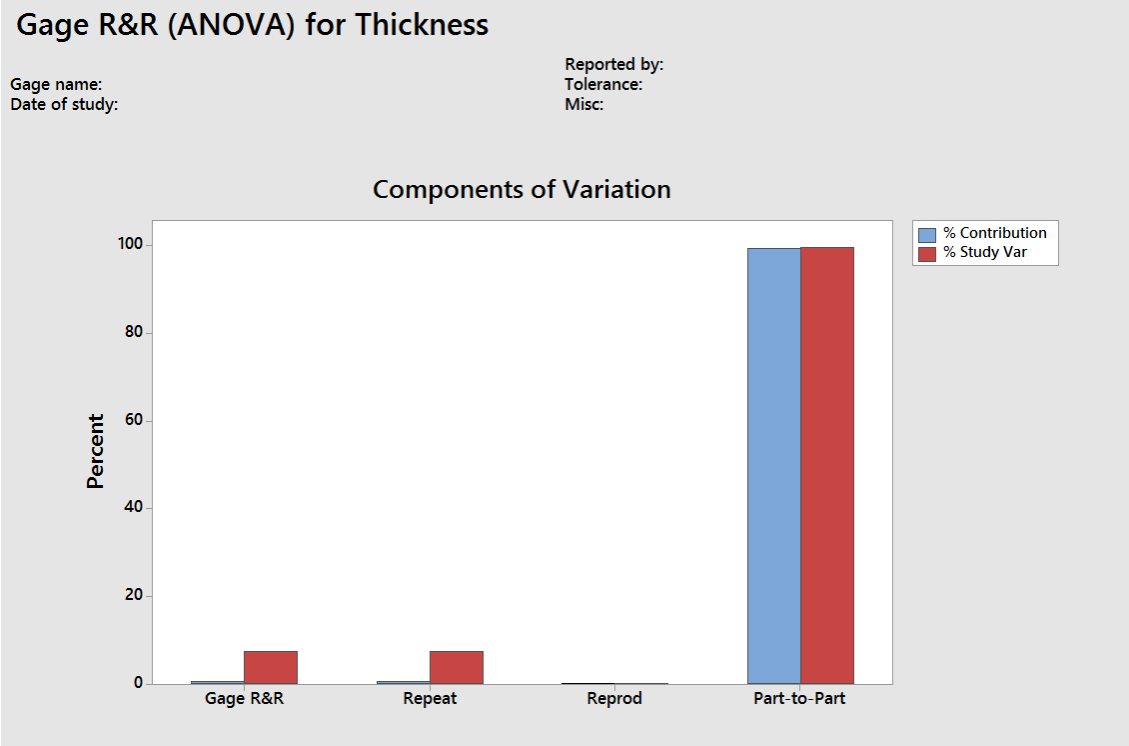

Gage R&R

Source	VarComp	95% CI	%Contribution (of VarComp)	95% CI
Total Gage R&R	0,000733	(0,001; 0,001)	0,54	(0,21; 1,13)
Repeatability	0,000733	(0,001; 0,001)	0,54	(0,21; 1,13)
Part-To-Part	0,134897	(0,072; 0,336)	99,46	(98,87; 99,79)
Total Variation	0,135630	(0,073; 0,336)	100,00	

Source	StdDev (SD)	95% CI	Study Var (6 × SD)	95% CI	%Study Var (%SV)
Total Gage R&R	0,027080	(0,023; 0,033)	0,16248	(0,138; 0,198)	7,35
Repeatability	0,027080	(0,023; 0,033)	0,16248	(0,138; 0,198)	7,35
Part-To-Part	0,367283	(0,269; 0,579)	2,20370	(1,613; 3,477)	99,73
Total Variation	0,368280	(0,270; 0,580)	2,20968	(1,621; 3,480)	100,00

Source	95% CI
Total Gage R&R	(4,55; 10,61)
Repeatability	(4,55; 10,61)
Part-To-Part	(99,44; 99,90)
Total Variation	

Number of Distinct Categories = 19
95% CI = (13,2504; 31,0225)

The point estimate for the Gage component of variance is equal to 0.54%, while the 95% confidence interval bounds are (0.21%,1.13%).
In conclusion, the XRF spectrometer introduces much less variability with respect to Calotest, its performance in this test shows it fully respects AIAG rules for measurement systems.
Therefore, for the following experiments, XRF spectrometer will be adopted as the standard measurement device, while Calotest will works as an auxiliary instrument, suitable to check spectrometer measurements.

Chapter 6

Factor Screening Experiment

The qualitative analysis has selected seven possible factors which could affect coating thickness during the manufacturing process:

- *Weight*: The presence of big tools/mould in the batch could influence the temperature and the electromagnetic field inside the coating chamber.
- *Position*: Vertical position in the chamber (e.g. high, medium, low).
- Rotation: Number of rotation axis of the substrate.
- *Maintenance*: The machine undergoes a scheduled preventive maintenance cycle
- *Target Weight*: Target contains the deposition material, before each batch they are weighed in order to estimate their grade of consumption.
- *Micro blasting*: Substrate surfaces are often micro blasted in order to polish the surface, uniform roughness and enhance coating adhesion.
- *Substrate Material*: The base material of the part to be coated

In order to verify the influence of these factors on the output characteristic, a factor screening experiment has been set up.
Six of the seven factors are made of two levels coded wit ±1 values, while the last one (material), is composed by three levels, coded M S K.

- *Weight*: 2 levels. As the saturation of the carousel could influence the coating thickness, two factor levels are obtained on the base of the amount of carousel shaft loaded with heavy gear cutting tools. If the number of shafts loaded with gear cutting tools are less than 5, a batch is considered as “light” (Code -1), otherwise it is “heavy” (Code 1).
- *Position*: 2 levels. Highest position on the carousel (1), lowest position (-1).
- Rotation: 2 levels. The number of planetary rotation of the substrate considered is one (-1) or two (1).
- *Maintenance*: 2 levels. “Old” (-1), from 20 batches from the next maintenance, and “new” (1), up to 20 batches starting from the last maintenance intervention.
- *Target Weight*: 2 levels. Targets are literally weighted before each process, in order to estimate their level of consumption. On the base of their weight, they are classified in “new”, “medium” and “old” target. In this experiment only “new” (-1) and “old” (1) target are considered.
- *Micro blasting*:2 levels Two surface finishing conditions are considered. Samples employed are uniformly grinded and polished, in order to reach a roughness finishing Ra of 0.02 µm. After the treatment, half of the total amount have been micro blasted (1), a treatment generally performed to enhance adhesion. The other half has been left in polishing condition (-1).
- *Material*: 3 levels. Substrate materials adopted are the most common steels and a cemented carbide quality. (Bohler K110 cold working steel (code K), Bohler S600 high speed steel (code S) and Ceratizit CTE40 cemented carbide (code M)).

For each of the 3 materials, 16 runs have been per formed, in order to obtain 3 x 2^(6-2) fractional factorial design. Every 2^(6-2) design is without replicates, with a resolution equal to IV.

Std. Order	MICRO BLASTING	WEIGHT	TARGET WEIGHT	MAINTENANCE	POSITION	ROTATION
1	-1	-1	-1	-1	-1	-1
2	1	-1	-1	-1	1	-1
3	-1	1	-1	-1	1	1
4	1	1	-1	-1	-1	1
5	-1	-1	1	-1	1	1
6	1	-1	1	-1	-1	1
7	-1	1	1	-1	-1	-1
8	1	1	1	-1	1	-1
9	-1	-1	-1	1	-1	1
10	1	-1	-1	1	1	1
11	-1	1	-1	1	1	-1
12	1	1	-1	1	-1	-1
13	-1	-1	1	1	1	-1
14	1	-1	1	1	-1	-1
15	-1	1	1	1	-1	1
16	1	1	1	1	1	1

Table 6.1: 2^ (6-2) Fractional factorial design

6.1 Analysis of fractional factorial designs without replicates

Runs have been performed in 16 different coating batches of the same process, (AlCrN-based coating). In every batch one sample for each material type has been included. Measures were taken in the centre of the circular face exposed to targets, the other face specimens to coating fixtures.

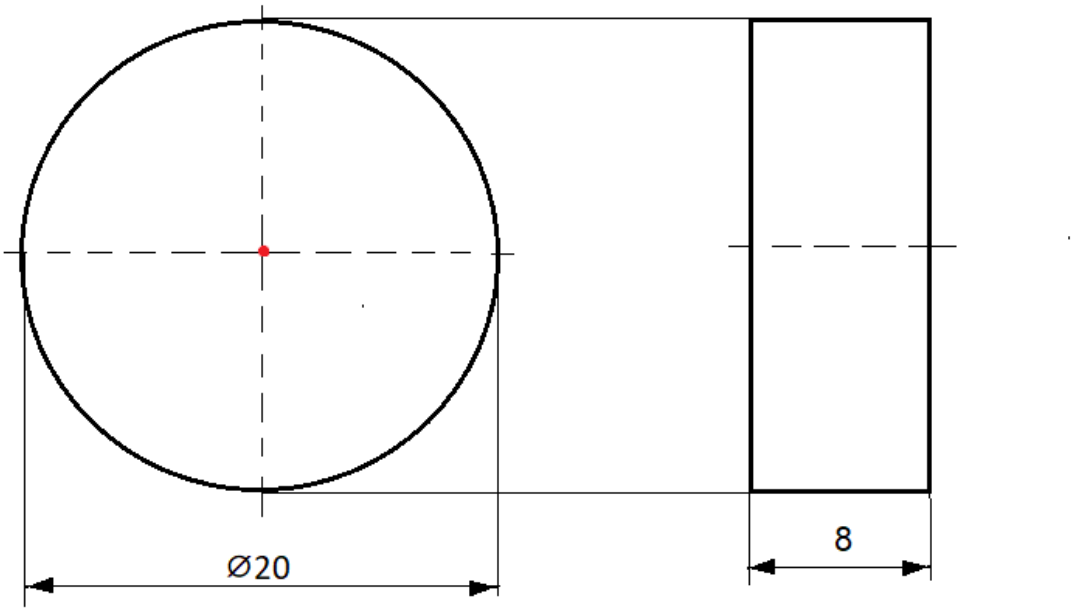

Figure 6.1: Specimens dimensions used in factor screening experiments. Red dot represents the measurement point.

The following scatterplot shows thickness measured on specimens in the 16 conditions, for all 3 materials.

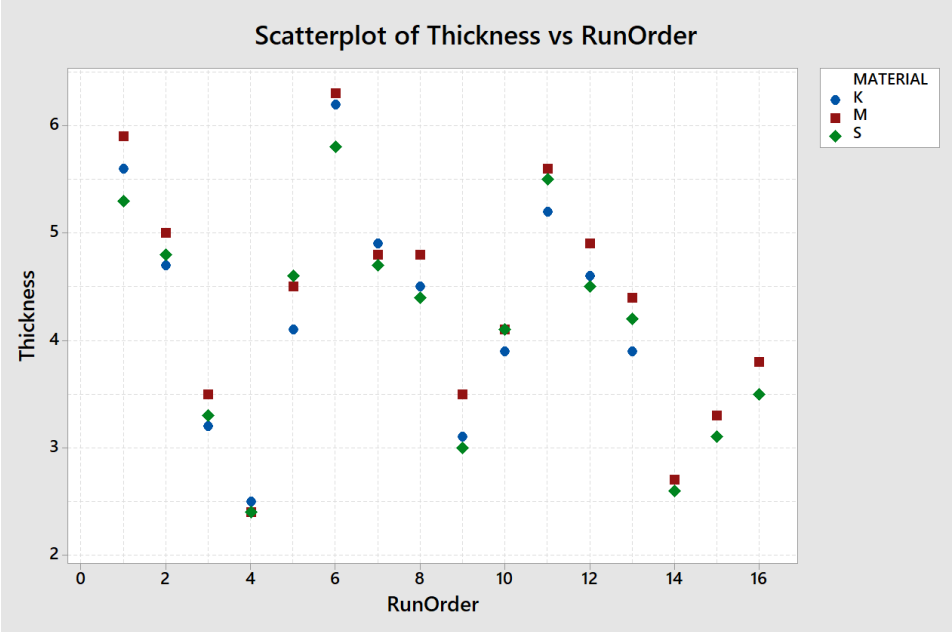

Figure 6.2: Scatterplot of thickness for all 16 conditions of the fractional factorial design, Output obtained for each material is displayed.

A separate analysis for each of the three fractional factorial designs, one for each material, has been performed.
Since the three experimental plans are without replicates, the significance level of factors can be determined by normal plots of the effect.
The normal plots of the effect show the same significant factors.
It is clearly visible that, among the six factors taken into account, “position” and “rotation” have a dominant effect.
“Micro blasting”, “Weight”, “Target weight” and “Maintenance” seems to be much less significant.
It is an important result, since the coating process appears robust to variation of machine conditions and saturation.
Even micro blasting pre-treatment it is not a significant factor for coating thickness variation. Probably it would be a relevant factor, if the output of was coating adhesion, instead of coating thickness.

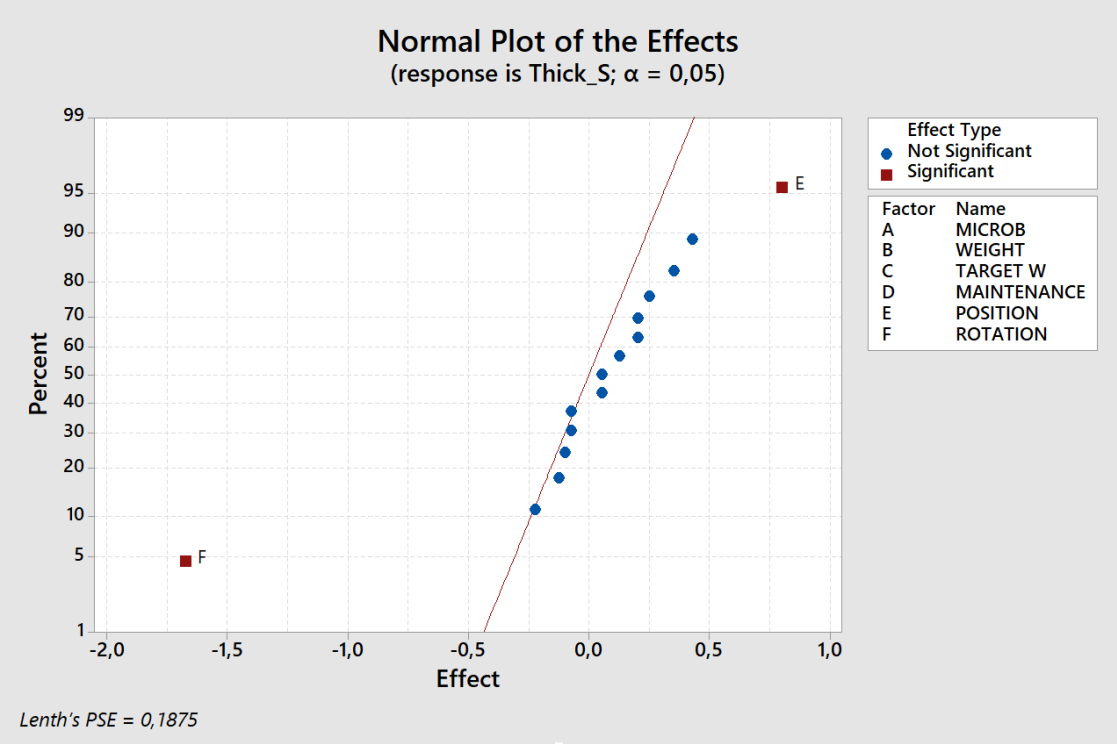

Figure 6.3: Normal plot of the effects for “S” material samples

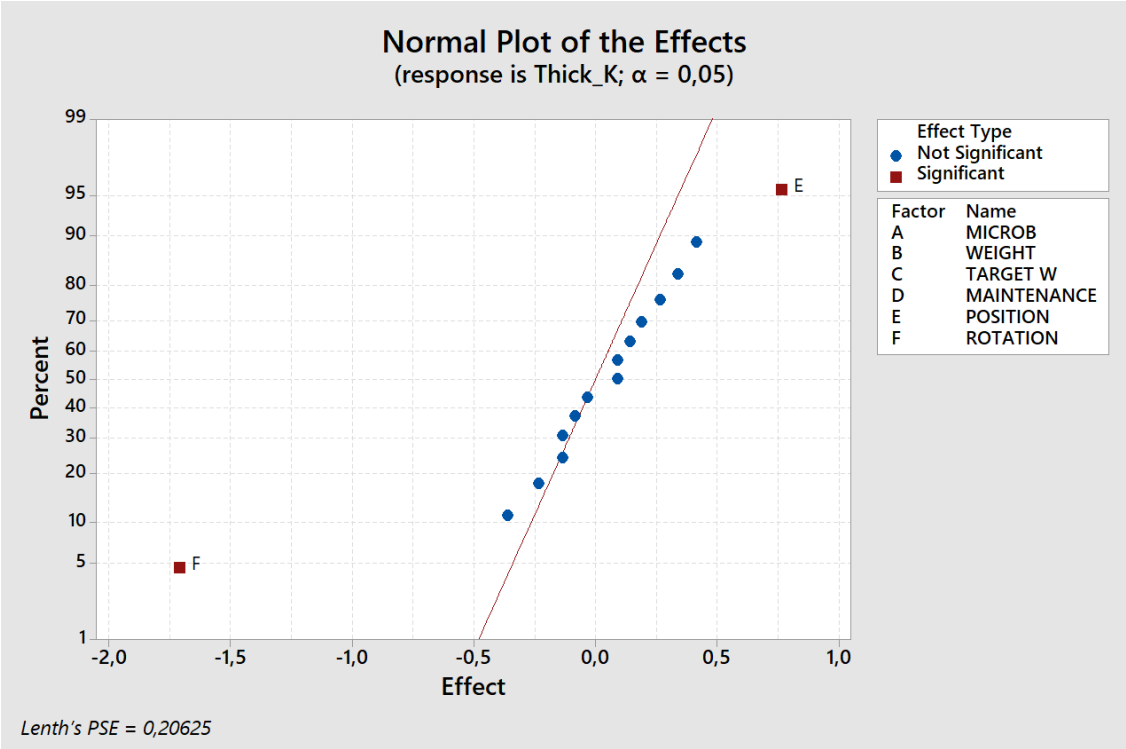

Figure 6.4: Normal plot of the effects for "K" material.

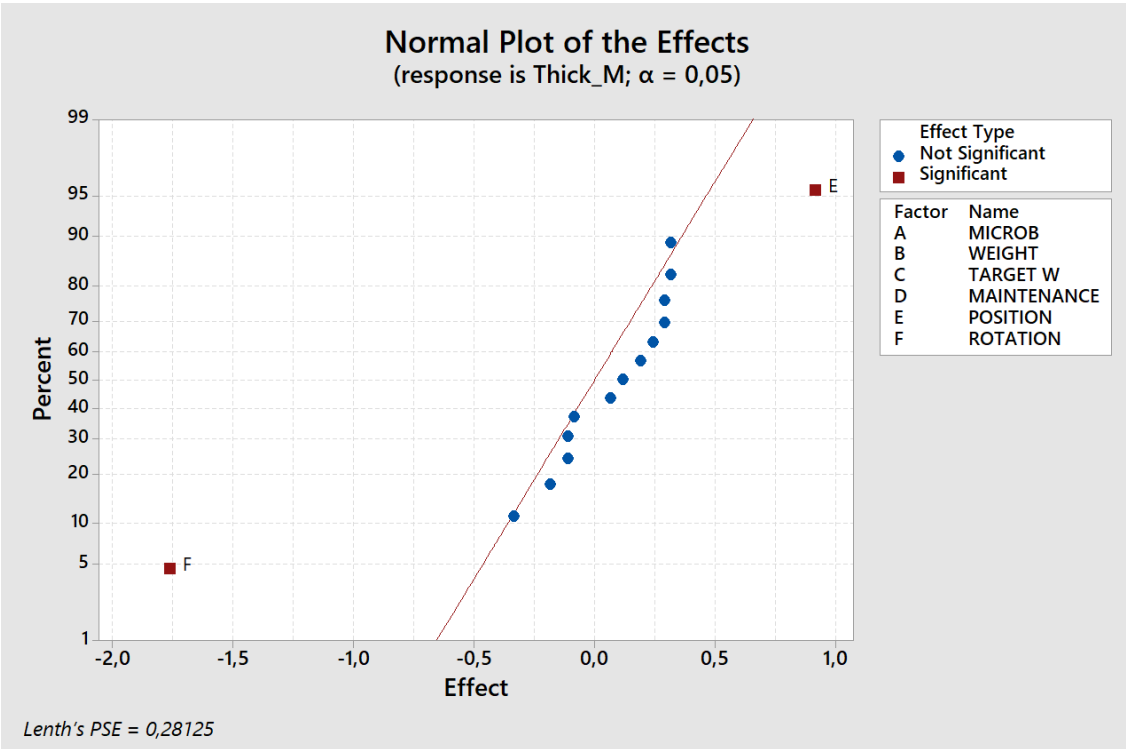

Figure 6.5: Normal plot of the effects for "M" material.

6.2 Full factorial design analysis

Once identified two relevant factors, a new analysis has been performed, considering factors “position”, “rotation” and “material”, and their interaction.
New design uses data of the previous analysis, but since the number of factor has been reduced, it has been possible to obtain a general full factorial design with 4 replicates.
Before introducing the ANOVA analysis, main effect and interaction plots have been displayed.
Main effects of position and rotation seem to be more relevant with respect to the base material effect.

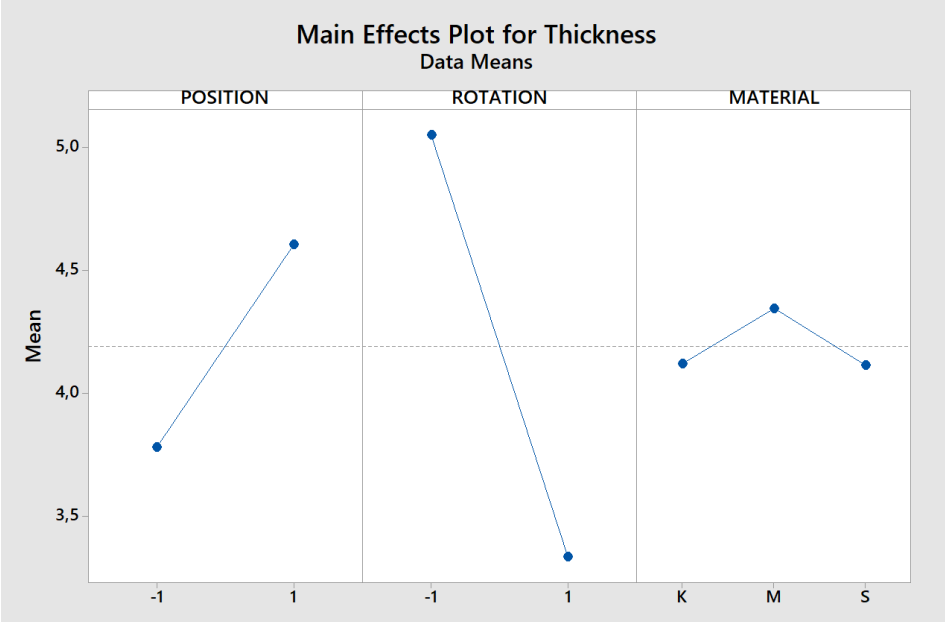

Figure 6.6

Interaction seems to be not significant in any case.

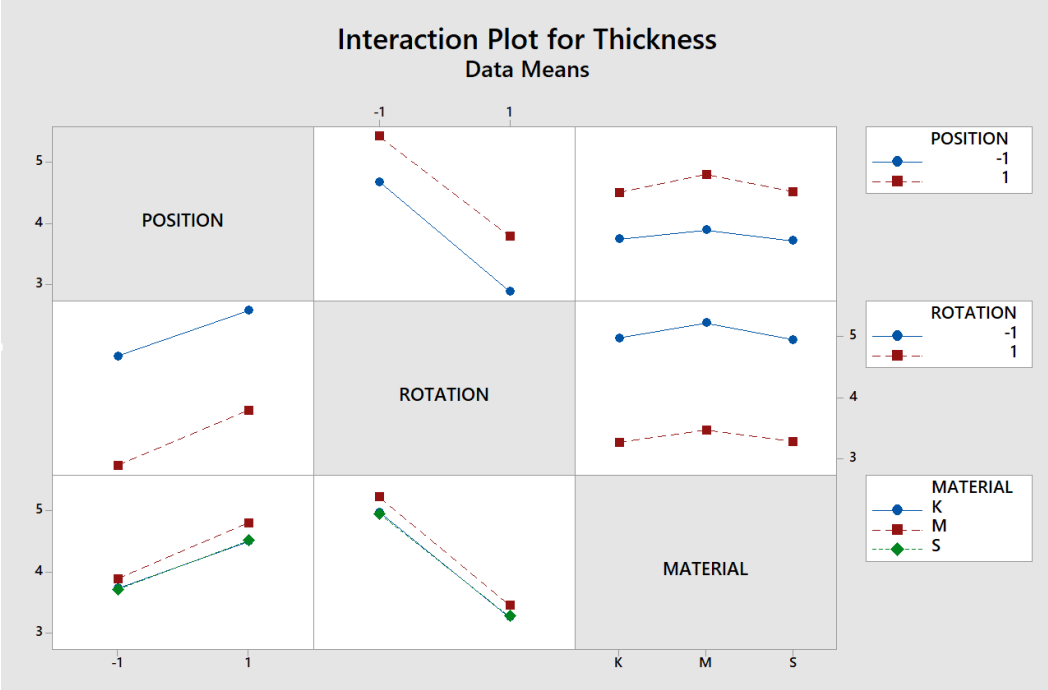

Figure 6.7

The ANOVA table is then displayed.

General Linear Model: Thickness versus POSITION; ROTATION; MATERIAL

Method

Factor coding (-1; 0; +1)

Factor Information

Factor	Type	Levels	Values
POSITION	Fixed	2	-1; 1
ROTATION	Fixed	2	-1; 1
MATERIAL	Fixed	3	K; M; S

Analysis of Variance

Source	DF	Adj SS	Adj MS	F-Value	P-Value
POSITION	1	8,1675	8,1675	40,47	0,000
ROTATION	1	35,3633	35,3633	175,23	0,000
MATERIAL	2	0,5554	0,2777	1,38	0,266
POSITION*ROTATION	1	0,0675	0,0675	0,33	0,567
POSITION*MATERIAL	2	0,0487	0,0244	0,12	0,887
ROTATION*MATERIAL	2	0,0154	0,0077	0,04	0,963
POSITION*ROTATION*MATERIAL	2	0,1137	0,0569	0,28	0,756
Error	36	7,2650	0,2018		
Total	47	51,5967			

Model Summary

S	R-sq	R-sq(adj)	R-sq(pred)
0,449228	85,92%	81,62%	74,97%

Coefficients

Term	Coef	SE Coef	T-Value	P-Value	VIF
Constant	4,1917	0,0648	64,65	0,000	
POSITION					
-1	-0,4125	0,0648	-6,36	0,000	1,00
ROTATION					
-1	0,8583	0,0648	13,24	0,000	1,00
MATERIAL					
K	-0,0729	0,0917	-0,80	0,432	1,33
M	0,1521	0,0917	1,66	0,106	1,33
POSITION*ROTATION					
-1 -1	0,0375	0,0648	0,58	0,567	1,00
POSITION*MATERIAL					
-1 K	0,0312	0,0917	0,34	0,735	1,33
-1 M	-0,0437	0,0917	-0,48	0,636	1,33
ROTATION*MATERIAL					
-1 K	-0,0021	0,0917	-0,02	0,982	1,33
-1 M	0,0229	0,0917	0,25	0,804	1,33
POSITION*ROTATION*MATERIAL					
-1 -1 K	-0,0563	0,0917	-0,61	0,543	1,33
-1 -1 M	-0,0062	0,0917	-0,07	0,946	1,33

```
Regression Equation

Thickness = 4,1917 - 0,4125 POSITION_-1 + 0,4125 POSITION_1 + 0,8583 ROTATION_-1
            - 0,8583 ROTATION_1 - 0,0729 MATERIAL_K + 0,1521 MATERIAL_M - 0,0792 MATERIAL_S
            + 0,0375 POSITION*ROTATION_-1 -1 - 0,0375 POSITION*ROTATION_-1 1
            - 0,0375 POSITION*ROTATION_1 -1 + 0,0375 POSITION*ROTATION_1 1
            + 0,0312 POSITION*MATERIAL_-1 K - 0,0437 POSITION*MATERIAL_-1 M
            + 0,0125 POSITION*MATERIAL_-1 S - 0,0312 POSITION*MATERIAL_1 K
            + 0,0437 POSITION*MATERIAL_1 M - 0,0125 POSITION*MATERIAL_1 S
            - 0,0021 ROTATION*MATERIAL_-1 K + 0,0229 ROTATION*MATERIAL_-1 M
            - 0,0208 ROTATION*MATERIAL_-1 S + 0,0021 ROTATION*MATERIAL_1 K
            - 0,0229 ROTATION*MATERIAL_1 M + 0,0208 ROTATION*MATERIAL_1 S
            - 0,0563 POSITION*ROTATION*MATERIAL_-1 -1 K
            - 0,0062 POSITION*ROTATION*MATERIAL_-1 -1 M
            + 0,0625 POSITION*ROTATION*MATERIAL_-1 -1 S
            + 0,0563 POSITION*ROTATION*MATERIAL_-1 1 K + 0,0062 POSITION*ROTATION*MATERIAL_-1
            1 M - 0,0625 POSITION*ROTATION*MATERIAL_-1 1 S
            + 0,0563 POSITION*ROTATION*MATERIAL_1 -1 K + 0,0062 POSITION*ROTATION*MATERIAL_1
            -1 M - 0,0625 POSITION*ROTATION*MATERIAL_1 -1 S
            - 0,0563 POSITION*ROTATION*MATERIAL_1 1 K - 0,0062 POSITION*ROTATION*MATERIAL_1 1
            M + 0,0625 POSITION*ROTATION*MATERIAL_1 1 S
```

Even in this analysis, only axial position and rotation modes seem to affect the response.
No interaction can be considered relevant.
Before accepting the result, it is necessary to check ANOVA hypothesis.

Normality hypothesis of standardized residuals cannot be refused.

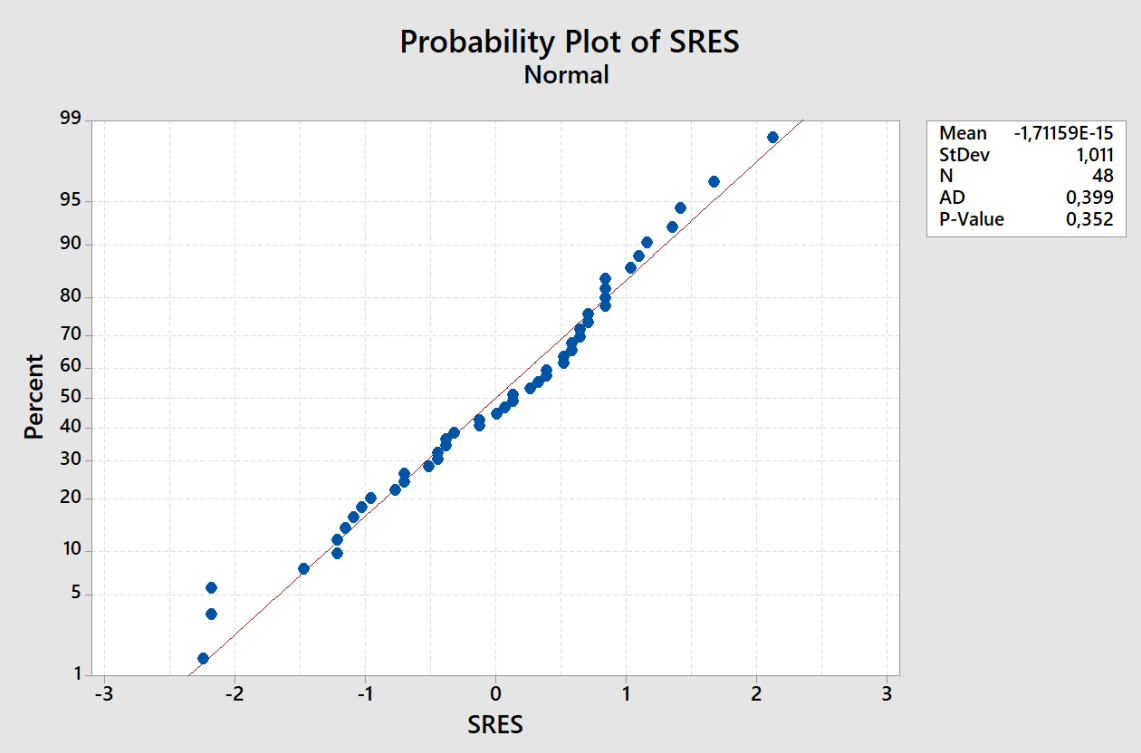

Figure 6.8

Equality of variances cannot be refused.

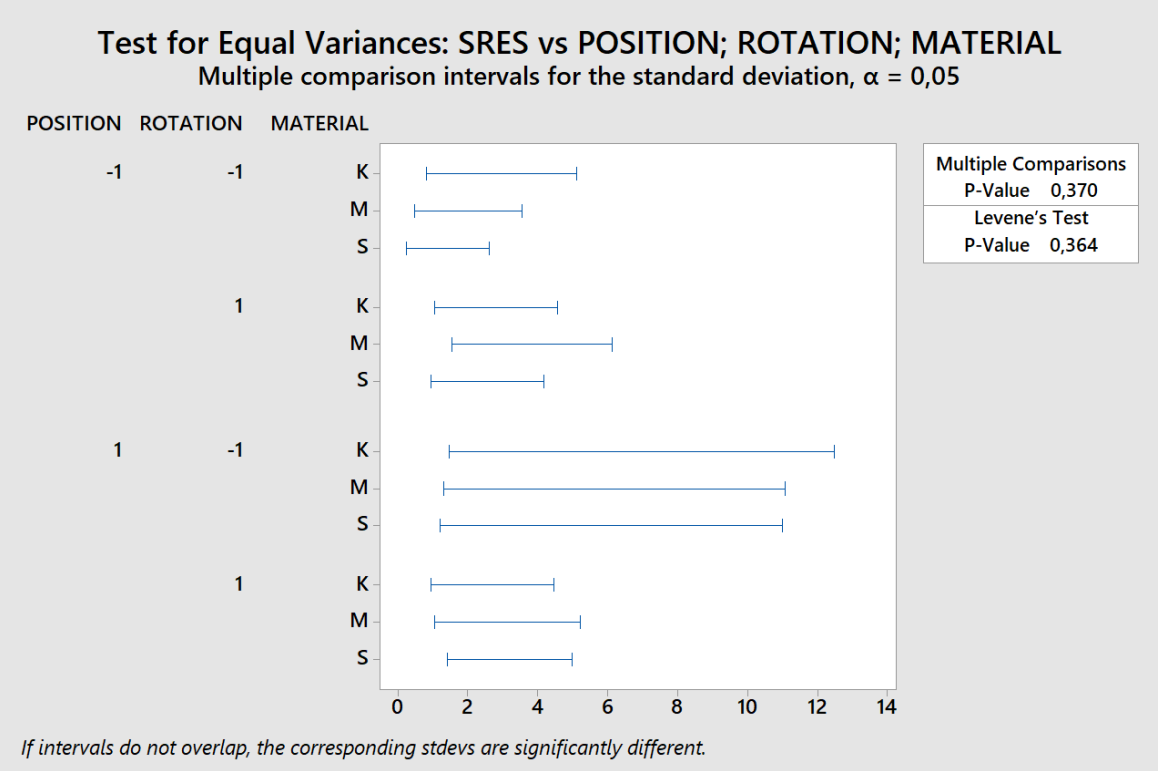

Figure 6.9

All standardized residuals belong to (-3, +3) interval, therefore no outliers appear. Residuals does not follow any obvious pattern.

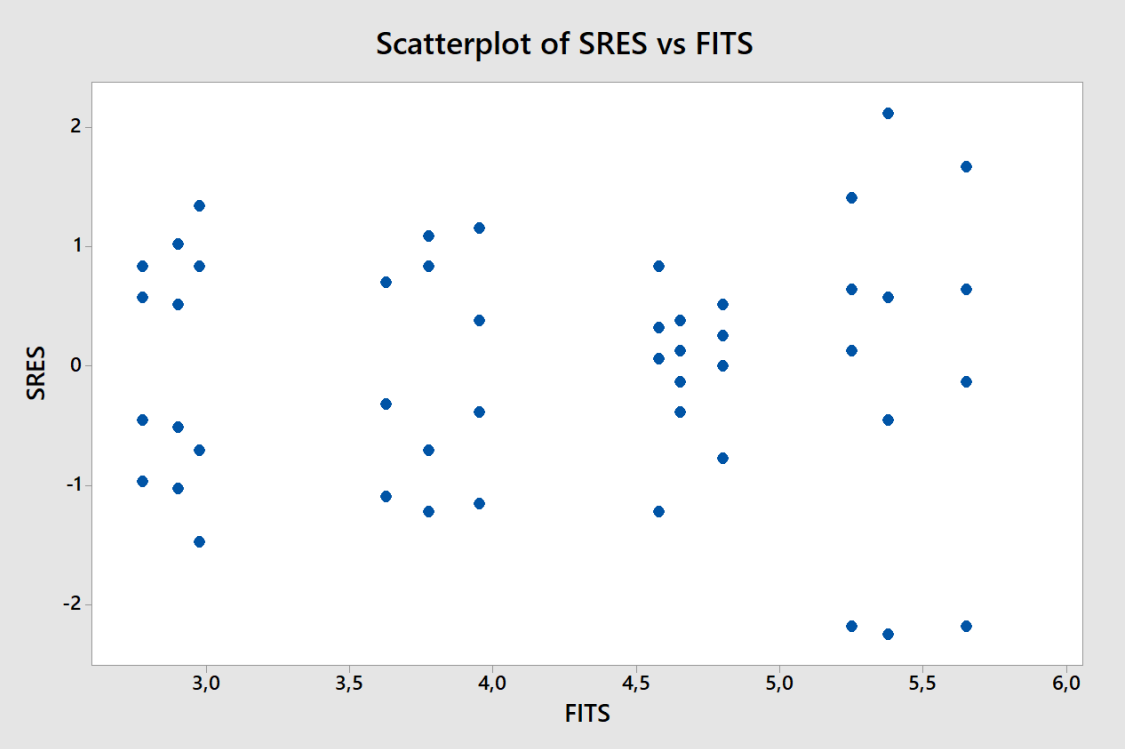

Figure 6.10

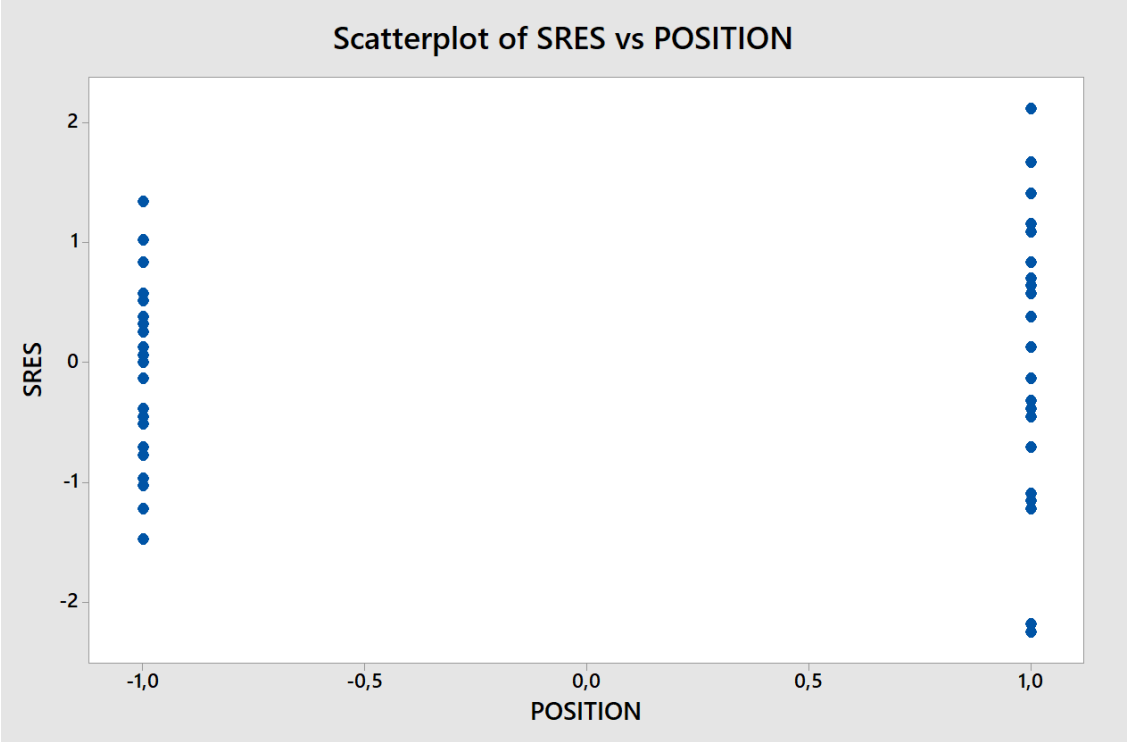

Figure 6.11

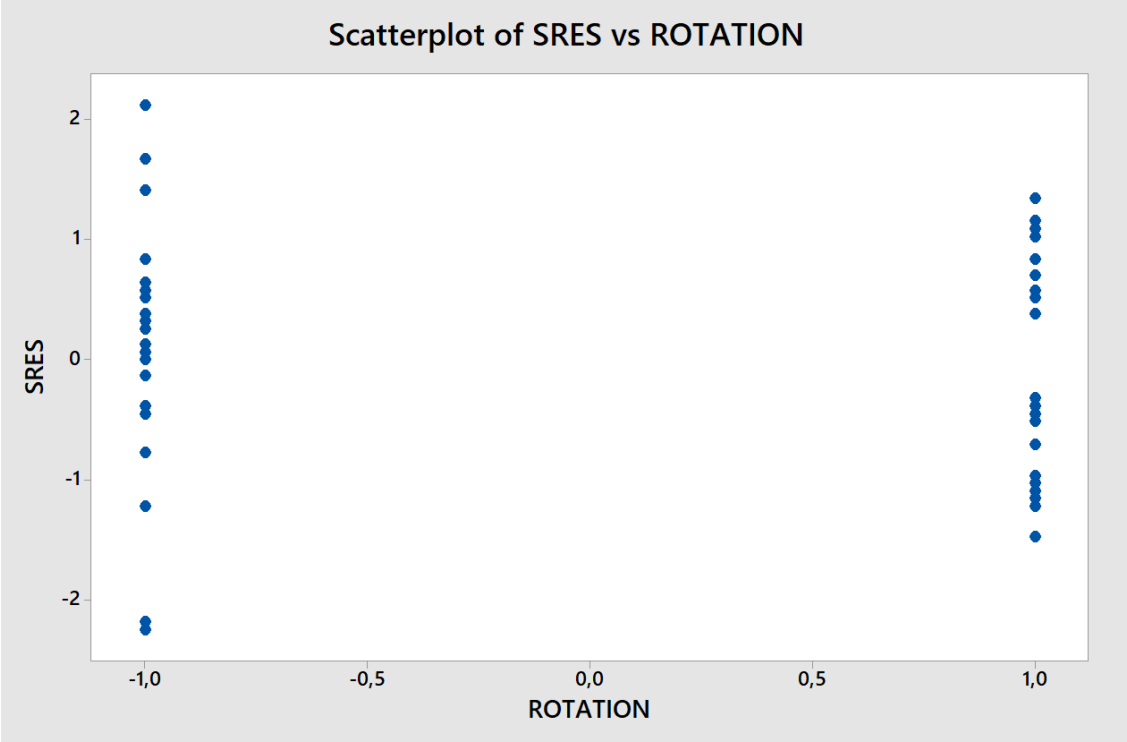

Figure 6.12

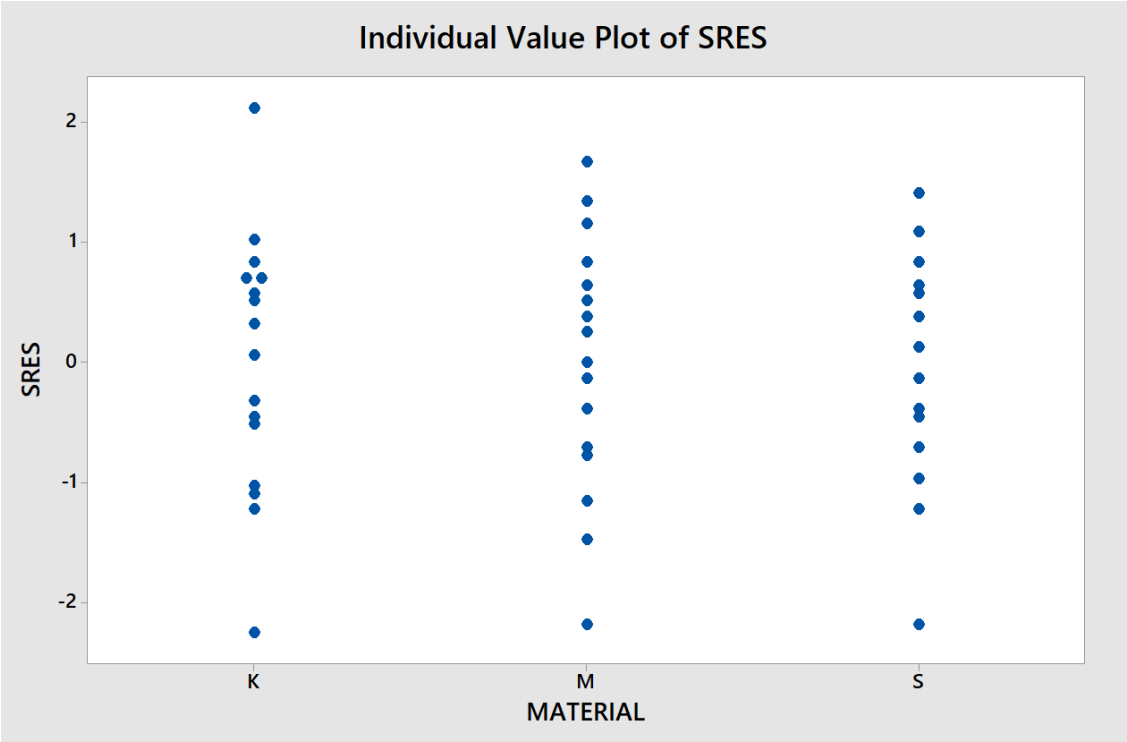

Figure 6.13

Autocorrelation of standardized residuals have been performed, no significance limits is reached, therefore no time dependency has been detected.

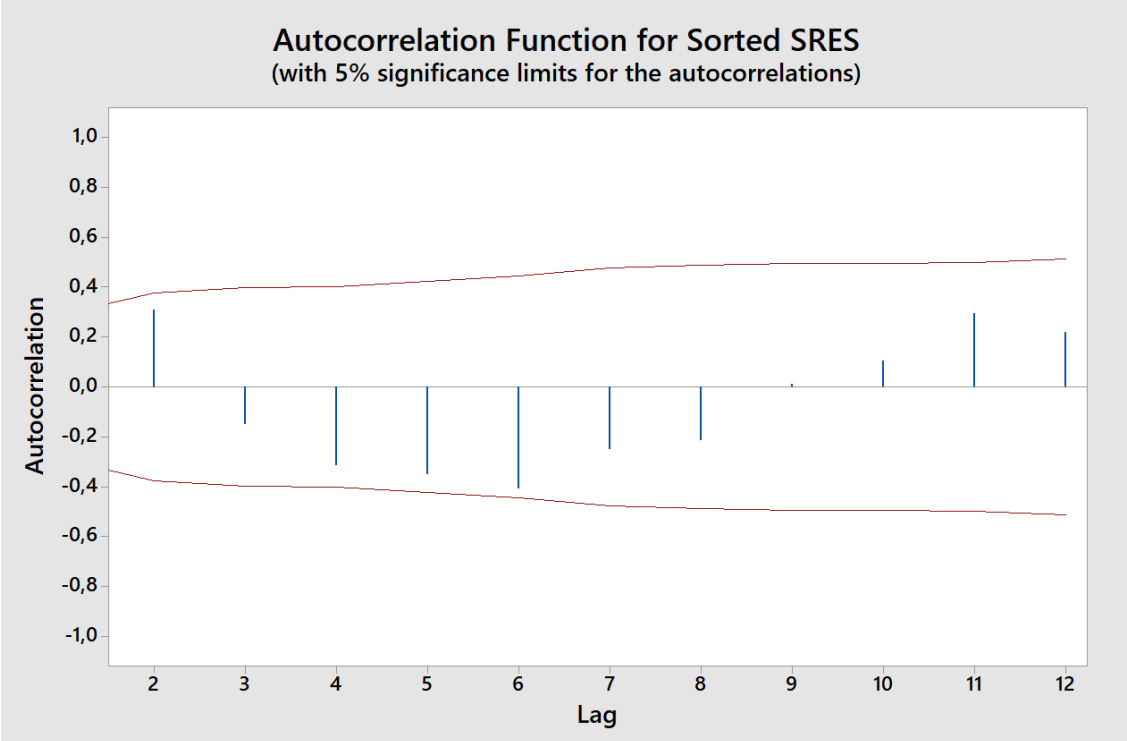

Figure 6.15

Power of the experiment has been calculated with Minitab®.
The selected design has a power of 95% with a minimum difference of interest of 0.65 [µm].
This result is acceptable in this screening experiment, even if lower minimum differences with the same power level can be reached increasing the number of replicates.

Power and Sample Size

```
General Full Factorial Design

α = 0,05  Assumed standard deviation = 0,4492

Factors: 3  Number of levels: 3; 2; 2

Include terms in the model up through order:  3
Not including blocks in model.
```

Reps	Total Runs	Power	Maximum Difference
4	48	0,95	0,651277

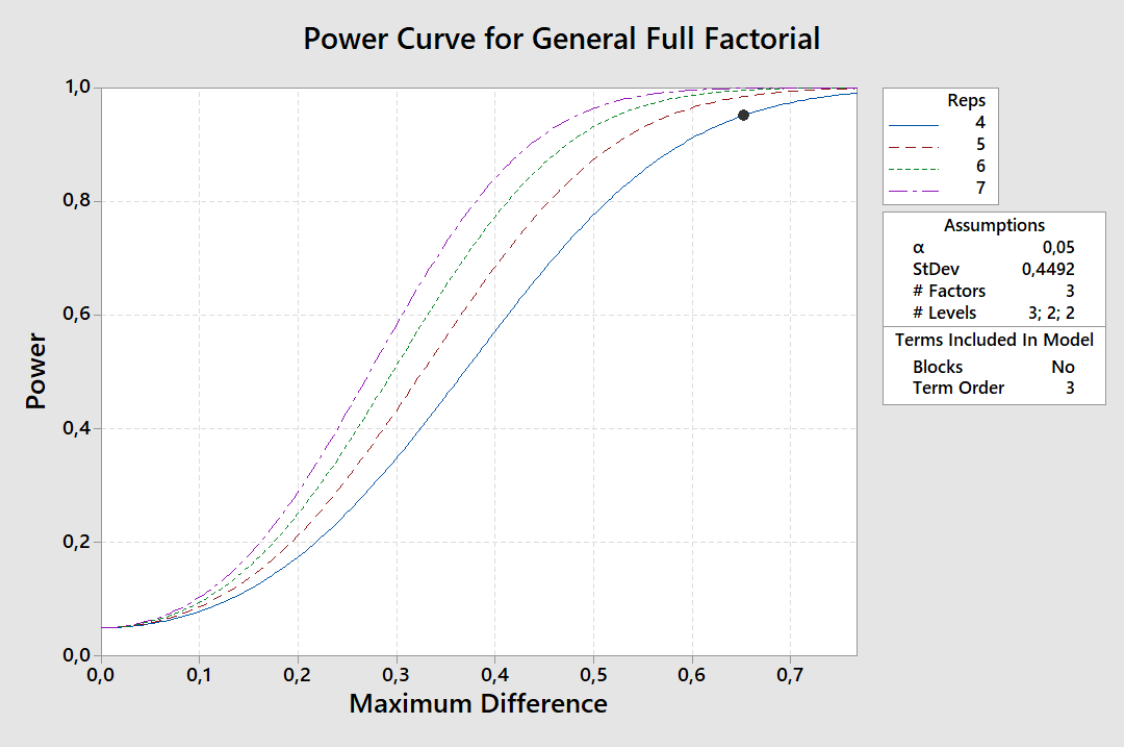

Figure 6.14: Power curves of the selected design, with 4,5, 6 and 7 replicates.

Chapter 7

Main Experimental Campaign

7.1 Single measurement point analysis

Factor screening experiment allowed to identify two factors which affect coating thickness: axial position inside the chamber and rotation modes on the carousel.
In order to develop a more detailed model, a new experimental campaign has been set. The design of the experiment is composed by the two factors “position” and “rotation”, with 3 levels for each factor.

- Axial position levels are “low”, “middle”, “high”
- Rotation modes are 1,2,3-fold rotations.

The number of replicates is 6, 3 within the same batch * 2 between distinct batches.

In total, 54 runs have been performed.

Geometry of specimens is the same of the factor screening experiments, cylindrical specimens ⌀20 x 8 mm. Like in the previous analysis, samples have been measured in the centre of the face exposed to targets.

Since variability within and between batches must be evaluated separately, factor “Repetition Between” has been included in the analysis.

Main effect of variation between different batches seems not significant:

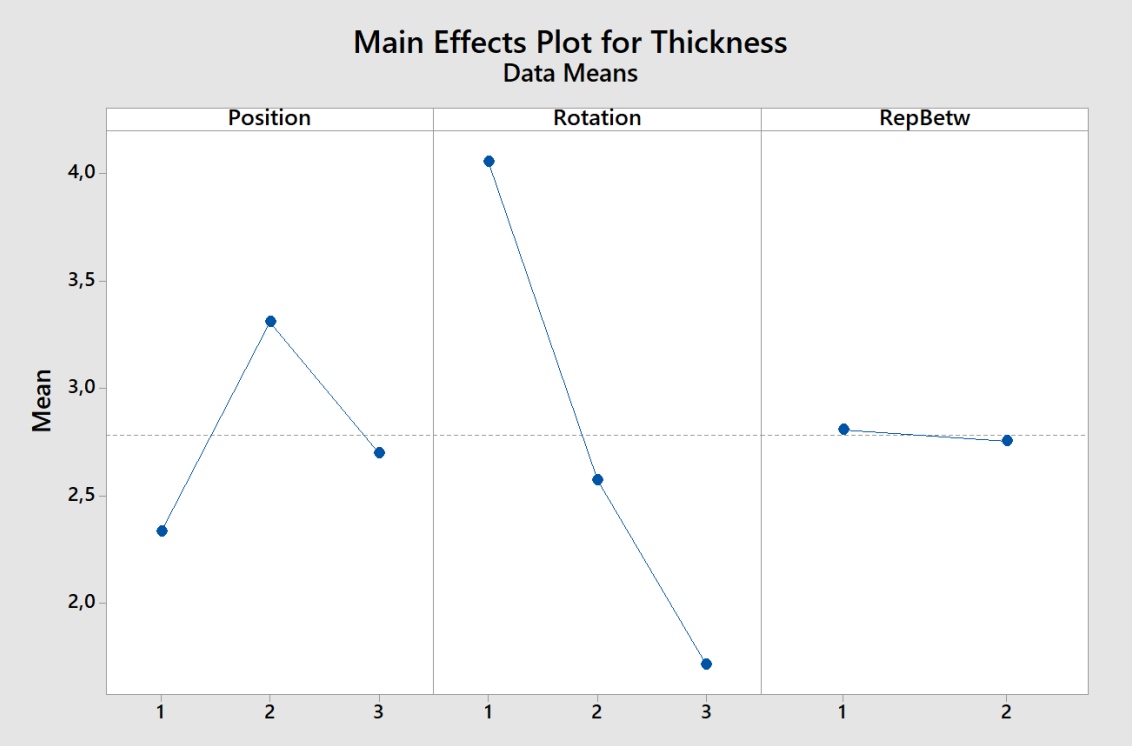

Figure 7.1

Interaction between position and rotation seems slightly significant, as the one between rotation modes and “between” variability, even if it is not

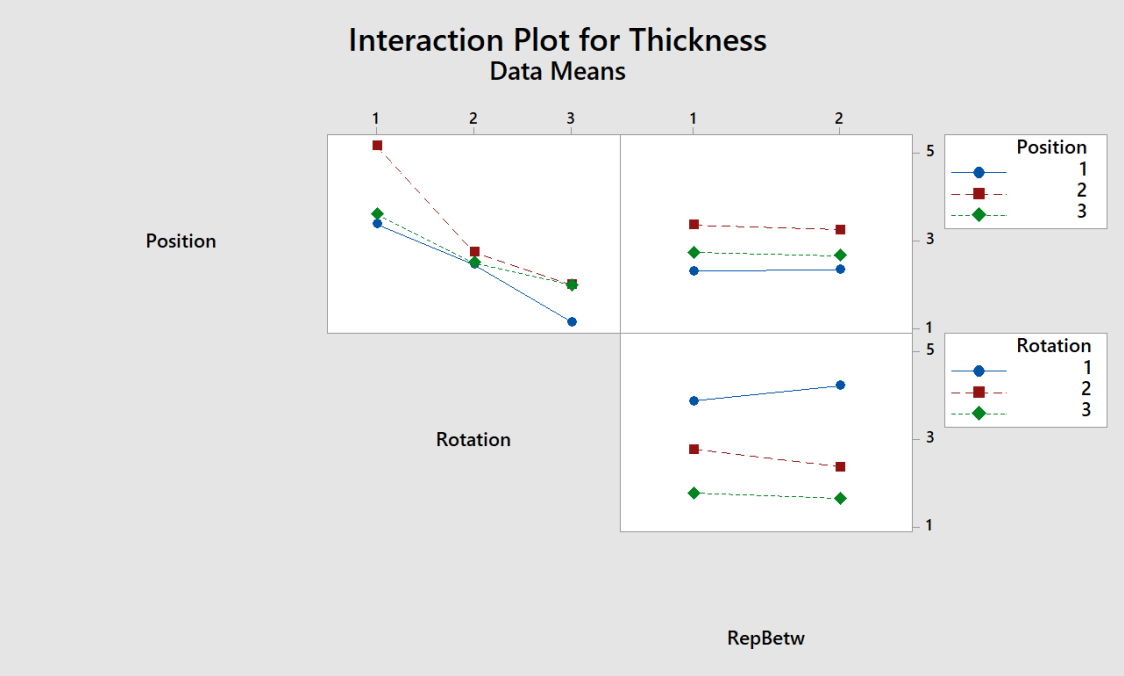

Figure 7.2

ANOVA table of the general linear model is then displayed.
Interaction of repetition between batches and the other two factors has been assumed as not relevant. This hypothesis will be checked during ANOVA analysis.

General Linear Model: Thickness versus Position; Rotation; RepBetw

Method

Factor coding (-1; 0; +1)

Factor Information

Factor	Type	Levels	Values
Position	Fixed	3	1; 2; 3
Rotation	Fixed	3	1; 2; 3
RepBetw	Fixed	2	1; 2

Analysis of Variance

Source	DF	Adj SS	Adj MS	F-Value	P-Value
Position	2	8,7609	4,3805	61,43	0,000
Rotation	2	50,5183	25,2592	354,24	0,000
RepBetw	1	0,0395	0,0395	0,55	0,461
Position*Rotation	4	5,8206	1,4552	20,41	0,000
Error	44	3,1375	0,0713		
Lack-of-Fit	8	1,8413	0,2302	6,39	0,000
Pure Error	36	1,2962	0,0360		
Total	53	68,2768			

Model Summary

S	R-sq	R-sq(adj)	R-sq(pred)
0,267032	95,40%	94,46%	93,08%

Coefficients

Term	Coef	SE Coef	T-Value	P-Value	VIF
Constant	2,7819	0,0363	76,55	0,000	
Position					
1	-0,4480	0,0514	-8,72	0,000	1,33
2	0,5287	0,0514	10,29	0,000	1,33
Rotation					
1	1,2748	0,0514	24,81	0,000	1,33
2	-0,2080	0,0514	-4,05	0,000	1,33
RepBetw					
1	0,0270	0,0363	0,74	0,461	1,00
Position*Rotation					
1 1	-0,2237	0,0727	-3,08	0,004	1,78
1 2	0,3424	0,0727	4,71	0,000	1,78
2 1	0,5896	0,0727	8,11	0,000	1,78
2 2	-0,3526	0,0727	-4,85	0,000	1,78

Regression Equation

Thickness = 2,7819 - 0,4480 Position_1 + 0,5287 Position_2 - 0,0807 Position_3
+ 1,2748 Rotation_1 - 0,2080 Rotation_2 - 1,0669 Rotation_3 + 0,0270 RepBetw_1
- 0,0270 RepBetw_2 - 0,2237 Position*Rotation_1 1 + 0,3424 Position*Rotation_1 2
- 0,1187 Position*Rotation_1 3 + 0,5896 Position*Rotation_2 1
- 0,3526 Position*Rotation_2 2 - 0,2370 Position*Rotation_2 3
- 0,3659 Position*Rotation_3 1 + 0,0102 Position*Rotation_3 2
+ 0,3557 Position*Rotation_3 3

Position, rotation and position*rotation affects layer thickness. Lack of fit, mainly composed by interaction of "repetition between" and rotation.
Even if p-value seems that this interaction affects the response, F-value is by far lower than the others significant main effects and interactions, therefore it can be assumed as negligible.
Let's check ANOVA hypothesis.
Normality assumption cannot be refused.

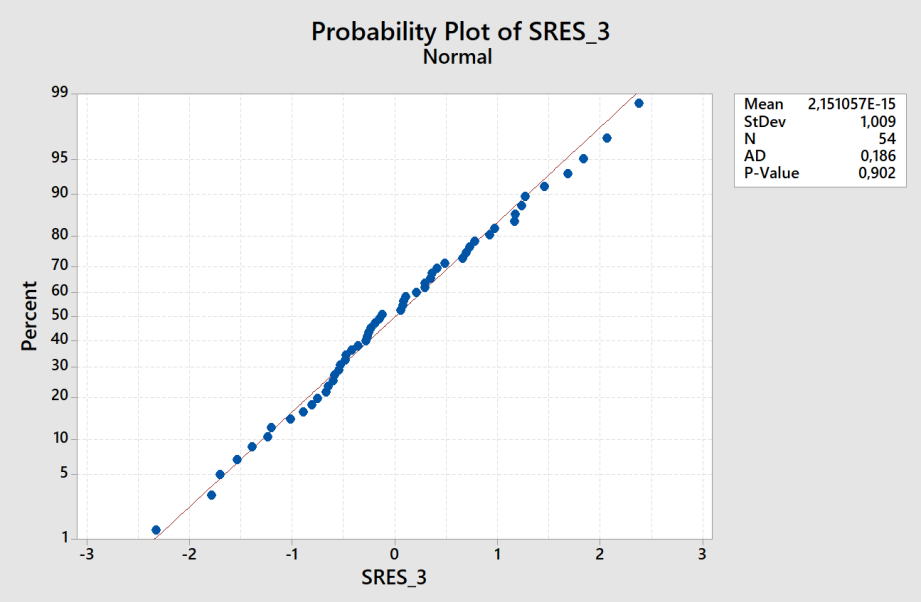

Figure 7.3

No outliers are detected, all standardized residuals belong to (-3, +3) interval.

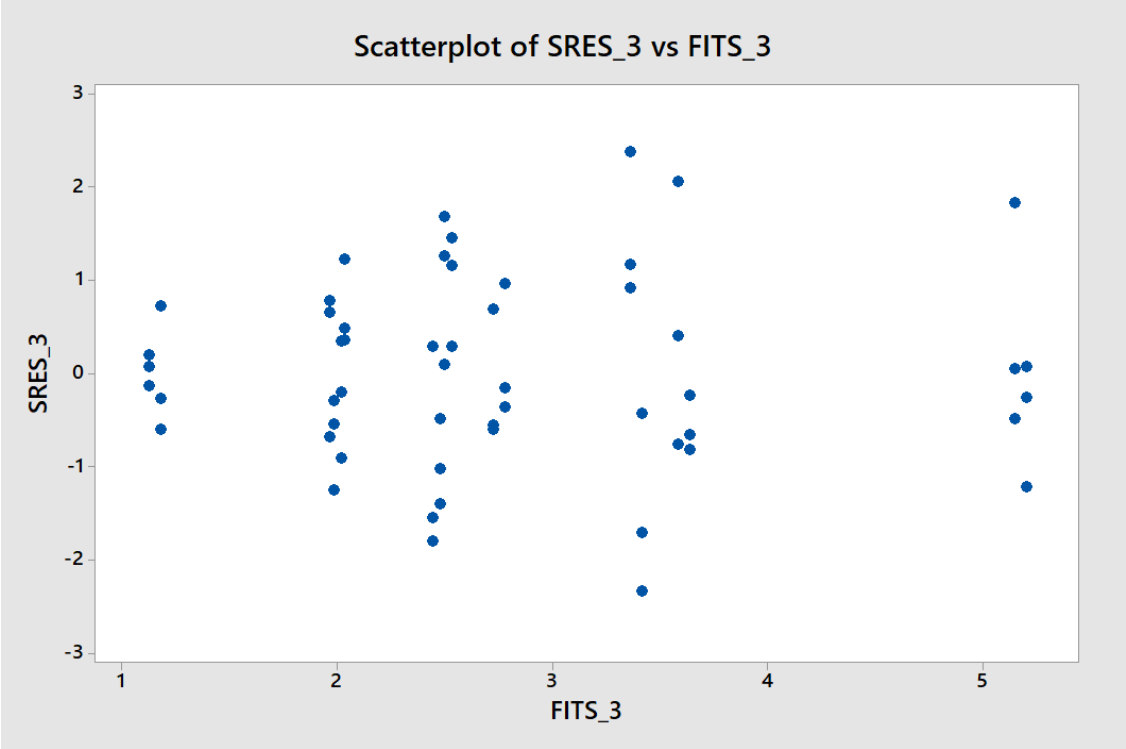

Figure 7.4

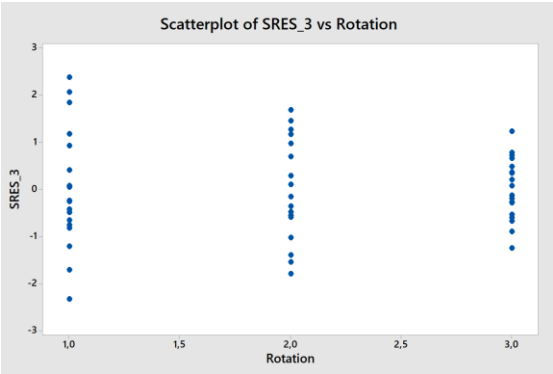

(a)

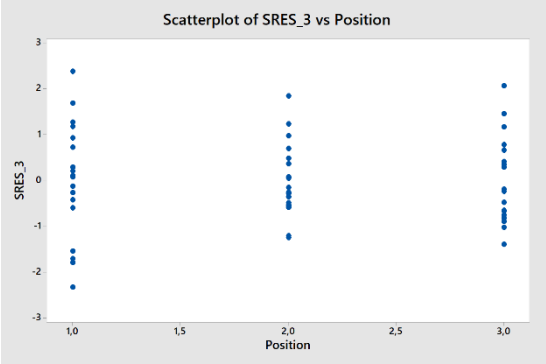

(b)

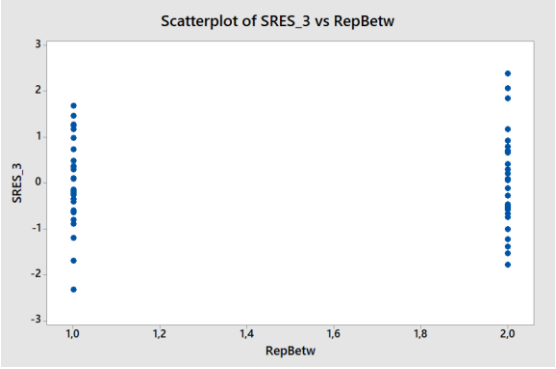

(c)

Figure 7.5 (a), (b) and (c)

Autocorrelation of sorted standardized residuals is not significant.

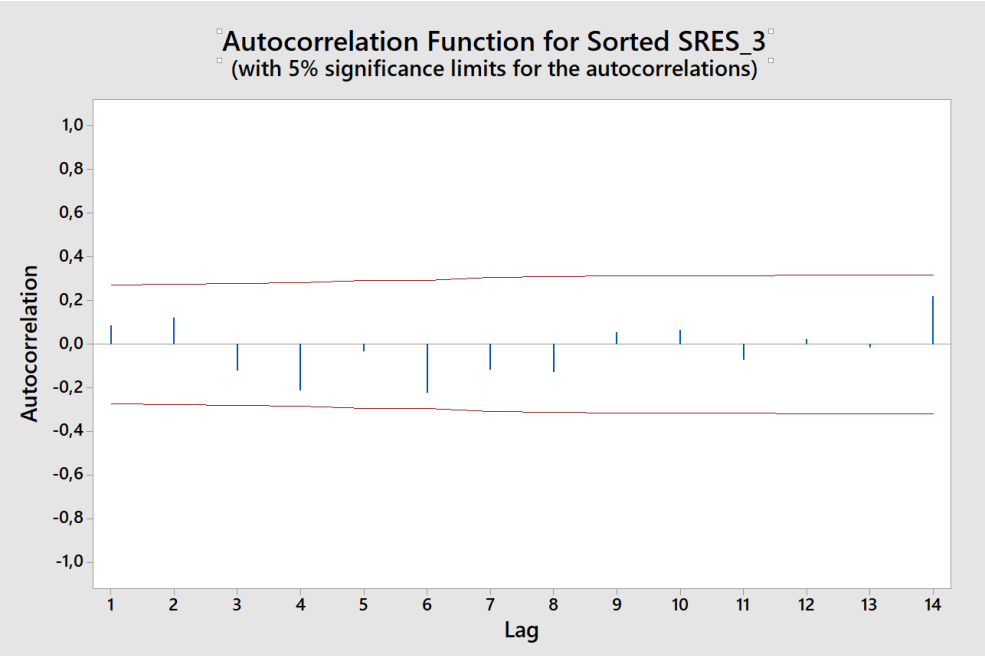

Figure 7.6

In conclusion, central measurement analysis shows no relevant variations between batches. Position, rotation and position*rotation are significant.
The analysis shows a reduction in terms of layer thickness when number of rotation modes is increased. With 2-fold and 3-fold rotation, sample faces are less exposed directly in line of sight to coating material source, therefore less amount of material reaches the surface.
Position effect is significant too: samples placed at middle height in the coating chamber have higher thickness values with respect to samples coated at bound levels.
This result can be explained as middle height samples are on average closer to target sources than specimens placed at bounds.

7.2 Multiple measurement points plans

Previous analyses are suitable to evaluate factors which affect variation of layer thickness between different samples, but the variability of the response within the sample has not been investigated yet.
Therefore, a new measurement plan of the same samples of the single measurement study has been set up.
Samples measuring plan is shown in Figure 7.7 (red dots).
Measurements have been taken in 4 different angular position, at 90° one another.
On the face, 4 radial position have been inspected, starting at 0.2 mm from the edge. Other measurements are distant 2 mm one another. On the lateral surface, in the correspondent angular position of face measurement, 3 axial position have been inspected, starting at 0,2 mm from the face.
Two different analysis have been performed, one for the face and one for the lateral surface.

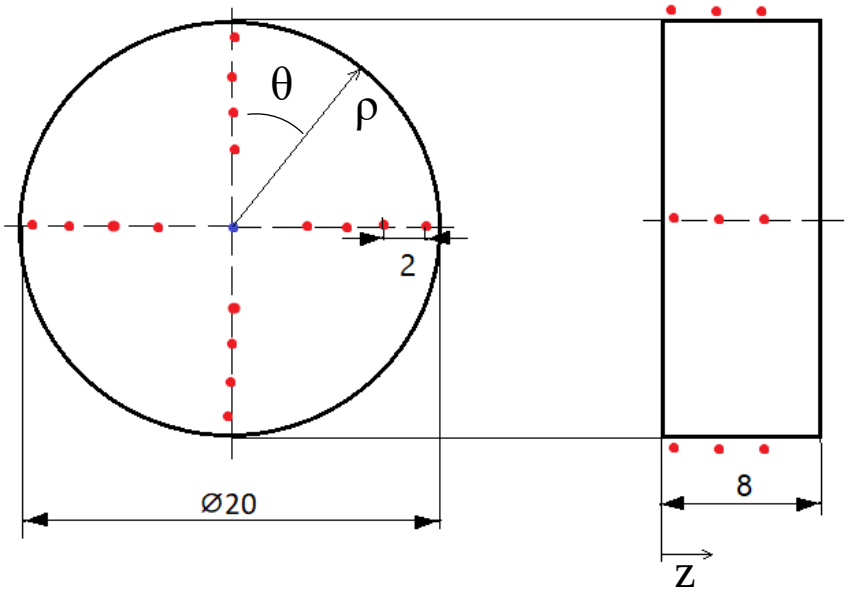

Figure 7.7: Measurement plan of specimens.

7.2.1 Thickness distribution on circular face

Analysis of thickness distribution on circular faces takes into account 4 factors, the two previously detected as relevant (axial position in the chamber, and rotation modes) and radial and angular position on the face ("Rho" and "Theta" factors).
Looking at the main effect plot, angular position seems not significant.

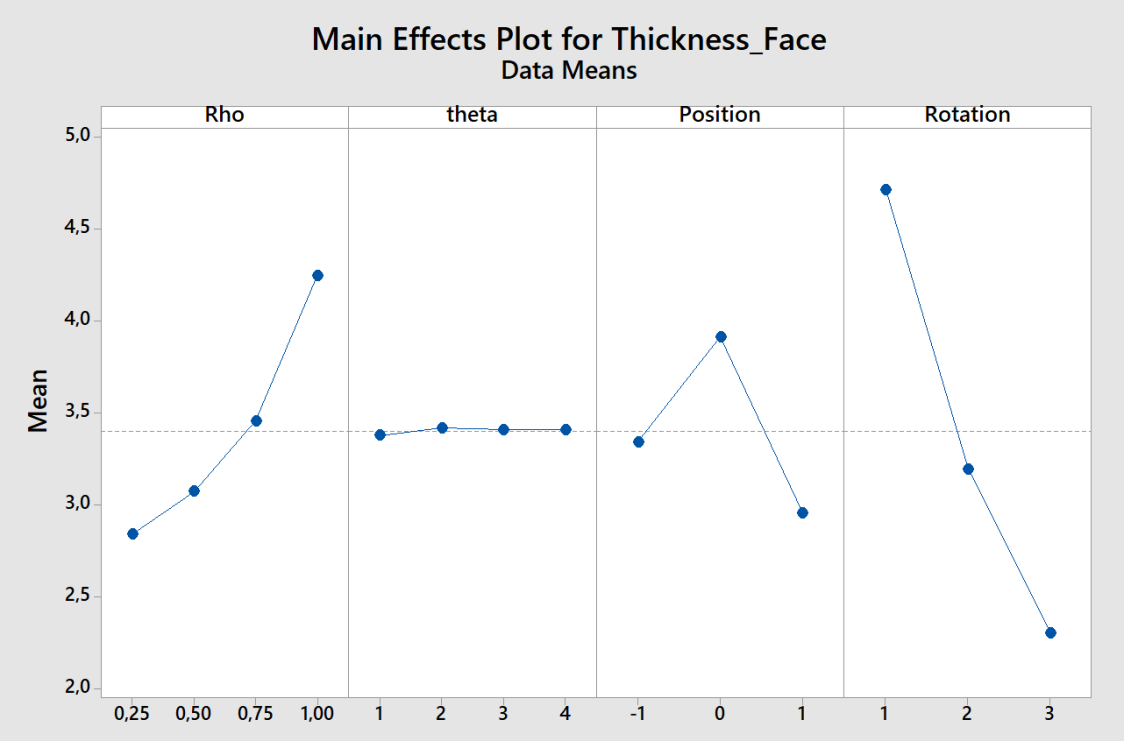

Figure 7.8

Some interactions seem to be significant, i.e. position*rotation, and position*rotation.

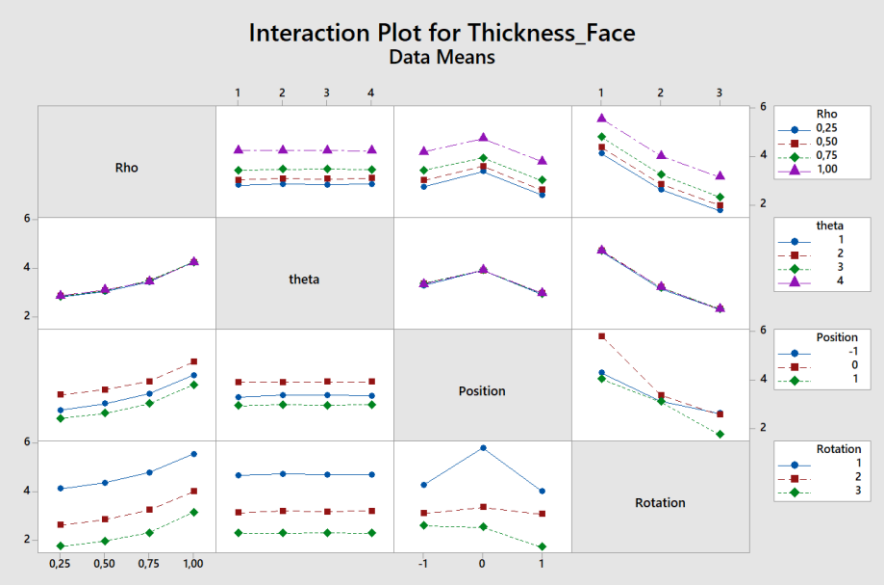

Figure 7.9

ANOVA table is then displayed.

General Linear Model: Thickness_Face versus Rho; theta; ... n; Rotation

Method

Factor coding (-1; 0; +1)

Factor Information

Factor	Type	Levels	Values
Rho	Fixed	4	0,25; 0,50; 0,75; 1,00
theta	Fixed	4	1; 2; 3; 4
Position	Fixed	3	-1; 0; 1
Rotation	Fixed	3	1; 2; 3

Analysis of Variance

Source	DF	Adj SS	Adj MS	F-Value	P-Value
Rho	3	245,13	81,712	1046,35	0,000
theta	3	0,20	0,066	0,84	0,470
Position	2	134,16	67,081	858,99	0,000
Rotation	2	854,70	427,349	5472,36	0,000
Rho*theta	9	0,18	0,020	0,26	0,985
Rho*Position	6	0,26	0,044	0,56	0,762
Rho*Rotation	6	0,33	0,056	0,71	0,639
theta*Position	6	0,22	0,036	0,47	0,833
theta*Rotation	6	0,10	0,017	0,22	0,970
Position*Rotation	4	94,73	23,684	303,28	0,000
Rho*theta*Position	18	0,35	0,019	0,25	0,999
Rho*theta*Rotation	18	0,30	0,017	0,21	1,000
Rho*Position*Rotation	12	0,26	0,021	0,27	0,993
theta*Position*Rotation	12	0,20	0,017	0,22	0,998
Rho*theta*Position*Rotation	36	0,41	0,011	0,14	1,000
Error	720	56,23	0,078		
Total	863	1387,76			

Model Summary

S	R-sq	R-sq(adj)	R-sq(pred)
0,279450	95,95%	95,14%	94,17%

In addition to the already tested effects of position, rotation, and their influence, radial position seems to have an effect on the response variable, with higher coating thickness values on the edges. Factor theta (angular position) does not appear as significant. This result suggests an axisymmetric distribution of coating thickness on the face. Before accepting the results, ANOVA hypothesis are checked.

Normality hypothesis cannot be refused.

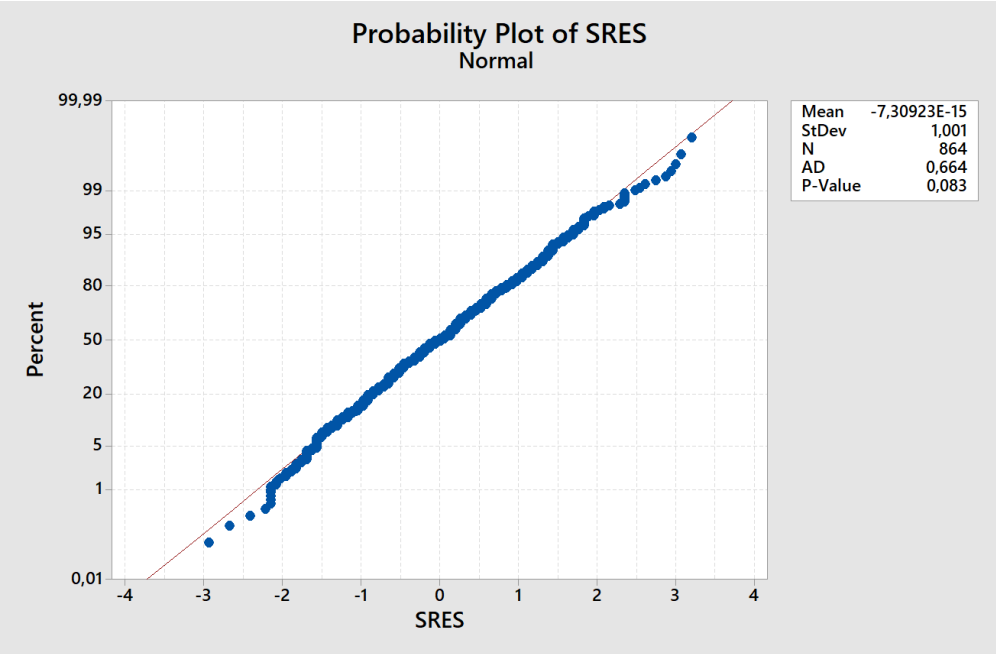

Figure 7.10

Only two standardized residuals exceed the interval (-3, +3), no obvious distributions are noticed.

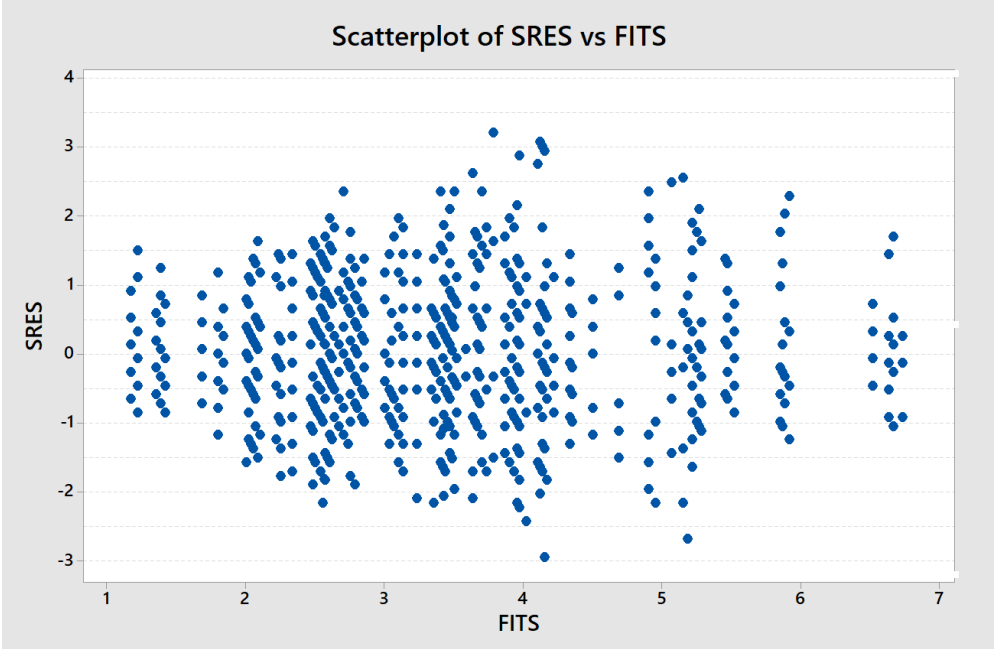

Figure 7.11

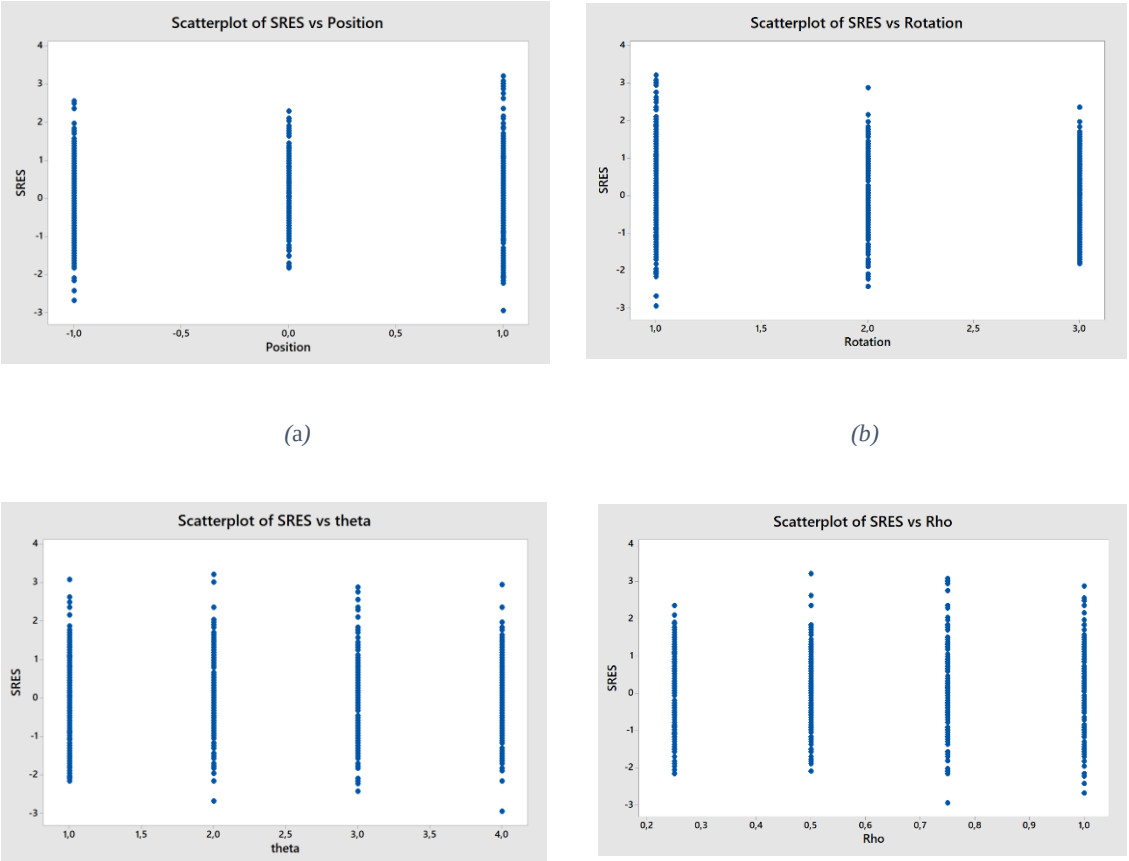

(a) *(b)*

(c) *(d)*

Figure 7.12 (a) (b) (c) and (d)

In conclusion, ANOVA hypothesis are verified. Thickness distribution on the face can be assumed axisymmetric since no influence of factor theta is statistically significant.
On the other hand, radial position (factor rho) is significant. Coating layer is thicker close to the face edges. The result could be explained by the edge concentration effect of electromagnetic field in conductors.
In a cathodic arc deposition process, since depositing material is ionized, it will be more likely attracted by areas where electromagnetic field is more intense, like edges.

Once defined factors that affect layer thickness distribution within a single piece, regression model will be developed to study in deep the deposition along radial direction.

7.2.1.1 Regression model for circular face

Regression model includes second and third order components for position and rho factors. For rotation factor, since it is a categorical predictor, not a continuous one, only first order terms plus its interactions have been included.
Third order term "Position^3" cannot be estimated due to sampling in only 3 positions. (Top, middle and bottom of the chamber).

Regression Analysis: Thickness_Face versus Position; Rho; Rotation

The following terms cannot be estimated and were removed:
Position*Position*Position

Method

Categorical predictor coding (1; 0)

Analysis of Variance

Source	DF	Adj SS	Adj MS	F-Value	P-Value
Regression	20	1329,16	66,4581	956,00	0,000
Position	1	0,04	0,0384	0,55	0,457
Rho	1	0,35	0,3519	5,06	0,025
Rotation	2	44,89	22,4442	322,86	0,000
Position*Position	1	69,50	69,5046	999,83	0,000
Rho*Rho	1	0,25	0,2486	3,58	0,059
Position*Rho	1	0,05	0,0514	0,74	0,390
Position*Rotation	2	3,55	1,7740	25,52	0,000
Rho*Rotation	2	0,18	0,0877	1,26	0,284
Rho*Rho*Rho	1	0,70	0,7010	10,08	0,002
Position*Position*Rho	1	0,09	0,0938	1,35	0,246
Position*Rho*Rho	1	0,03	0,0299	0,43	0,512
Position*Position*Rotation	2	75,90	37,9499	545,91	0,000
Position*Rho*Rotation	2	0,02	0,0079	0,11	0,892
Rho*Rho*Rotation	2	0,15	0,0740	1,06	0,345
Error	843	58,60	0,0695		
Lack-of-Fit	15	0,42	0,0281	0,40	0,979
Pure Error	828	58,18	0,0703		
Total	863	1387,76			

Model Summary

S	R-sq	R-sq(adj)	R-sq(pred)
0,263660	95,78%	95,68%	95,56%

Coefficients

Term	Coef	SE Coef	T-Value	P-Value	VIF
Constant	4,856	0,169	28,77	0,000	
Position	-0,0536	0,0720	-0,74	0,457	43,00
Rho	2,134	0,948	2,25	0,025	873,44
Rotation					
2	-2,376	0,126	-18,83	0,000	44,00
3	-3,054	0,126	-24,19	0,000	44,00
Position*Position	-1,7018	0,0538	-31,62	0,000	8,00
Rho*Rho	-3,07	1,62	-1,89	0,059	4128,00
Position*Rho	-0,198	0,230	-0,86	0,390	205,50
Position*Rotation					
2	0,1083	0,0659	1,64	0,101	12,00
3	-0,3427	0,0659	-5,20	0,000	12,00
Rho*Rotation					
2	-0,192	0,446	-0,43	0,667	279,50
3	-0,687	0,446	-1,54	0,124	279,50
Rho*Rho*Rho	2,718	0,856	3,18	0,002	1327,78
Position*Position*Rho	0,0791	0,0681	1,16	0,246	8,00
Position*Rho*Rho	0,115	0,176	0,66	0,512	88,50
Position*Position*Rotation					
2	1,3914	0,0466	29,85	0,000	4,67
3	1,2674	0,0466	27,19	0,000	4,67
Position*Rho*Rotation					
2	-0,0004	0,0963	-0,00	0,997	12,00
3	0,0396	0,0963	0,41	0,681	12,00
Rho*Rho*Rotation					
2	0,108	0,352	0,31	0,758	139,50
3	0,488	0,352	1,39	0,165	139,50

Regression Equation

Rotation			
1	Thickness_Face	=	4,856 - 0,0536 Position + 2,134 Rho - 1,7018 Position*Position - 3,07 Rho*Rho - 0,198 Position*Rho + 2,718 Rho*Rho*Rho + 0,0791 Position*Position*Rho + 0,115 Position*Rho*Rho
2	Thickness_Face	=	2,479 + 0,0548 Position + 1,941 Rho - 0,3104 Position*Position - 2,96 Rho*Rho - 0,198 Position*Rho + 2,718 Rho*Rho*Rho + 0,0791 Position*Position*Rho + 0,115 Position*Rho*Rho
3	Thickness_Face	=	1,802 - 0,3963 Position + 1,447 Rho - 0,4343 Position*Position - 2,58 Rho*Rho - 0,158 Position*Rho + 2,718 Rho*Rho*Rho + 0,0791 Position*Position*Rho + 0,115 Position*Rho*Rho

Model seems to correctly predict the response variable. Three regression equation have been displayed, one for each rotation mode.

The factors that affect thickness on the face are rho, rotation, position^2, position*rotation, rho^3, position^2*rotation. Even Rho^2 seems to be slightly significant.
Adjusted R-squared parameter is very high, therefore the model seems to correctly predict the response variable
Before going one with the analysis, model assumptions must be checked.

Normality hypothesis cannot be refused.

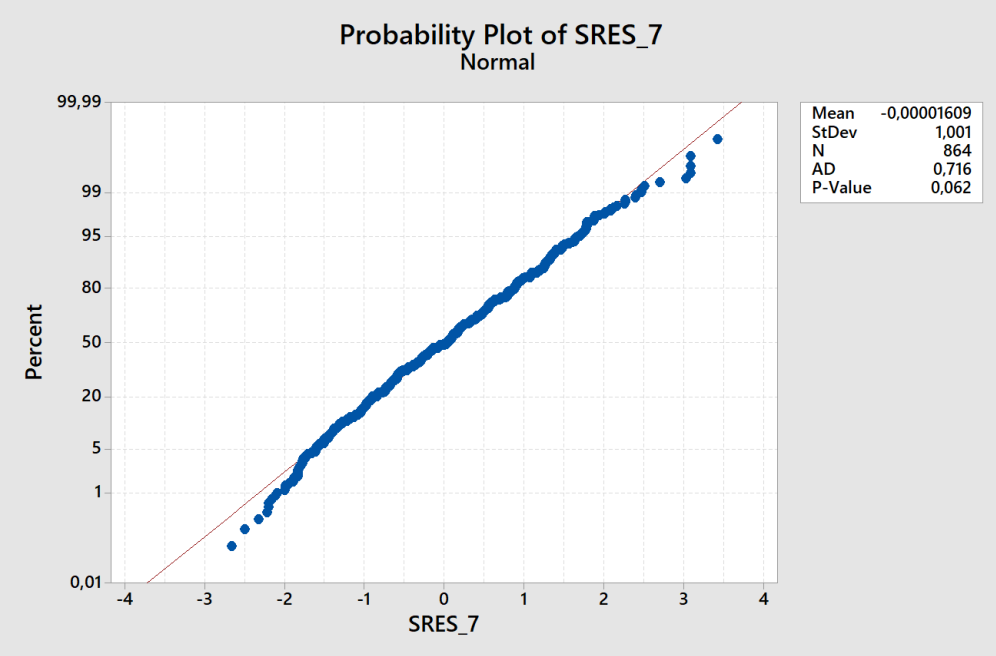

Figure 7.13

Only two values are not included in (-3, +3) interval for std. residuals, no obvious distributions are detected.

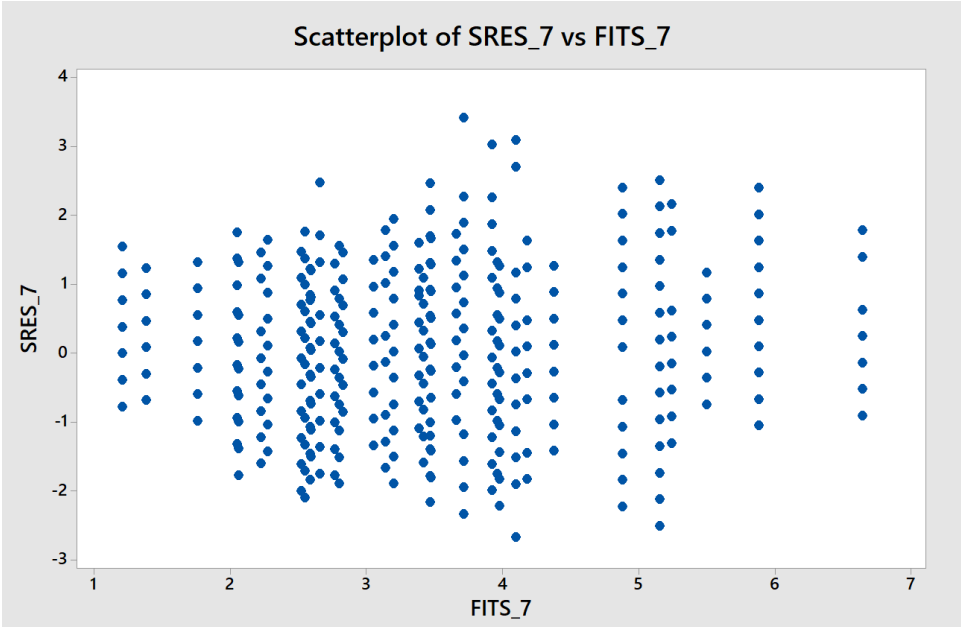

Figure 7.14

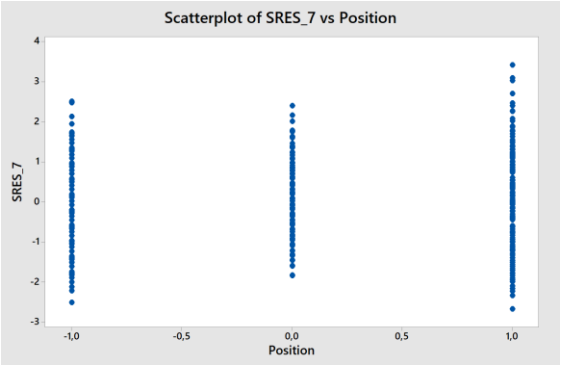

(a)

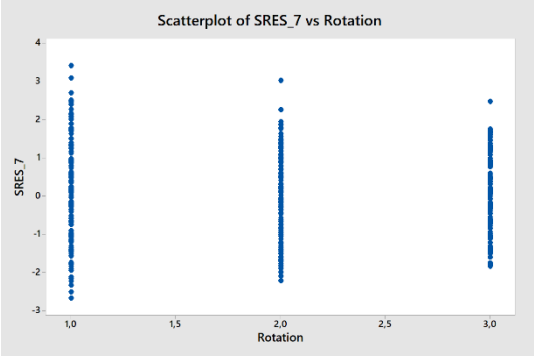

(b)

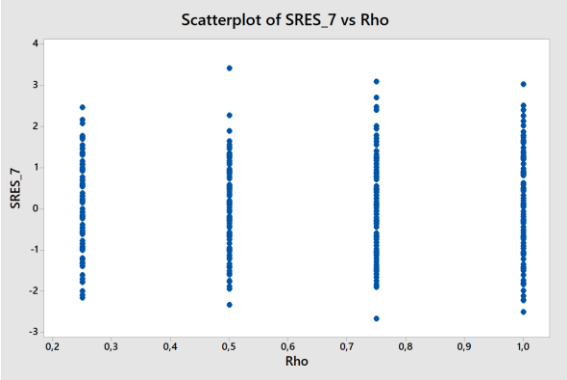

(c)

Figure 7.15 (a), (b) and (c)

Even if the model is significant, due to the presence of several not significant factors, it has been reduced, maintaining in any case the hierarchic terms.

Regression Analysis: Thickness_Face versus Position; Rho; Rotation

The following terms cannot be estimated and were removed:
Position*Position*Position

Method

Categorical predictor coding (1; 0)

Analysis of Variance

Source	DF	Adj SS	Adj MS	F-Value	P-Value
Regression	11	1328,73	120,794	1743,28	0,000
Position	1	2,91	2,913	42,04	0,000
Rho	1	0,30	0,300	4,33	0,038
Rotation	2	551,20	275,602	3977,45	0,000
Position*Position	1	174,74	174,735	2521,76	0,000
Rho*Rho	1	0,22	0,221	3,19	0,075
Position*Rotation	2	18,83	9,417	135,91	0,000
Rho*Rho*Rho	1	0,70	0,701	10,12	0,002
Position*Position*Rotation	2	75,90	37,950	547,69	0,000
Error	852	59,04	0,069		
Lack-of-Fit	24	0,85	0,036	0,51	0,977
Pure Error	828	58,18	0,070		
Total	863	1387,76			

Model Summary

S	R-sq	R-sq(adj)	R-sq(pred)
0,263232	95,75%	95,69%	95,63%

Coefficients

Term	Coef	SE Coef	T-Value	P-Value	VIF
Constant	4,913	0,151	32,55	0,000	
Position	-0,1232	0,0190	-6,48	0,000	3,00
Rho	1,893	0,910	2,08	0,038	806,94
Rotation					
2	-2,4458	0,0380	-64,37	0,000	4,00
3	-3,2542	0,0380	-85,65	0,000	4,00
Position*Position	-1,6523	0,0329	-50,22	0,000	3,00
Rho*Rho	-2,87	1,61	-1,79	0,075	4063,50
Position*Rotation					
2	0,1081	0,0269	4,02	0,000	2,00
3	-0,3180	0,0269	-11,84	0,000	2,00
Rho*Rho*Rho	2,718	0,854	3,18	0,002	1327,78
Position*Position*Rotation					
2	1,3914	0,0465	29,90	0,000	4,67
3	1,2674	0,0465	27,24	0,000	4,67

Regression Equation

Rotation			
1	Thickness_Face	=	4,913 - 0,1232 Position + 1,893 Rho - 1,6523 Position*Position - 2,87 Rho*Rho + 2,718 Rho*Rho*Rho
2	Thickness_Face	=	2,467 - 0,0151 Position + 1,893 Rho - 0,2609 Position*Position - 2,87 Rho*Rho + 2,718 Rho*Rho*Rho
3	Thickness_Face	=	1,658 - 0,4411 Position + 1,893 Rho - 0,3849 Position*Position - 2,87 Rho*Rho + 2,718 Rho*Rho*Rho

R-squared parameters maintain high values, lack of fit is not significant.
All model terms seem to have an influence on the output. Before going on with the analysis, model hypothesis need to be checked.
Equality of variance cannot be refused.

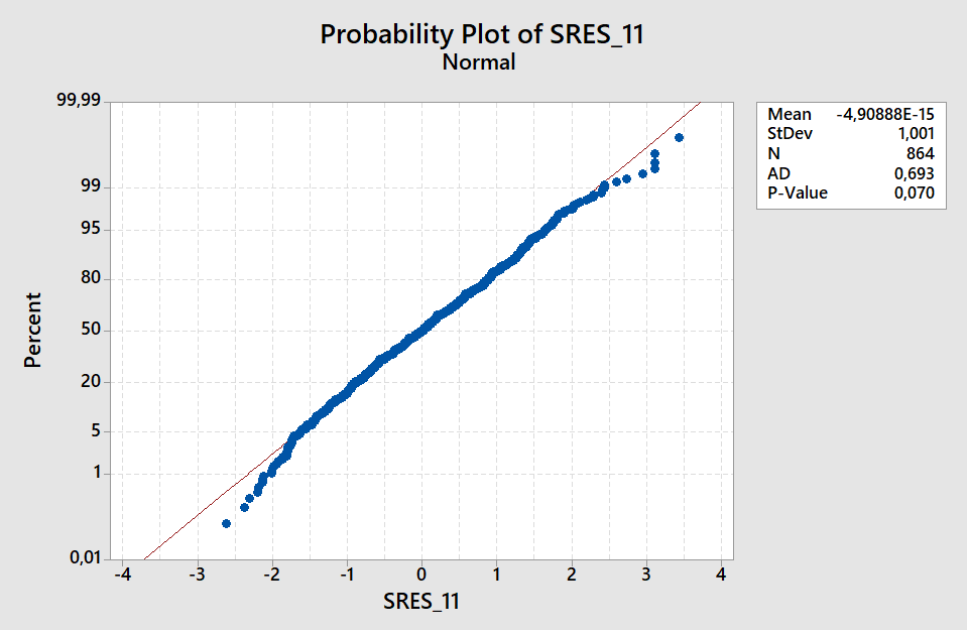

Figure 7.16

As in the previous model,only two values are not included in (-3, +3) interval for std. residuals, no obvious distributions are detected.

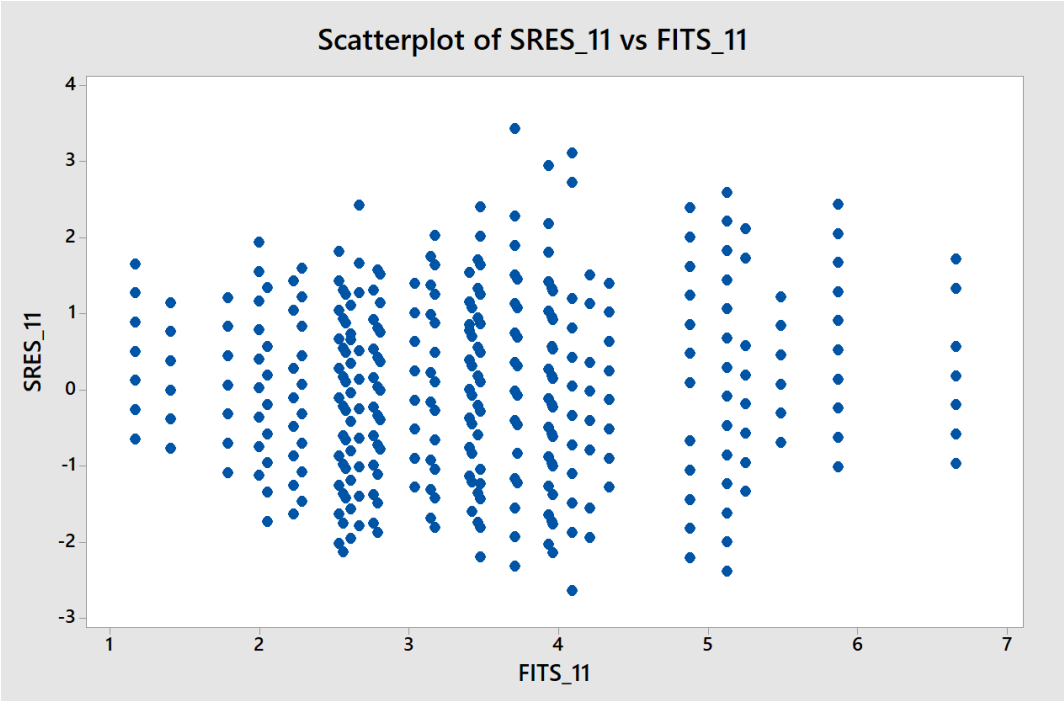

Figure 7.17

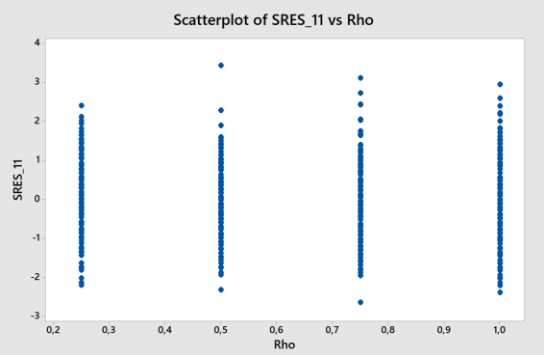

(a)

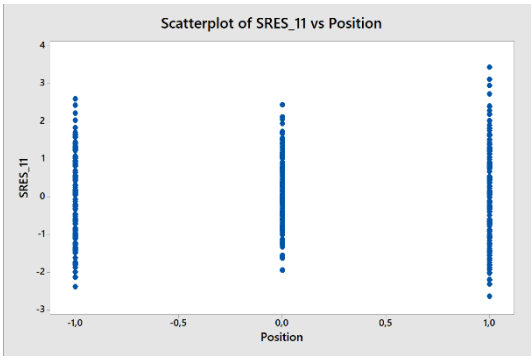

(b)

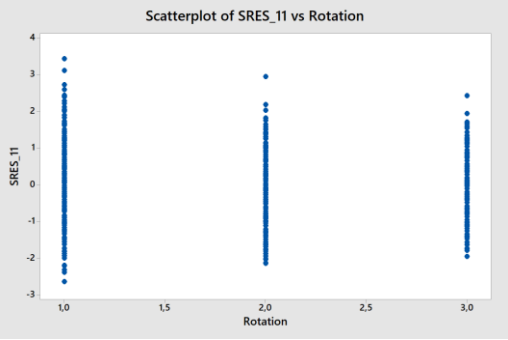

(c)

Figure 7.18 (a), (b) and (c)

In conclusion, model hypotheses are respected. In order to evaluate whether the regression model can be applied to the process, three predictive runs have been launched. For continuous predictors, like axial position in the chamber and radial position within the face of the specimens, new values in the correspondent range, not previously evaluated, have been explored.

Run	**1**	**2**	**3**
Position	0,5	-0,5	-1
Rho	1	0,75	0,25
Rotation	2	1	3
Thickness measured	3,9	5,4	2,1

Table 7.1: Prediction runs for regression model of coating thickness on the specimens' face

All runs are within the limits of prediction intervals:

Prediction for Thickness_Face

Regression Equation

Thickness_Face = 4,913 - 0,1232 Position + 1,893 Rho + 0,000000 Rotation_1
- 2,4458 Rotation_2 - 3,2542 Rotation_3 - 1,6523 Position*Position
- 2,87 Rho*Rho + 0,000000 Position*Rotation_1 + 0,1081 Position*Rotation_2
- 0,3180 Position*Rotation_3 + 2,718 Rho*Rho*Rho
+ 0,000000 Position*Position*Rotation_1
+ 1,3914 Position*Position*Rotation_2 + 1,2674 Position*Position*Rotation_3

Settings

Variable	Setting
Position	0,5
Rho	1
Rotation	2

Prediction

Fit	SE Fit	95% CI	95% PI
4,13338	0,0275567	(4,07930; 4,18747)	(3,61390; 4,65286)

Settings

Variable	Setting
Position	-0,5
Rho	0,75
Rotation	1

Prediction

Fit	SE Fit	95% CI	95% PI
5,51236	0,0275567	(5,45827; 5,56644)	(4,99287; 6,03184)

Settings

Variable	Setting
Position	-1
Rho	0,25
Rotation	3

Prediction

Fit	SE Fit	95% CI	95% PI
2,05098	0,0310222	(1,99009; 2,11187)	(1,53075; 2,57122)

In conclusion, prediction runs confirm that the model can be accepted to explain and predict layer thickness distribution on circular face.
A similar analysis will be run for lateral surface of specimens.

7.2.2 Lateral surface thickness distribution

Analysis of thickness distribution on lateral faces takes into account 4 factors, axial position and rotation inside the chamber, axial and angular position on the lateral surface ("Zeta" and "Theta" factors).
As for circular face, data have been firstly analysed with a general linear model.
Looking at the main effect plot, angular position seems not significant, while the other three factors seem to have an influence on the response surface.

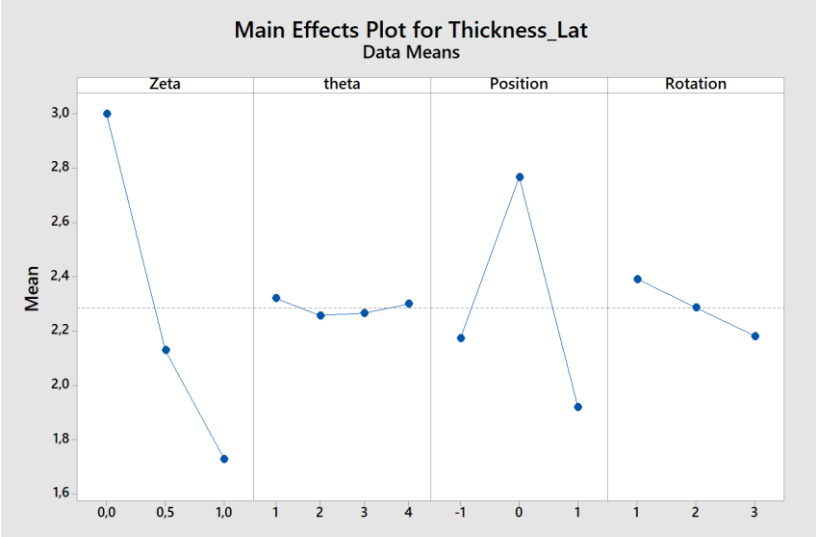

Figure 7.19

Interaction of Zeta*Rotation and Position*Rotation seems to affect the output:

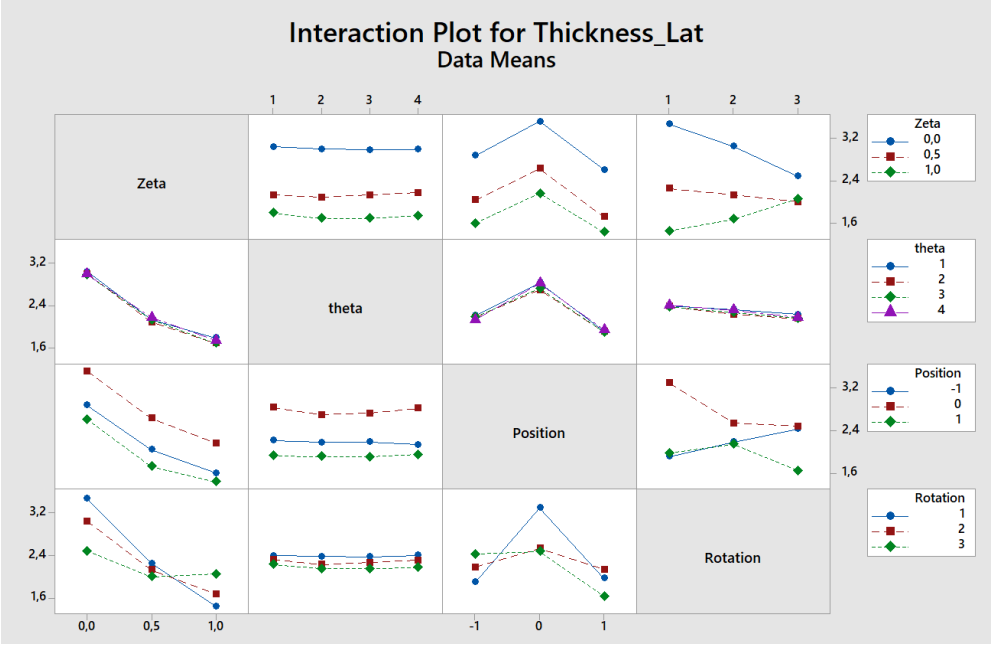

Figure 7.20

Anova table is displayed:

General Linear Model: Thickness_Lat versus Zeta; theta; ... on; Rotation

Method

Factor coding (-1; 0; +1)

Factor Information

Factor	Type	Levels	Values
Zeta	Fixed	3	0,0; 0,5; 1,0
theta	Fixed	4	1; 2; 3; 4
Position	Fixed	3	-1; 0; 1
Rotation	Fixed	3	1; 2; 3

Analysis of Variance

Source	DF	Adj SS	Adj MS	F-Value	P-Value
Zeta	2	182,824	91,4120	739,51	0,000
theta	3	0,412	0,1373	1,11	0,344
Position	2	82,088	41,0440	332,04	0,000
Rotation	2	4,782	2,3909	19,34	0,000
Zeta*theta	6	0,261	0,0434	0,35	0,909
Zeta*Position	4	0,909	0,2272	1,84	0,120
Zeta*Rotation	4	46,168	11,5420	93,37	0,000
theta*Position	6	0,565	0,0941	0,76	0,600
theta*Rotation	6	0,137	0,0228	0,18	0,981
Position*Rotation	4	44,356	11,0889	89,71	0,000
Zeta*theta*Position	12	0,398	0,0332	0,27	0,994
Zeta*theta*Rotation	12	0,311	0,0259	0,21	0,998
Zeta*Position*Rotation	8	1,181	0,1477	1,19	0,300
theta*Position*Rotation	12	0,561	0,0467	0,38	0,971
Zeta*theta*Position*Rotation	24	0,471	0,0196	0,16	1,000
Error	540	66,750	0,1236		
Total	647	432,173			

Model Summary

S	R-sq	R-sq(adj)	R-sq(pred)
0,351585	84,55%	81,49%	77,76%

If model hypothesis are checked, normality and equality of variances are not respected.

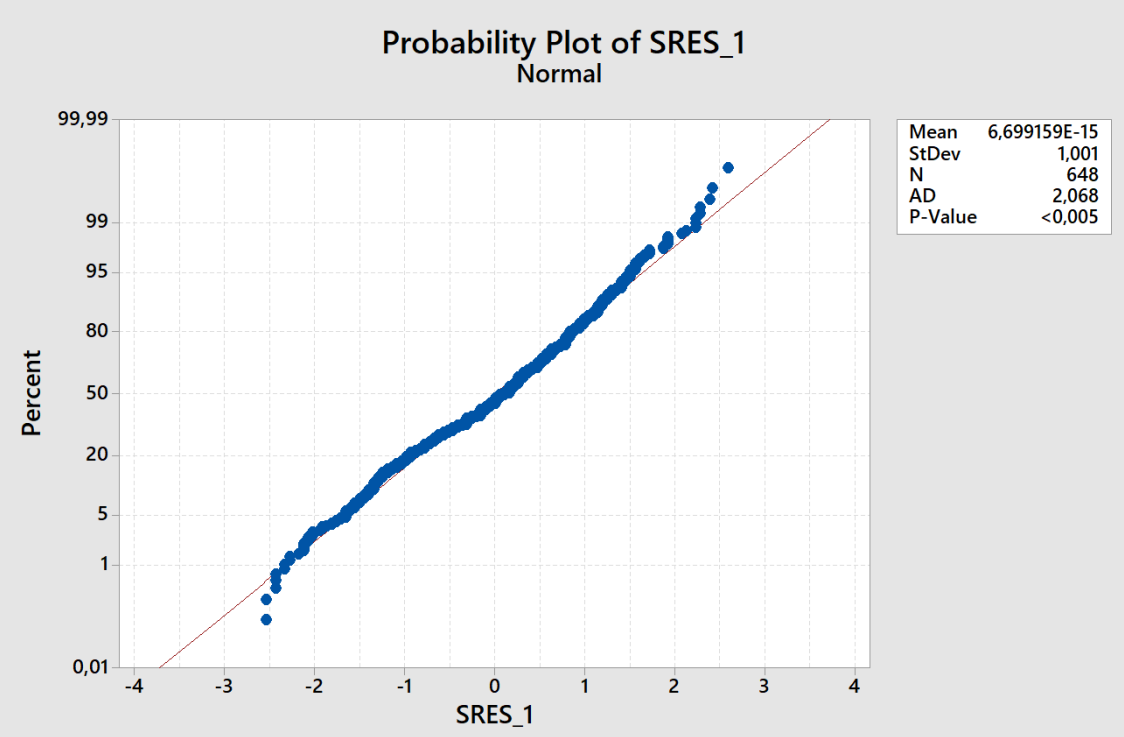

Figure7.21

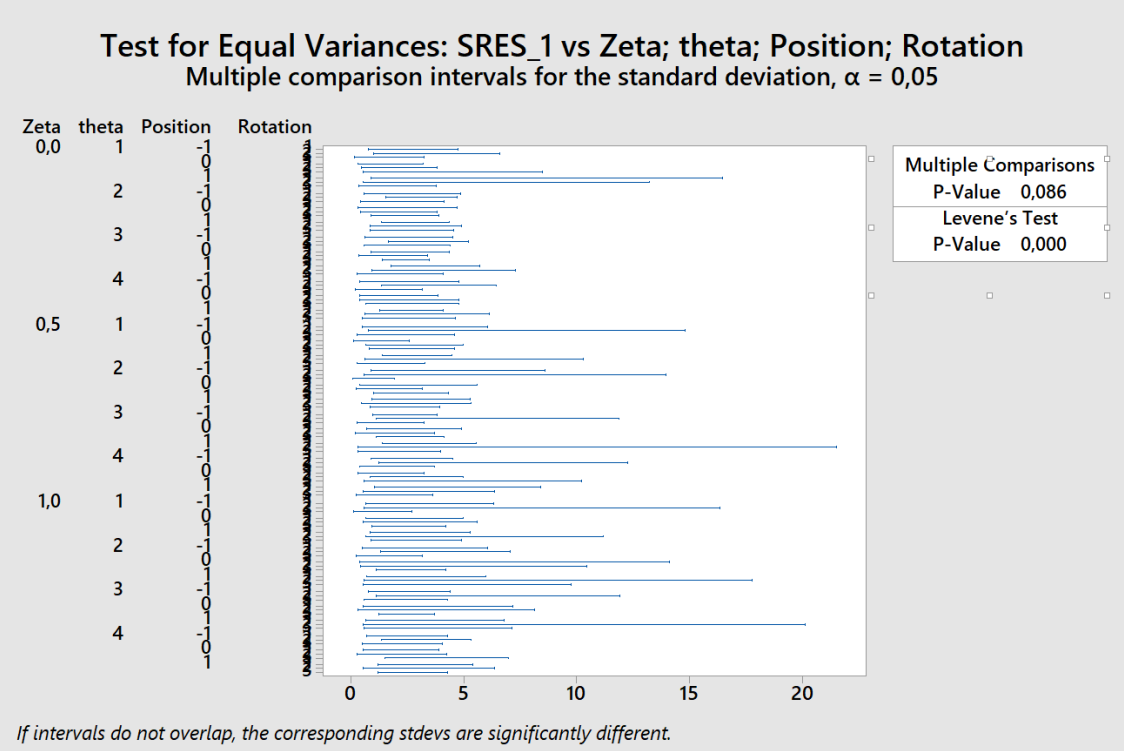

Figure 7.22

No outliers appear, all standardized residuals belong to (-3, +3) interval. No obvious distributions are noticed.

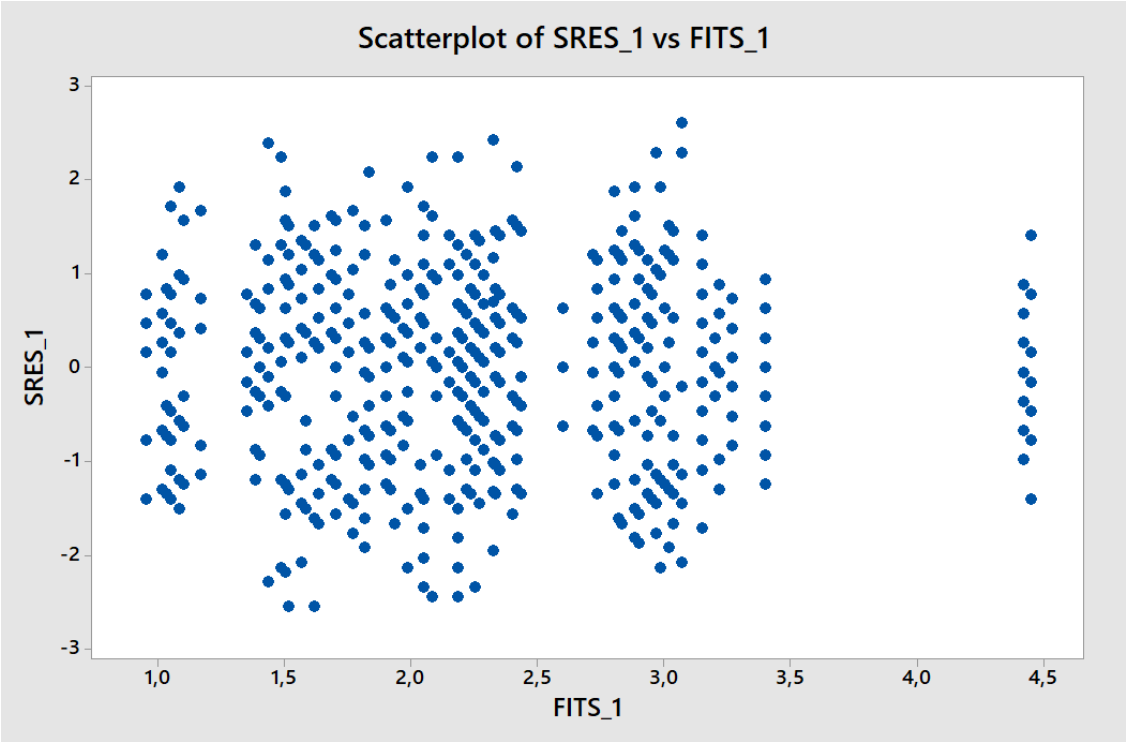

Figure 7.23

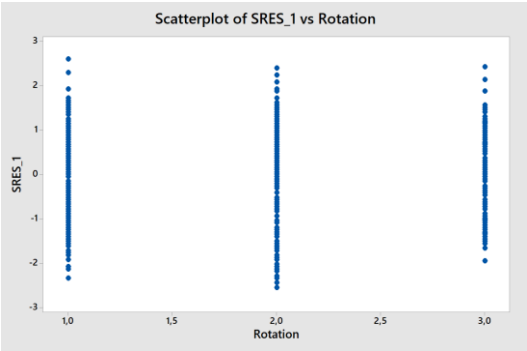

(a)

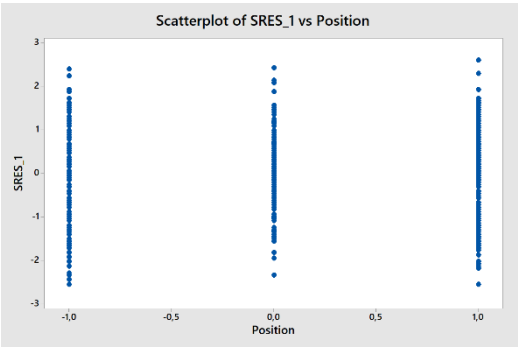

(b)

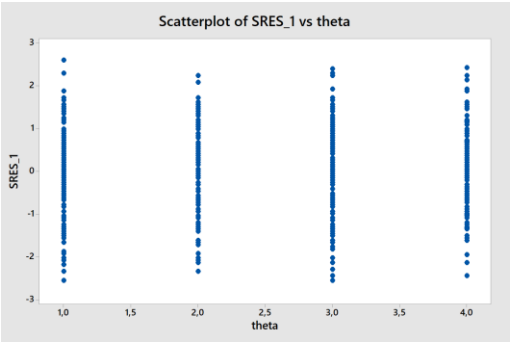

(c)

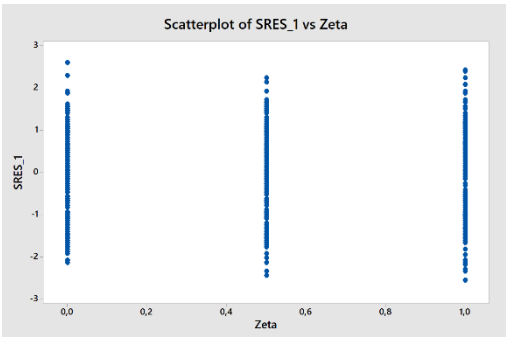

(d)

Figure 7.24 (a) (b) (c) and (d)

Even if factors Zeta, rho, position, interaction position*rotation, zeta*rotation seems to affect thickness distribution, model cannot be accepted because hypothesis are not verified. A regression analysis will be performed.

7.2.2.1 Regression model for thickness distribution on lateral surface

.

Regression model includes second and third order components for position and zeta factors. For rotation factor, since it is a categorical predictor, not a continuous one, only first order terms plus its interactions have been included.

Third order terms “Position^3” and “Zeta^3” cannot be estimated due to sampling in only 3 positions.

Looking at the boxplot in figure 7.25, distribution along axial direction seems to vary on the base of rotation mode, therefore interaction between these factors could be significant.

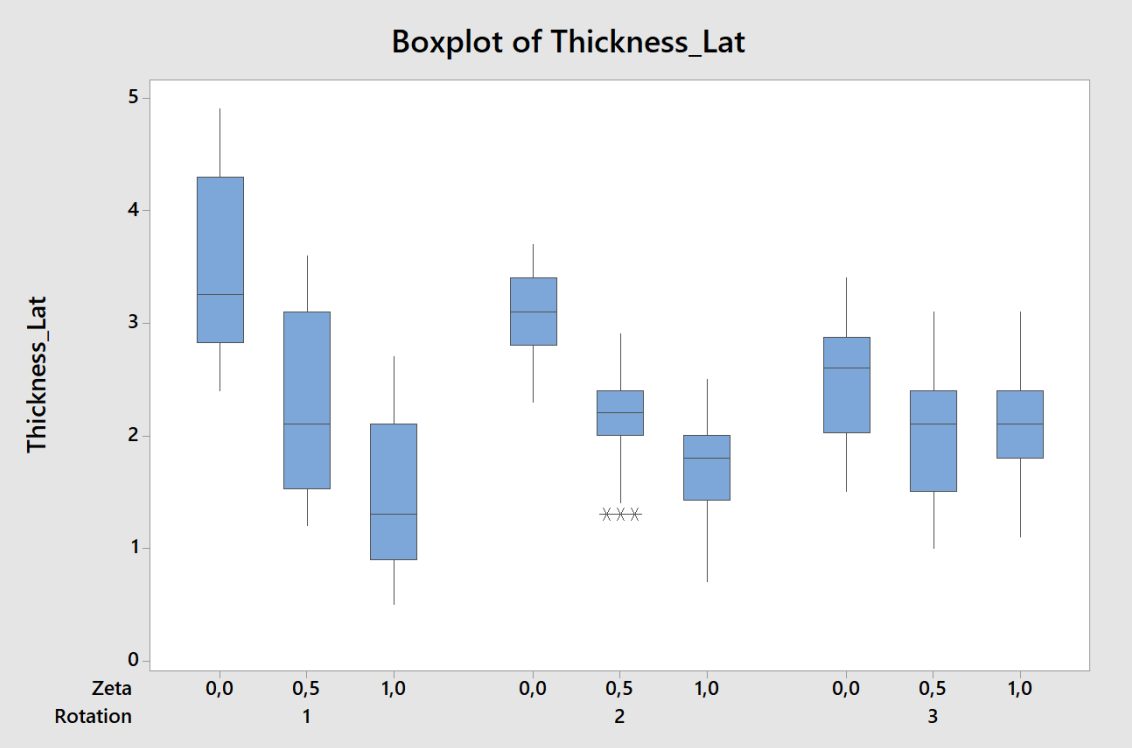

Figure 7.25

Regression analysis is then launched.

Regression Analysis: Thickness_Lat versus Zeta; Position; Rotation

The following terms cannot be estimated and were removed:
Zeta*Zeta*Zeta; Position*Position*Position

Method

Categorical predictor coding	(1; 0)
Box-Cox transformation	
Rounded λ	1
Estimated λ	1,12017
95% CI for λ	(0,988667; 1,25167)

Analysis of Variance

Source	DF	Adj SS	Adj MS	F-Value	P-Value
Regression	14	360,740	25,7672	228,33	0,000
Zeta	1	59,062	59,0624	523,38	0,000
Position	1	0,008	0,0078	0,07	0,792
Rotation	2	64,839	32,4194	287,28	0,000
Zeta*Zeta	1	7,957	7,9571	70,51	0,000
Position*Position	1	64,506	64,5059	571,61	0,000
Zeta*Position	1	0,190	0,1901	1,68	0,195
Zeta*Rotation	2	46,069	23,0347	204,12	0,000
Position*Rotation	2	15,593	7,7967	69,09	0,000
Zeta*Position*Position	1	0,431	0,4311	3,82	0,051
Position*Position*Rotation	2	28,762	14,3811	127,44	0,000
Error	633	71,433	0,1128		
Lack-of-Fit	12	1,567	0,1306	1,16	0,308
Pure Error	621	69,866	0,1125		
Total	647	432,173			

Model Summary

S	R-sq	R-sq(adj)	R-sq(pred)
0,335929	83,47%	83,11%	82,68%

Coefficients

Term	Coef	SE Coef	T-Value	P-Value	VIF
Constant	4,4258	0,0544	81,34	0,000	
Zeta	-3,049	0,133	-22,88	0,000	17,00
Position	0,0090	0,0343	0,26	0,792	4,50
Rotation					
2	-1,0861	0,0686	-15,84	0,000	6,00
3	-1,6115	0,0686	-23,50	0,000	6,00
Zeta*Zeta	0,940	0,112	8,40	0,000	13,00
Position*Position	-1,4198	0,0594	-23,91	0,000	4,50
Zeta*Position	0,0514	0,0396	1,30	0,195	2,50
Zeta*Rotation					
2	0,6500	0,0792	8,21	0,000	4,00
3	1,5910	0,0792	20,09	0,000	4,00
Position*Rotation					
2	-0,0569	0,0396	-1,44	0,151	2,00
3	-0,4285	0,0396	-10,82	0,000	2,00
Zeta*Position*Position	0,1340	0,0686	1,95	0,051	4,50
Position*Position*Rotation					
2	0,9833	0,0686	14,34	0,000	4,67
3	0,9083	0,0686	13,25	0,000	4,67

Regression Equation

Rotation			
1	Thickness_Lat	=	4,4258 - 3,049 Zeta + 0,0090 Position + 0,940 Zeta*Zeta - 1,4198 Position*Position + 0,0514 Zeta*Position + 0,1340 Zeta*Position*Position
2	Thickness_Lat	=	3,3397 - 2,399 Zeta - 0,0479 Position + 0,940 Zeta*Zeta - 0,4365 Position*Position + 0,0514 Zeta*Position + 0,1340 Zeta*Position*Position
3	Thickness_Lat	=	2,8144 - 1,458 Zeta - 0,4194 Position + 0,940 Zeta*Zeta - 0,5115 Position*Position + 0,0514 Zeta*Position + 0,1340 Zeta*Position*Position

Like in the previously illustrated general linear model, normality hypothesis on standardized residuals is not verified, even transforming data with box cox.

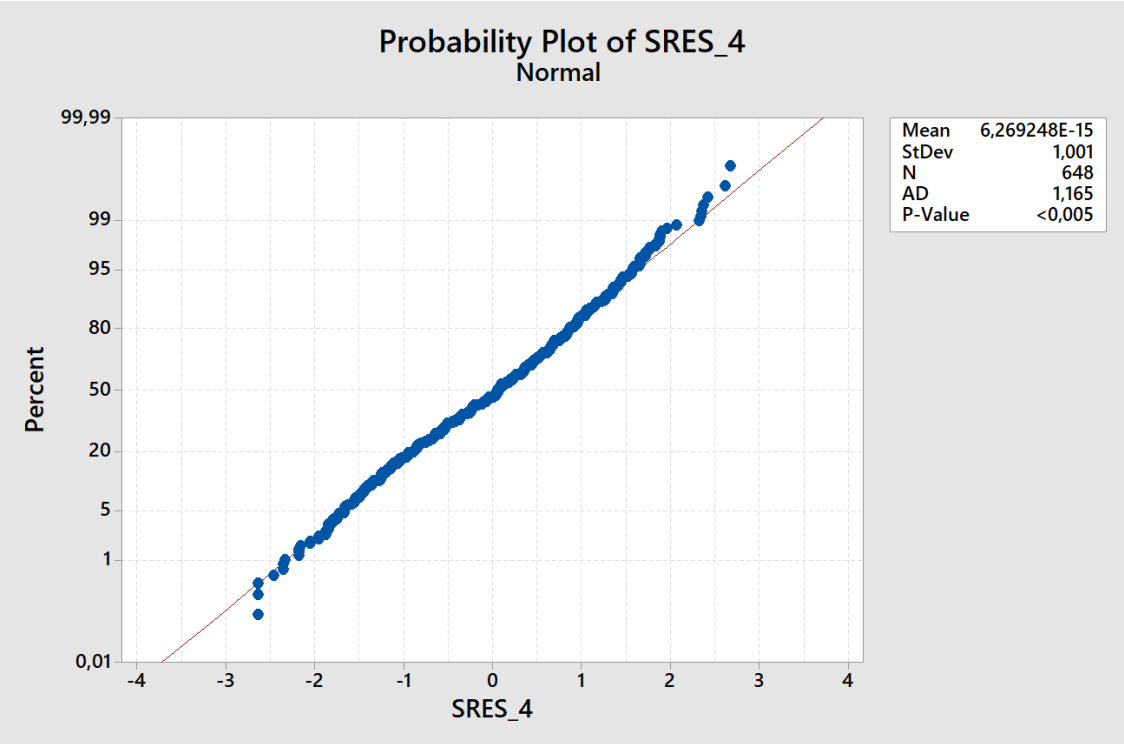

Figure 7.26

No outliers are detected.

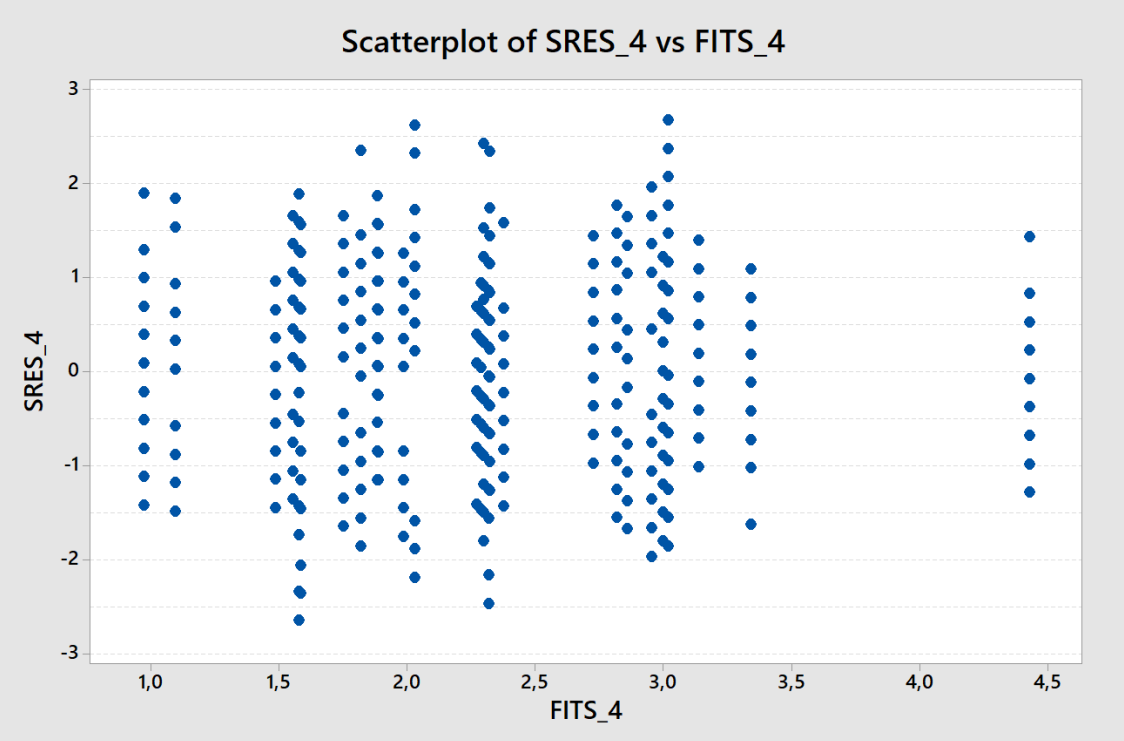

Figure 7.27

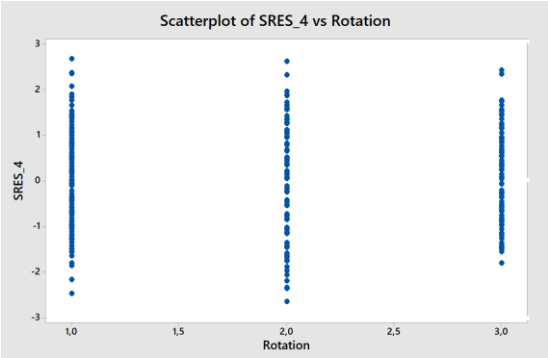

(a)

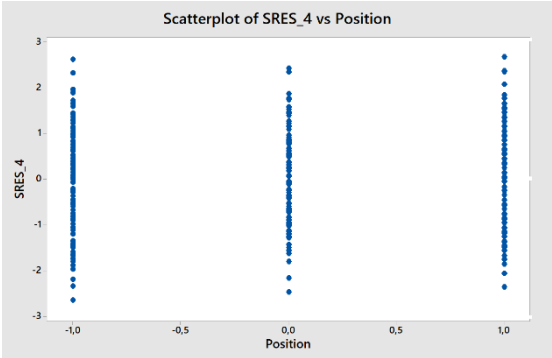

(b)

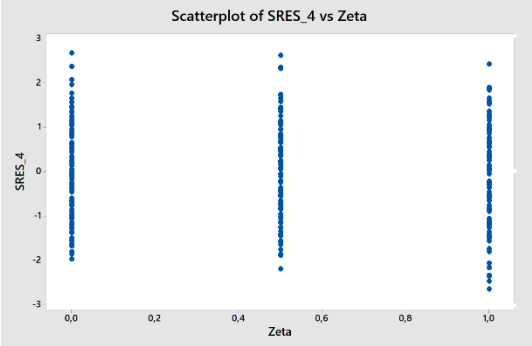

(c)

Figure 28 (a), (b) and (c)

Factors zeta, rotation, zeta^2, position^2, zeta*rotation, zeta*position^2, position^2*rotation seem to have an influence on the response variable.
Zeta (and higher terms) influence can be explained by edge effect of electromagnetic field, like in thickness distribution analysis on the circular face.
Even normality hypothesis is not verified, model accuracy has been tested with some prediction runs.
All measurements obtained are within the prediction intervals, therefore the model can be assumed valid in explaining and predicting the response variable.

Run	**1**	**2**	**3**
Zeta	0	0,25	0
Position	0	0,5	-0,5
Rotation	2	3	1
Thickness	3,1	2,5	3,8

Table 7.2: Prediction runs for lateral surface thickness distribution model

Prediction for Thickness_Lat

Regression Equation

Thickness_Lat = 4,4258 - 3,049 Zeta + 0,0090 Position + 0,000000 Rotation_1
- 1,0861 Rotation_2 - 1,6115 Rotation_3 + 0,940 Zeta*Zeta
- 1,4198 Position*Position + 0,0514 Zeta*Position + 0,000000 Zeta*Rotation_1
+ 0,6500 Zeta*Rotation_2 + 1,5910 Zeta*Rotation_3
+ 0,000000 Position*Rotation_1 - 0,0569 Position*Rotation_2
- 0,4285 Position*Rotation_3 + 0,1340 Zeta*Position*Position
+ 0,000000 Position*Position*Rotation_1 + 0,9833 Position*Position*Rotation_2
+ 0,9083 Position*Position*Rotation_3

Settings

Variable	Setting
Zeta	0
Position	0
Rotation	2

Prediction

Fit	SE Fit	95% CI	95% PI
3,33970	0,0544108	(3,23285; 3,44655)	(2,67143; 4,00797)

Settings

Variable	Setting
Zeta	0,25
Position	0,5
Rotation	3

Prediction

Fit	SE Fit	95% CI	95% PI
2,18581	0,0391664	(2,10890; 2,26272)	(1,52167; 2,84995)

Settings

Variable	Setting
Zeta	0
Position	-0,5
Rotation	1

Prediction

Fit	SE Fit	95% CI	95% PI
4,06635	0,0479511	(3,97219; 4,16051)	(3,39999; 4,73271)

7.3 Analysis of mean and standard deviation of face and lateral surface

In industrial application of PVD, it is important to guarantee to the customer a certain mean on every part type, and a correspondent limited variability.
Therefore, thickness mean and standard deviation, both on circular face and lateral surface, have been analyzed.
It is important to remember that all consideration are valid only for geometries similar to the cylindrical specimens employed, since result could be different in case of different shaped samples, or different orientation when mounted on coating fixtures.
Figure 7.29 shows a plot which relates thickness mean on the face (meanF) vs lateral surface mean (MeanL). Right side cluster belongs to 1-fold rotation, the other to 1 and 2-fold rotation.
The plot shows a moderate linear dependence of the two means, and a higher mean difference between face and lateral surface for 1-fold rotation samples.

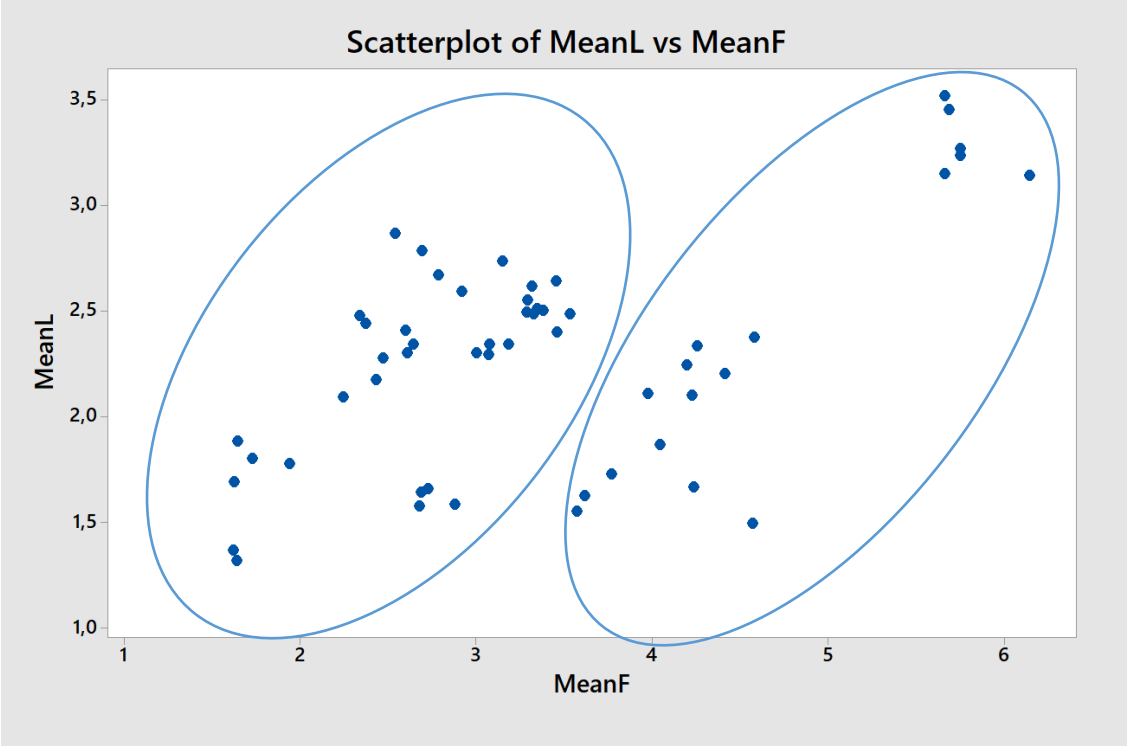

Figure 7.29

Next plot links mean and the natural logarithm of standard deviation on circular face and on the lateral surface. In the graph related to the face, no significant distribution are observed, while on the lateral surface it has been detected a cluster of data (circled).
This cluster refers to 3-fold rotation data. It is clear that, while the mean value of thickness can vary, in 3-fold rotation the lateral thickness distribution is by far more constant with respect the other two rotation modes.
The result can be explained by the fact that the 3-fold rotation modes maximize the uniformity of the time that each part of the specimen is exposed in line of sight with respect to targets of depositing material.

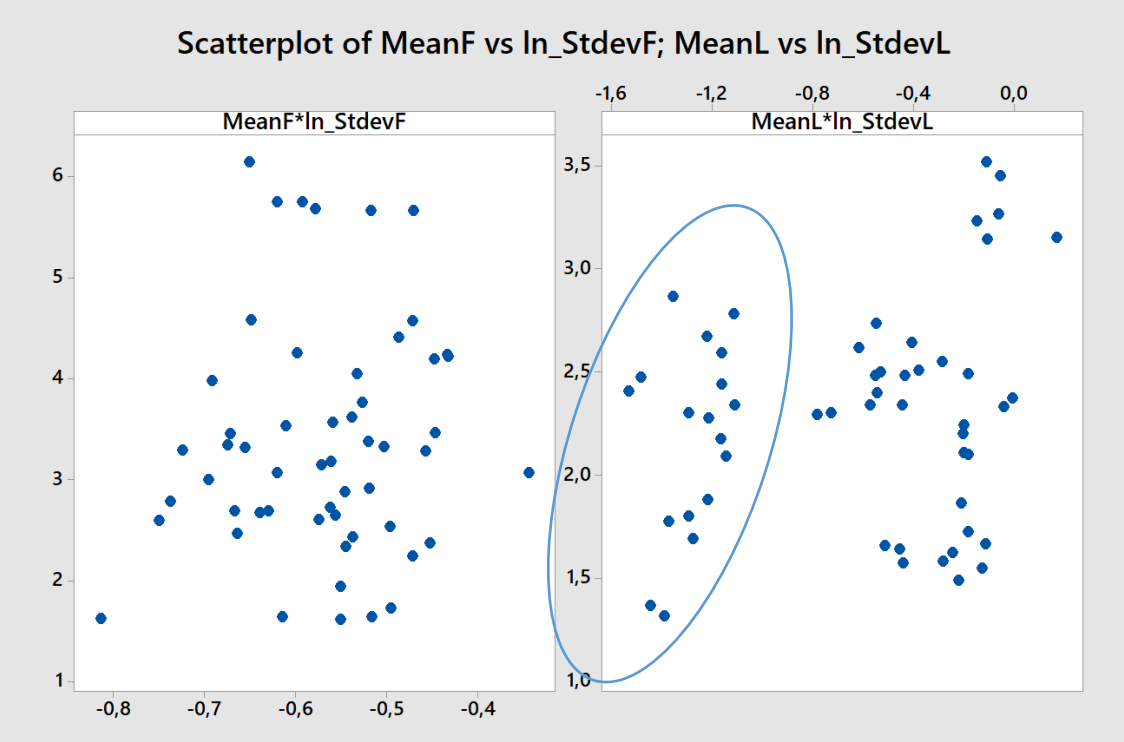

Figure 7.30

Figure 7.31 displays the distribution of thickness means and standard deviations with respect to axial position inside the chamber. Lateral surfaces means in the central position shows slightly greater values, a similar behavior is not observed on the face.

Figure 7.31

More consistent results are shown in the same graph referred to rotation modes.
Mean on face have a decreasing trend, increasing the number of rotation; it is also clear that more rotation modes reduce the standard deviation on the lateral surface.

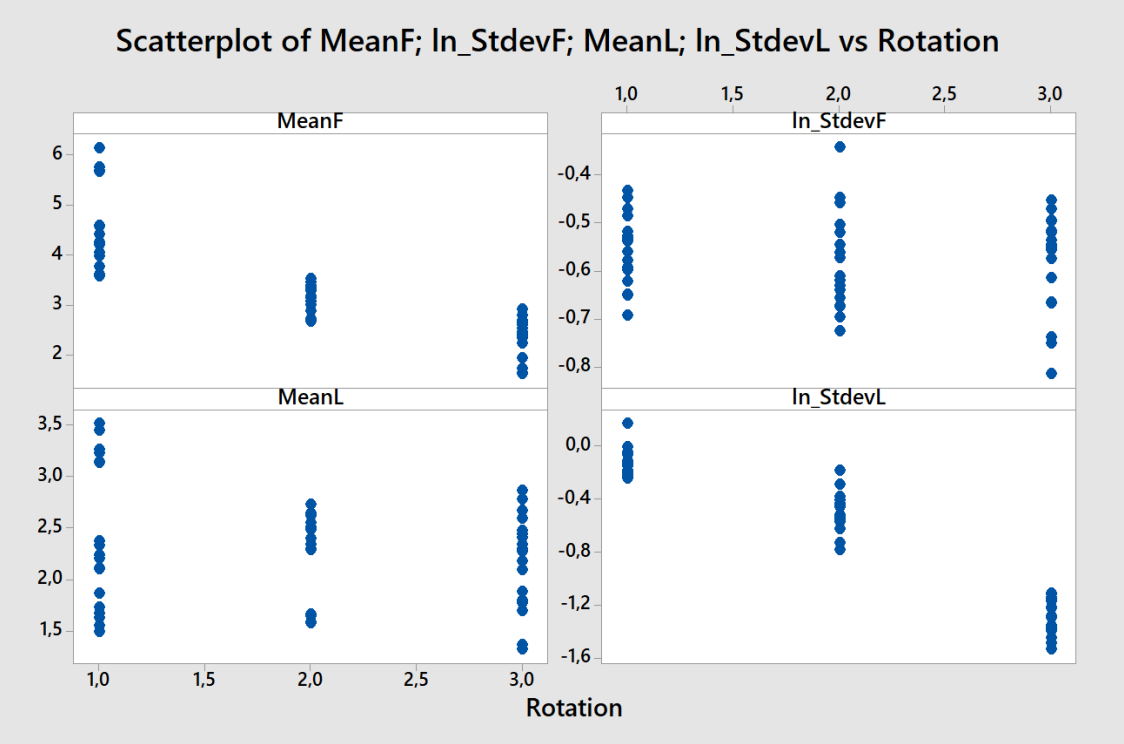

Figure 7.32

Therefore, in designing a coating process for parts with similar geometry and shape of the specimens employed, it must be taken into account that similar mean values on the face and on the lateral surface can be obtained only with the 3-fold rotation.

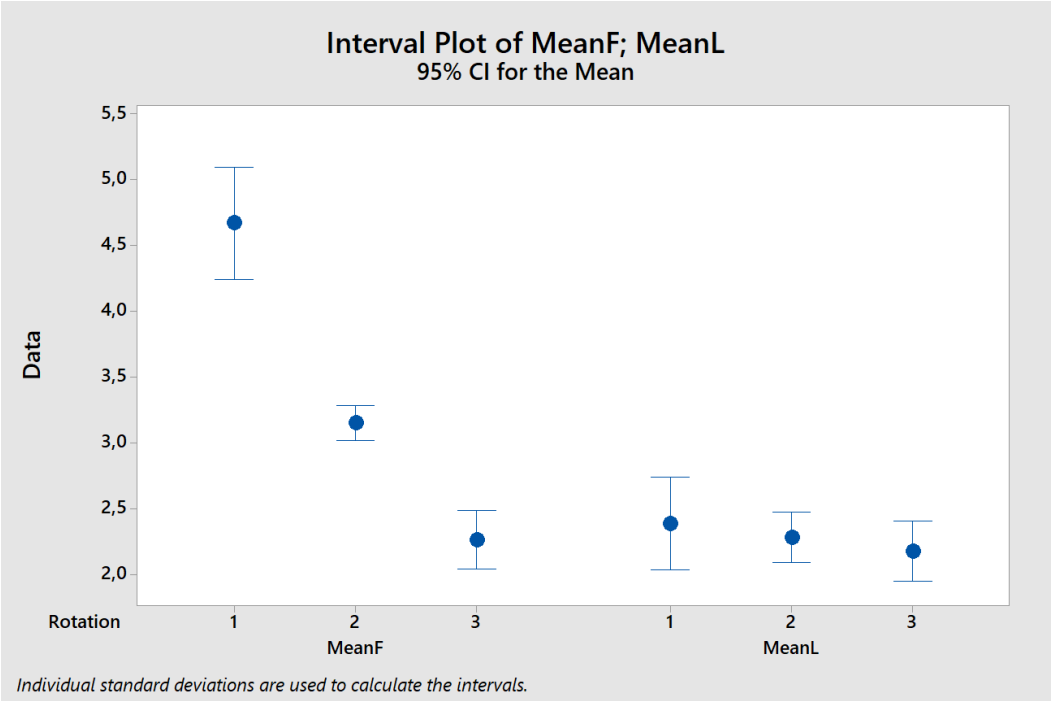

Figure 7.33

Thickness uniformity on the face is not influenced by the rotation modes, while highest constancy in the lateral surface can be reached with the 3-fold rotation.

Figure 7.34

Finally, another interesting results is the proportionality of the mean on the face with respect to the measurement in the central point (ref. paragraph 7.1).
A linear regression model has been set up. The model shows a perfect linear behavior.
This result is aligned with the model of thickness distribution on the circular face. Thickness has a minimum in the surface center, then it increases its value close to the borders.

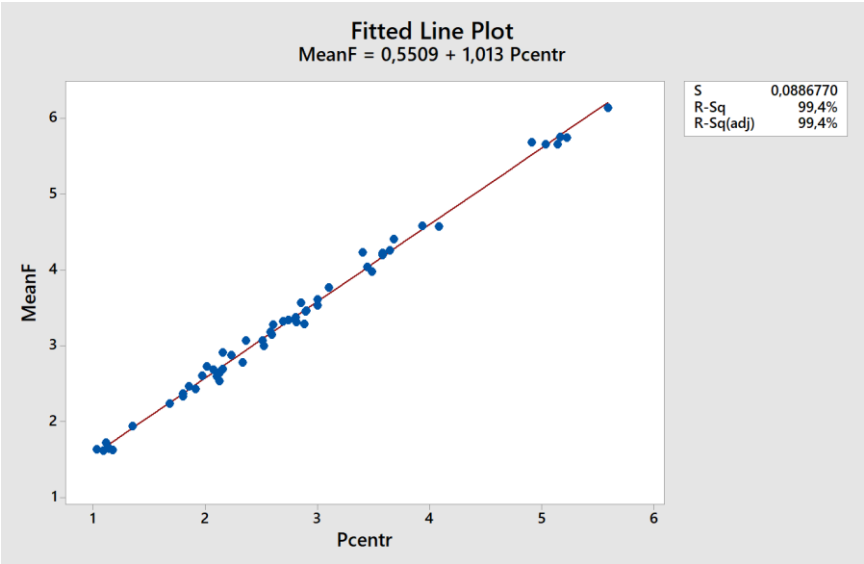

Figure 7.35

Chapter 8

Conclusion and further developments

The study conducted shows a way to regulate coating thickness parameters (mean value and uniformity) on the base of loading parameters, like rotation modes and axial positioning inside the chamber.
Controlling the thickness level and uniformity is one of the biggest issue to ensure a high-quality coating and therefore high performance of coated components and tools.
Particular attention must be paid on the choice of rotation modes: 1-fold rotation maximizes thickness on the area directly exposed to targets, but variability with respect to other zones is higher.
A process with more rotations modes reduces the local deposition rate but enhances a constant thickness level.
Therefore, if high thickness level and uniformity are required, a multiple coating process with several rotation modes can be evaluated.
Process cost will rise, due to the higher consumption of resources (energy, material, manpower etc..), therefore the choice must me evaluated also from the economic point of view. However not all coating types are suitable to adhere on a previously deposited coating layer.
In addition, edge effect must be taken into account. Tools and components with sharp edges are more likely to be influenced by this phenomenon.
In designing the coating process for a specific tool type, test should be made in order to state the thickness level which ensures best performance. Once detected ideal thickness, a distribution model can be made, in a similar way of the regression models developed in chapter 7 of this study.
It is clear that tolerance intervals on coating thickness must be defined on specific zone of the piece. Generally, the wider is the zone to be guaranteed, the wider the tolerance interval should be. Following this rule, satisfying process capability ratios can be reached.

Further developments in this field could interest the distribution of deposition rate, and consequently coating thickness in a definite amount of time, for several definite parts geometries.
A further study could include new source of variation, like the use of different machines of the same model, or even of different models.
Finally, a similar study should be run for different PVD coating technologies, like sputtering processes.

Bibliography

[AIAG10] *Measurement Systems Analysis – MSA Fourth edition*, Automotive Industry Action Group – [Chrysler Group LLC, Ford Motor Company, General Motors Corporation-2010

[Bob16] K. Bobzin, *High-performance coatings for cutting tools,* CIRP Journal of Manufacturing Science and Technology-2016

[Bob17] K. Bobzin, T. Brögelmann, C. Kalscheuer, T. Liang, *High-rate deposition of thick (Cr,Al)ON coatings by high speed physical vapor deposition*, Surface & Coatings Technology-2017

[Bun92] R.F. Bunshah, *PVD and CVD Coatings, Friction, Lubrication, and Wear Technology*, Vol 18, ASM Handbook, ASM International-1992

[Bur05] R. K. Burdick, C. M. Borror, D. C. Montgomery, *Design and Analysis of Gauge R&R Studies – Making Decisions with Confidence Intervals in Random and Mixed ANOVA Models*, ASA-SIAM-2005

[Fri99] C. Friedrich, G. Berg, J. Senf, E. Broszeit, *Reliable PVD coatings on components: aspects of deposition and characterization for quality management*, Surface & Coatings Technology-1999

[Fuc95] F. J. Fuchs, *Ultrasonic cleaning: Fundamental theory and application*, conference paper, NASA Marshall Space Flight Center, Aerospace Environmental Technology Conference; p 369-378-1995

[Mah00] J. E. Mahan, *Physical vapor deposition of thin films*, John Wiley & Sons, Inc.-2000

[Mat96] A. Matthews, A. Leyland and P. Stevenson, *Widening the market for advanced PVD coatings*, Journal of Materials Processing Technology 56 -1996

[Pan07] M. Panjan, M. Cekada, P. Panjan, T. Peterman, *Computer Simulation of Multilayer Structure of TiAlN/CrN Coatings,* Plasma Processes and Polymers-2007

[Pan13] M. Panjan, *Influence of substrate rotation and target arrangement on the periodicity and uniformity of layered coatings*, Surface & Coatings Technology-2013

[Rot96] B. Rother, H.A. Jehn, H.M. Gabriel, *Multilayer hard coatings by coordinated substrate rotation modes in industrial PVD deposition systems,* Surface & Coatings Technology-1996

[Rot99] B. Rother, G. Ebersbach, H.M. Gabriel, *Substrate-rotation systems and productivity of industrial PVD processes*, Surface & Coatings Technology-1999

[Tuc13] R.C. Tucker, Jr., *Surface Engineering, Thermal Spray Technology*. Vol 5A, ASM Handbook, ASM International-2013

[Xu98] H. Xu, S Gong, L. Deng, *Preparation of thermal barrier coatings for gas turbine blades by EB-PVD*, Thin Solid Films-1998

International standards:

EN ISO 3497:2001 *Metallic coatings —Measurement of coating thickness — X-ray spectrometric methods*

EN ISO 26423:2016 *Fine ceramics (advanced ceramics, advanced technical ceramics) — Determination of coating thickness by crater-grinding method*